

## **Master thesis : Design of High Entropy Alloys through Laser Powder Bed Fusion with the help of Differential Thermal Analysis**

**Auteur :** Blondiau, Catherine

**Promoteur(s) :** Mertens, Anne; Tchuindjang, Jérôme Tchoufack

**Faculté :** Faculté des Sciences appliquées

**Diplôme :** Master en ingénieur civil biomédical, à finalité spécialisée

**Année académique :** 2023-2024

**URI/URL :** <http://hdl.handle.net/2268.2/20446>

---

### *Avertissement à l'attention des usagers :*

*Tous les documents placés en accès ouvert sur le site le site MatheO sont protégés par le droit d'auteur. Conformément aux principes énoncés par la "Budapest Open Access Initiative"(BOAI, 2002), l'utilisateur du site peut lire, télécharger, copier, transmettre, imprimer, chercher ou faire un lien vers le texte intégral de ces documents, les disséquer pour les indexer, s'en servir de données pour un logiciel, ou s'en servir à toute autre fin légale (ou prévue par la réglementation relative au droit d'auteur). Toute utilisation du document à des fins commerciales est strictement interdite.*

*Par ailleurs, l'utilisateur s'engage à respecter les droits moraux de l'auteur, principalement le droit à l'intégrité de l'oeuvre et le droit de paternité et ce dans toute utilisation que l'utilisateur entreprend. Ainsi, à titre d'exemple, lorsqu'il reproduira un document par extrait ou dans son intégralité, l'utilisateur citera de manière complète les sources telles que mentionnées ci-dessus. Toute utilisation non explicitement autorisée ci-avant (telle que par exemple, la modification du document ou son résumé) nécessite l'autorisation préalable et expresse des auteurs ou de leurs ayants droit.*

---



UNIVERSITY OF LIEGE  
FACULTY OF APPLIED SCIENCES

---

## Design of High Entropy Alloys through Laser Powder Bed Fusion with the help of Differential Thermal Analysis

---

Master thesis conducted by  
**Catherine BLONDIAU**  
with the aim of obtaining the degree of Master in Biomedical Engineering

Under the supervision of **Anne MERTENS**  
Ph.D. Student supervisor : **Herrim SEIDOU**

*Academic year 2023-2024*





---

## Abstract

The use of metal alloys has been at the heart of many technological advances, from industry to electronics, throughout human history. Among recent advances, High Entropy Alloys (HEAs) stand out as a promising category, characterised by the balanced presence of several elements. These HEAs have attracted growing interest because of their exceptional properties, opening up new prospects for the design of high-performance materials. They offer promising opportunities in a range of applications, from aerospace to biomedical.

The emergence of additive manufacturing (AM) and laser powder bed fusion (LPBF) technology has created new opportunities for the design and production of complex metal components. LPBF's ability to produce parts with complex geometries and high density makes it an attractive technique in the HEA field.

This work focuses on the development of new HEAs by LPBF, with the support of differential thermal analysis (DTA). In a first step, a new HEA was investigated, exploring various combinations of elements to achieve optimal properties. The methodology involved the manufacture of HEA samples by DTA, followed by in-depth analysis of their microstructure, phases and hardness. Different analyses were carried out. Analyses of the DTA cooling curves helped to determine the solidification path. Characterisation was performed using an optical microscope (OM), a scanning electron microscope (SEM) and energy dispersive spectrometry (EDX). This confirmed the presence of specific phases in the microstructures, confirming the predictions made by the VEC theory. Vickers hardness was used for the hardness. In a second step, the LPBF technology was applied to manufacture a new HEA, in order to assess the feasibility and final properties of the parts produced.

In conclusion, this work confirms the help of theories in predicting present phases, as well as the benefits that DTA analysis can bring to the research for a new HEA design.

---

## Acknowledgments

I would like to express my heartfelt gratitude to my supervisor, Anne Martens, for providing me with the opportunity to delve in this captivating research topic, and for her unwavering support and dedicated guidance throughout this journey. I would also like to express my gratitude for your willingness to proofread this manuscript.

Next, I extend my sincere thanks to the entire Metallic Material Science (MMS) team, who warmly welcomed me and offered invaluable assistance on various aspects of my thesis. Special appreciation goes to Sylvie Salieri, Rosine Pirson, Olivier Dedry, Jérôme Tchuindjang, Gauthier Snoeck and Enrico Saggionetto. In particular, I want to acknowledge Herrim Seidou, Ph.D. student, for his supervision. Thank you for dedicating your time to elucidate the intricacies of the subject, assisting me in my work and advised on the writing of this manuscript.

I would also like to convey my appreciation to the members of my thesis committee for their time spent reviewing my work and participating in my oral defense.

A specific thank you goes out to all my friends and family who supported, stood by me or given advice throughout this year. Special gratitude to Lise, Pauline, and Chloé. Thank you for all the good times we've had together, and for the motivation you've given me. Additionally, I want to express my thanks to my everlasting supporter, my girlfriend Louise, who continued to believe in me and supported me until the end.

# Contents

<b>Abstract</b>	<b>2</b>
<b>Acknowledgments</b>	<b>3</b>
<b>1 Introduction</b>	<b>9</b>
<b>2 State of the art</b>	<b>10</b>
2.1 Additive manufacturing . . . . .	10
2.1.1 Laser powder bed fusion (LPBF) . . . . .	13
2.1.1.1 Process mechanism . . . . .	14
2.1.1.2 Rheological properties of powders . . . . .	16
2.1.1.3 Influence of parameters and defects . . . . .	17
2.2 High Entropy Alloys (HEAs) . . . . .	23
2.2.1 Introduction . . . . .	23
2.2.2 Definitions and interpretations . . . . .	25
2.2.3 The four core effects . . . . .	25
2.2.4 Properties of HEAs . . . . .	27
2.2.4.1 Corrosion properties . . . . .	27
2.2.4.2 Hardness properties . . . . .	27
2.2.5 Phases property and influence of the elements . . . . .	27
<b>3 Materials and methods</b>	<b>30</b>
3.1 Original powders . . . . .	30
3.2 Powder preparation . . . . .	31
3.2.1 Powder preparation for Differential Thermal Analysis (DTA) . . . . .	31
3.2.2 Laser Powder Bed Fusion (LPBF) powder preparation . . . . .	32
3.3 Sample production . . . . .	34
3.3.1 Differential thermal analysis . . . . .	34
3.3.2 Laser powder bed fusion . . . . .	35
3.3.2.1 Single track . . . . .	35
3.3.2.2 Cubes . . . . .	36
3.4 Pycnometer analysis . . . . .	37
3.5 Profilometer analysis . . . . .	38
3.6 Microstructural characterisation . . . . .	38
3.6.1 Sample preparation . . . . .	38
3.6.2 Optical microscope (OM) and Stream Analysis software . . . . .	40
3.6.3 Scanning Electron Microscope . . . . .	40
3.7 Hardness . . . . .	41
<b>4 Results</b>	<b>43</b>
4.1 Differential thermal analysis samples . . . . .	43
4.1.1 Single phase microstructure . . . . .	43
4.1.2 Dual phases . . . . .	45
4.1.2.1 CrFeMnNi-based . . . . .	45
4.1.2.2 AlCrFeMnNi-based . . . . .	47
4.1.3 Triple phase . . . . .	51
4.2 Spreadability . . . . .	53

4.2.1	Single Track . . . . .	53
4.2.2	LPBF printed cubes . . . . .	55
4.3	Laser powder bed fusion samples . . . . .	55
4.3.1	Single tracks . . . . .	55
4.3.2	LPBF printed cubes . . . . .	57
4.3.2.1	Density . . . . .	58
4.3.2.2	Surface characterisation . . . . .	59
4.4	Hardness analysis . . . . .	61
<b>5</b>	<b>Discussion</b>	<b>63</b>
5.1	Near equilibrium solidification . . . . .	63
5.1.1	Influence of elements . . . . .	63
5.1.2	Phase prediction theories . . . . .	65
5.1.2.1	FCC and BCC phases . . . . .	65
5.1.2.2	Sigma phases . . . . .	66
5.2	Out of equilibrium solidification . . . . .	68
5.2.1	Rheology of powders . . . . .	68
5.2.2	Solidification . . . . .	68
5.3	Hardness analysis . . . . .	70
5.4	Limitations . . . . .	71
<b>6</b>	<b>Future perspectives</b>	<b>72</b>
<b>7</b>	<b>Conclusion</b>	<b>73</b>
	<b>Annex</b>	<b>84</b>

## List of Tables

1	Metal AM process [16]. . . . .	13
2	Defect and associated causes [21]. . . . .	18
3	VEC of the element [86]. . . . .	29
4	Selected elements used in this work. . . . .	30
5	Chemical composition of the 316L steel powder. . . . .	30
6	Chemical composition of single track: $AlCrFe_2MnNi_2$ . . . . .	32
7	Chemical composition of LPBF printed cubes: $Al_{0.2}Cr_{0.68}Fe_{1.79}MnMo_{0.1}Ni_{1.47}$ . . . . .	32
8	Powder used for single track of $AlCrFe_2MnNi_2$ . . . . .	33
9	Chemical composition of the DTA samples. . . . .	34
10	Specification of Aconity MINI SLM printer. . . . .	36
11	3D printing parameters. . . . .	37
12	Principal cooling peaks for $Al_{0.1}Cr_2Fe_{3.4}MnMo_{0.2}Ni_{3.2}$ , $CrFe_2MnNi_2$ and $CrFe_2MnMo_{0.3}Ni_2$ samples. . . . .	43
13	EDX analysis of chemical composition of $Al_{0.1}Cr_2Fe_{3.4}MnMo_{0.2}Ni_{3.2}$ , $CrFe_2MnNi_2$ and $CrFe_2MnMo_{0.3}Ni_2$ samples. . . . .	45
14	Principal cooling peaks for $CrFeMnNi$ and $Cr_2Fe_2MnNi$ samples. . . . .	45
15	EDX analysis of chemical composition of $CrFeMnNi$ and $Cr_2Fe_2MnNi$ samples. . . . .	47
16	Quantification of the BCC and FCC phases for $CrFeMnNi$ and $Cr_2Fe_2MnNi$ samples. . . . .	47
17	Principal cooling peaks for $AlCrFeMnNi$ , $AlCrFe_2MnNi_2$ , and $AlCrFe_2Ni_2$ samples. . . . .	48
18	EDX analysis of chemical composition of $AlCrFe_2MnNi_2$ , $AlCrFe_2Ni_2$ and $AlCrFeMnNi$ samples. . . . .	50
19	Quantification of the phases for $AlCrFeMnNi$ , $AlCrFe_2MnNi_2$ , and $AlCrFe_2Ni_2$ samples . . . . .	51
20	Principal cooling peaks for $AlCrFe_2Mo_{0.3}Ni_2$ and $AlCrFe_2MnMo_{0.3}Ni_2$ samples. . . . .	52
21	EDX analysis of chemical composition of $AlCrFe_2MnMo_{0.3}Ni_2$ and $AlCrFe_2Mo_{0.3}Ni_2$ samples. . . . .	53
22	Hardness of the DTA sample. . . . .	62
23	VEC and phases observed of DTA samples. . . . .	67

## List of Figures

1	Market share of different industries for AM applications [11]. . . . .	10
2	Metal Additive Manufacturing Market in 2020 [16]. . . . .	12
3	Schematic diagram of LPBF process [26] and [27]. . . . .	15
4	Different processes for powder production [38]. . . . .	17
5	Keyhole formation [43]. . . . .	18
6	Micrograph of fusion pore [46]. . . . .	19
7	Micrograph of gas porosity [49]. . . . .	19
8	Droplet splash in LPBF causing balling [21]. . . . .	20
9	Schematic diagram of the solidification of molten pool [56]. . . . .	20
10	Illustration of all four parameters that contribute to the Ed used in LPBF [59]. .	21
11	Schematic of different types of scanning strategy. (a) uni-directional scan, (b) bi-directional scan, (c) bi-directional, 90° rotation of scan, (d) 90° rotation of uni-directional scan between successive layers, (e) 45° rotation of scan vector [64].	22
12	Evolution of engineering materials [68]. . . . .	23
13	Schematic HEA and conventional alloy. A – E represent different element species in general. (a) Difference based on the atomic structure [4], (b) Difference based lattice distortion in body-centered cubic [67]. . . . .	24
14	The number of times each phase is present in 648 studies on the microstructure of HEAs [71]. . . . .	27
15	(a) Face Centered Cubic Structure, (b) Body-Centered Cubic Structure [80]. . .	28
16	SEM micrographs of powders used. (a) Al powder, (b) Mo powder, (c) Cr powder, (d) Ni powder, (e) Mn powder, (f) 316L steel powder. . . . .	31
17	HAVER EML 200 Premium. . . . .	33
18	$Al_{0.2}Cr_{0.68}Fe_{1.79}MnMo_{0.1}Ni_{1.47}$ after manually mixing. (a) Macroscopic view of $Al_{0.2}Cr_{0.68}Fe_{1.79}MnMo_{0.1}Ni_{1.47}$ , (b) SEM-micrograph of $Al_{0.2}Cr_{0.68}Fe_{1.79}MnMo_{0.1}Ni_{1.47}$ . . . . .	33
19	NETZCH STA 449C Jupiter DTA. . . . .	34
20	Aconity MINI printer. . . . .	35
21	AccuPyc II Series 1345 Pycnometer. . . . .	37
22	Alicona InfiniteFocus G5. . . . .	38
23	STRUERS Tegramin-30. . . . .	39
24	Sample prepared for SEM, in Bakelite and with silver paint. . . . .	39
25	Olympus BX60. . . . .	40
26	Tescan Clara Ultra-High Resolution. . . . .	41
27	(a) EMCO M1C 010, (b) Schematic of Vickers hardness setup [102]. . . . .	41
28	Optical micrograph of hardness Vickers indentation. . . . .	42
29	DTA cooling plot at 20°C /min for $Al_{0.1}Cr_2Fe_{3.4}MnMo_{0.2}Ni_{3.2}$ and at 5 °C /min for $CrFe_2MnNi_2$ and $CrFe_2MnMo_{0.3}Ni_2$ samples. . . . .	44
30	OM and SEM-micrographs of sample. (a) OM-micrograph of $CrFe_2MnNi_2$ sample, (b) SEM-micrograph of $CrFe_2MnMo_{0.3}Ni_2$ sample. . . . .	44
31	DTA cooling plot for $CrFeMnNi$ and $Cr_2Fe_2MnNi$ samples. . . . .	46
32	OM-micrograph of $CrFeMnNi$ sample. . . . .	46
33	Quantification of the phases in the microstructure of CrFeMnNi. . . . .	47
34	DTA cooling plot for $AlCrFeMnNi$ , $AlCrFe_2MnNi_2$ , and $AlCrFe_2Ni_2$ samples. .	48

35	SEM and OM-micrographs of samples. (a) SEM-micrograph of $AlCrFe_2MnNi_2$ sample, (b) OM-micrograph of $AlCrFeMnNi$ sample, (c) SEM-micrograph of dendritic region of $AlCrFeMnNi$ sample, (d) SEM-micrograph of inter-dendritic region of $AlCrFeMnNi$ sample. . . . .	49
36	EBSD on $AlCrFe_2MnNi_2$ sample (a) pattern quality, (b) phase map. . . . .	50
37	Quantification of the phases in the microstructure of AlCrFeMnNi-based samples. (a) $AlCrFeMnNi$ sample, (b) $AlCrFe_2MnNi_2$ sample. . . . .	51
38	DTA cooling plot for $AlCrFe_2Mo_{0.3}Ni_2$ and $AlCrFe_2MnMo_{0.3}Ni_2$ samples. . .	52
39	SEM-micrograph of $AlCrFe_2Mo_{0.3}MnNi_2$ . . . . .	53
40	Test for spreadability. (a) $CrFe_2MnNi_2$ with 10 $\mu m$ Cr powders, (b) $CrFe_2MnNi_2$ with 149 $\mu m$ Cr powders, (c) $AlCrFe_2MnNi_2$ with cuboid Ni powder, (d) $AlCrFe_2MnNi_2$ with spherical Ni powder. . . . .	54
41	Effect of morphology of powder in spreadability. (a) Initial mix: $Al_{0.4}Cr_{0.7}Fe_{2.3}MnMo_{0.1}Ni_{2.3}$ , (b) Mix after addition of 316L steel powder: $Al_{0.2}Cr_{0.68}Fe_{1.79}MnMo_{0.1}Ni_{1.47}$ and pre-heating at 200 °C. . . . .	55
42	OM-micrographs of defects in single track $AlCrFe_2MnNi_2$ . (a) Unmelting defect at 50W and 1200mm/s, (b) Irregular track defect at 150W and 1800mm/s, (c) Spatter defect at 175W and 1400mm/s. . . . .	56
43	Width by applied parameters of $AlCrFe_2MnNi_2$ . . . . .	56
44	Quality of track based on laser power and scanning speed of $AlCrFe_2MnNi_2$ . .	57
45	Cubes of $Al_{0.2}Cr_{0.68}Fe_{1.79}MnMo_{0.1}Ni_{1.47}$ printed. . . . .	58
46	Defect during printing of $Al_{0.2}Cr_{0.68}Fe_{1.79}MnMo_{0.1}Ni_{1.47}$ . . . . .	58
47	Graphical correlation between Ed values and percentages of density. . . . .	59
48	Surface roughness of the samples $Al_{0.2}Cr_{0.68}Fe_{1.79}MnMo_{0.1}Ni_{1.47}$ for difference Ed. (a) Low Ed: 57 $J/mm^3$ , (b) Medium Ed: 86 $J/mm^3$ , (c) Medium Ed: 114 $J/mm^3$ , (d) High Ed: 162 $J/mm^3$ . . . . .	60
49	Correlation between quality surface and energy density (Ed). (a) Average roughness of profile plotted in relation to Ed, (b) Mean spacing of profile irregularities of roughness profile plotted in relation to Ed. . . . .	61
50	Surface roughness of the samples $Al_{0.2}Cr_{0.68}Fe_{1.79}MnMo_{0.1}Ni_{1.47}$ for different laser passes (a) One laser pass, (b) Two laser passes. . . . .	61
51	DTA cooling combined plots of temperature of eutectoid transformation with effect of Mo. . . . .	64
52	DTA cooling combined plots of temperature of eutectoid transformation with effect of Mn. . . . .	65
53	Process map with regards to the single track $AlCrFe_2MnNi_2$ . . . . .	69
54	Process map with regards to the printing of $Al_{0.2}Cr_{0.68}Fe_{1.79}MnMo_{0.1}Ni_{1.47}$ alloy. . . . .	70



# 1 Introduction

Additive manufacturing (AM) is a recent technology that has attracted a great deal of interest because of its ability to easily manufacture parts with complex geometries [1]. Among additive manufacturing methods to produce metal parts, laser powder bed fusion (LPBF) stands out for its exceptional qualities about superior surface quality and great-dimensional accuracy [2].

High entropy alloys (HEA) represent another recent discovery, involving alloys with multiple principal elements [3]. HEAs are known to have very good properties, such as high corrosion resistance, high fatigue strength, high hardness, good biocompatibility... [4]. Their common production method is arc melting under vacuum or induction melting followed by casting and mechanical alloying followed by spark plasma sintering [5]. However, more and more research are focusing on HEAs with LPBF because of their high cooling rates [6]. Each element can contribute to the material's performance, making preliminary alloy selection a crucial step in HEA development.

This thesis is part of a Ph.D. thesis aiming to manufacture a new HEA with high corrosion resistance properties using LPBF technology. The initial stages of the Ph.D. involve the selection of elements for inclusion in the alloy, followed by the first analyses of the printed samples.

Differential Thermal Analysis (DTA) was utilised in this study to choose and proportion the elements present in the new HEA. Ten samples with different compositions were prepared using DTA. To investigate these samples, DTA, optical microscopy (OM), scanning electron microscopy (SEM), and Vickers hardness testing were employed to analyse the effects of the elements.

Additionally, 20 printed cubes of the same alloy were produced using different parameters, with variations in energy density and the number of laser passes. The analysis of these samples included the examination of surface characteristics and density.

## 2 State of the art

The aim of this chapter is to establish the context and background necessary for the subsequent discussion of the results. Firstly, Additive Manufacturing (AM) technology will be discussed, with a focus on the Laser Powder Bed Fusion (LPBF) process, used for this study. Subsequently, the second part will describe High Entropy Alloys (HEAs), the type of alloy investigated for this study.

### 2.1 Additive manufacturing

AM, commonly known as 3D printing, is a technological revolution that has reshaped the way objects are designed and manufactured. It was developed in the 1980s, challenging traditional methods such as machining or injection molding [7]. The machining process begins with a block of material in which the desired shape of the part is carved. Injection molding, on the other hand, involves injecting molten material in a mould that has the desired shape for the part [1].

The term "additive manufacturing" refers to a category of techniques that enable objects to be manufactured directly from computer-aided design (CAD) drawings without the need of specially designed tools, moulds or fixtures. This is one of the reasons why they differ from traditional methods [8]. AM enables objects to be created layer by layer, offering a flexibility and versatility never seen before in the traditional manufacturing process [9]. This is achieved by creating a CAD and storing information about each layer in stereolithography files, also known as STL files. This method uses a computer to oversee the entire process, robotic arms, a computer numerical control, a controlled environment and scanning and recording systems [8].

Advances in 3D printing were driven by the growing demand for rapid prototyping and custom component manufacturing [7]. Over the years, AM has surpassed its original purpose of rapid prototyping and has become a widely applied manufacturing method [10]. Indeed, it has a wide range of applications and is already being used in almost every area of life [8]. FIGURE 1 shows the market share of various industries for AM applications, from business machines, aerospace and automotive to medical.

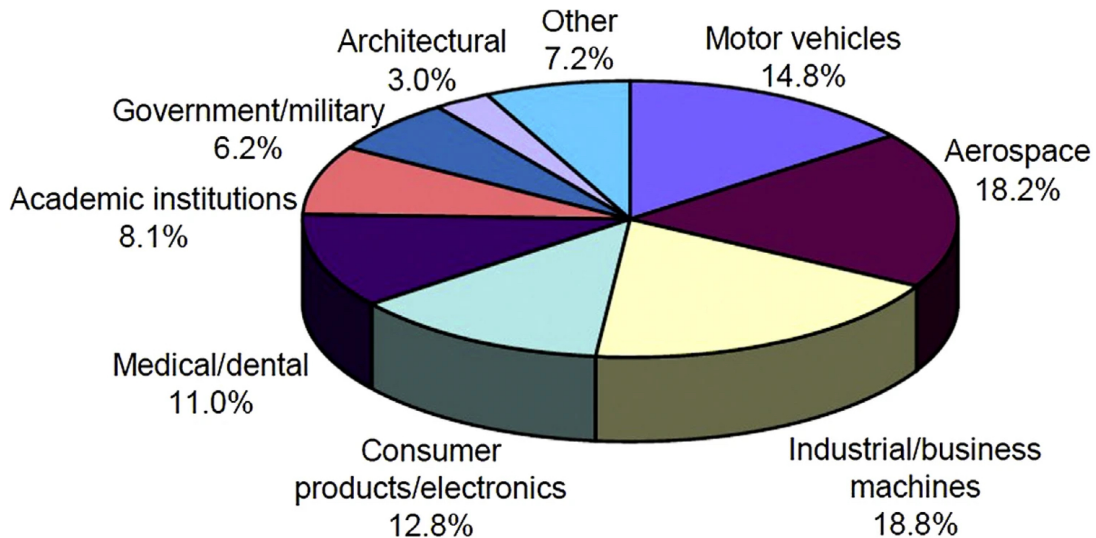


Figure 1: Market share of different industries for AM applications [11].

The growth in the use of AM is due to its many advantages. Following are the most important [1].

- **Freedom of Geometry**

The layer-by-layer printing process offers greater freedom for much more complex geometries that would be impossible to achieve by machining or moulding alone. For example, complex patterns such as angled perforated tubing would be difficult to produce using traditional methods.

- **Customisation and Prototyping Easy to Implement**

Customisation and prototyping are easily achieved, as the CAD file simply needs to be modified to quickly adapt the shape of the part for printing. This capability can be highly beneficial, particularly in the medical sector, where surgeons may need implants tailored precisely to the size and characteristics of the patient. But it is also useful for prototyping because different models can be created quickly and easily, allowing for iterative testing and improvement.

- **Reduced Waste**

As the part is built layer by layer, most materials used during production become part of the final object. As a result, this production method generates minimal waste compared to machining, where raw material is subtracted to create the part.

- **Cost is Independent of the Complexity of the Part**

However, this method still presents several drawbacks and challenges.

- **Microstural Heterogeneity and Anisotropy**

The parts produced exhibit microstructural heterogeneity and anisotropy, which can have a significant impact on their mechanical properties [1]. Anisotropy is a phenomenon in which the characteristics of the part depend on the orientation of the material. This phenomenon is mainly attributed to the thermal stresses experienced by parts during production, including repeated melting and rapid solidification [12]. Additionally, anisotropy can result from defects in the AM such as pores, rough surfaces, lack of fusion between layers, etc [13].

- **Lack of Precision**

Another important drawback is the lack of precision of the method. However, these limitations can be reduced by post-processing techniques [1]. Post-processing methods are explained in more detail in SECTION 2.1.1.1.

- **Restriction on the Size of the Object Produced**

The size of the build platform or the maximum height that the printer can reach is limited, often around 150 dm<sup>3</sup> [1].

- **Not Economical if Many Parts or Non-complex Parts are Produced**

The cost-effectiveness of the method compared with traditional methods often depends on the number of parts produced and the complexity of the part. If the part has to be produced in small quantities, or the complexity is high, AM will be more cost-effective [1].

These defects are one of the reasons why, although AM production is increasing, it remains an alternative production method to traditional methods and is not destined to replace them [1].

These advantages aside, the development of AM is also due to the ability to adapt to different types of material. There are three main types of material used in 3D printing: polymers and composites, metals and alloys and ceramics [14]. The production method depends, among other factors, on the type of material used [15]. This study is related to metals, so the focus is on AM techniques involving metals. Moreover, metallic materials are of growing interest to researchers and industry. Indeed, in addition to the advantages mentioned above, the AM of metals can offer environmental benefits such as the reduction of pollutant emissions [16].

In addition to the type of material used, the classification of AM processes can be based on other parameters such as the solidification process of the material and the deposition method. There are seven major process families for additive manufacturing: Vat Photopolymerization, Material Jetting, Binder Jetting, Material Extrusion, Sheet Lamination, Powder Bed Fusion and Direct Energy Deposition. As shown in FIGURE 2, only five processes are commonly used for metals. However, a focus on only four of the methods will be made, given that even if MJ is in the metal AM techniques, it is not pure metal but polymer with some metal powder added in. TABLE 1 shows the different types of AM used in metal production [16].

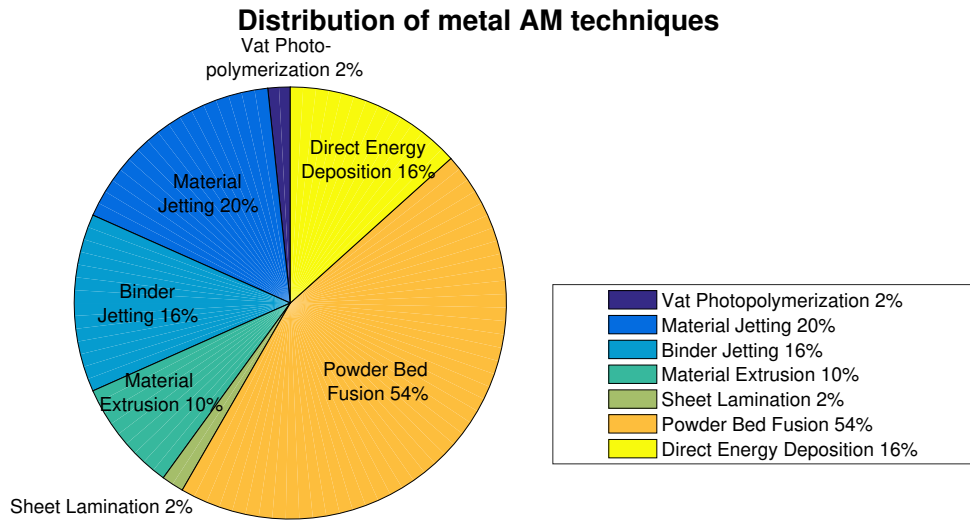


Figure 2: Metal Additive Manufacturing Market in 2020 [16].

Table 1: Metal AM process [16].

AM Category	Metal AM Process	Process Description
<b>Material Extrusion</b>	Fused Deposition Modelling	Melted material is selectively dispensed through a heated extrusion nozzle in a pre-determined path to construct 3D parts
	Bound Powder Extrusion	
<b>Powder Bed Fusion</b>	Direct Metal Laser Sintering	Thermal energy such as electron and laser beams selectively melts and fuses areas of a powder bed. After each print, the build plate is lowered, and a roller adds a new layer of powdered materials and sinters it to the previous layer.
	Selective Laser Melting	
	Electron Beam Melting	
	Direct Metal Laser Melting	
<b>Directed Energy Deposition</b>	Cold spray	A nozzle combined with a multi-axis robot that selectively adds material to a substrate with sufficient energy to create a layer. The material takes the form of a metal wire or powder.
	Thermal energy	
<b>Binder Jetting</b>	Binder Jetting	A liquid-state binder agent is selectively deposited through a print head onto the powder bed, to bind the powder and form a layer of a part. The binder consolidates the powdered materials within and between sliced layers at room temperature.

### 2.1.1 Laser powder bed fusion (LPBF)

As shown in FIGURE 2, LPBF is the most used method for metal printing. Consequently, this is the only method that will be present. The LPBF is one of the powder bed fusion methods where a layer of powder is spread and predetermined regions are then exposed to high-intensity laser energy. In this way, powders can be melted and fused layer by layer according to the design prepared in the CAD software [17]. The LPBF system configuration typically includes a laser source, a build platform, an automated powder delivery system, a

control system and additional components (such as rollers, scrapers, etc). During processing, the powder bed is pulled down and covered with a layer of powder at the same time [18]. One of the characteristics of LPBF compared with other metal AMs is the powders it uses. LPBF generally uses very fine powders, in the 30-45  $\mu\text{m}$  range [19].

Compared to conventional manufacturing methods, LPBF allows for the production of complex-shaped parts without requiring additional post-processing, with virtually no geometric limitations. It offers efficient material usage, high flexibility, and reduced production times [20]. Compared with the metal-working AM method, it has a superior surface quality and greater dimensional accuracy [2]. At the microstructural scale, finer grains are also present in the materials made with LPBF [21].

Despite the advantages of the LPBF process, there are still some challenges to overcome. Firstly, the LPBF process is characterised by rapid solidification and high temperature gradients within the melt pools. Temperature gradients range from  $10^5$  to  $10^8$  K/s. This very high rate results in thermal stresses which lead to segregation and formation of non-equilibrium phases, making it difficult to predict the structure [22]. Furthermore, these repeated cyclic stresses cause fatigue in the pieces produced by LPBF [21]. Also, areas containing pores, whether between layers or on surfaces, are the initiation zones for cracks [23]. Another defect is due to the initial contamination of the powder, local voids or evaporation after deposition of the powder layer. They can lead to microstructural defects, such as warpage or porosity [22]. In addition, the stability, configuration and behaviour of the melt have a significant impact on the roughness, porosity and quality of the surface formed by the accumulation of layers (stair-step effect) [24]. These limitations cannot be completely avoided. However, significant work has been carried out to control the physical phenomena associated with these defects to produce fully dense samples with as few defects as possible [7]. An understanding of the mechanism is essential to avoid further defects.

#### 2.1.1.1 Process mechanism

As explained above, the first step is to create a model of the desired part using CAD software. In the process, data are extracted from a CAD model, which is then cut in thin layers. Each cut layer is developed with the appropriate scan paths [25]. Through the scanner mirrors, a laser beam selectively scans and melts the powders, which have been previously spread on the substrate along the developed scan paths. Once the layer is complete, the build platform is lowered by an amount equal to the layer thickness, and a new layer of powders is spread. The process is repeated until all layers have been printed [25]. The stages of the process are illustrated in FIGURE 3.

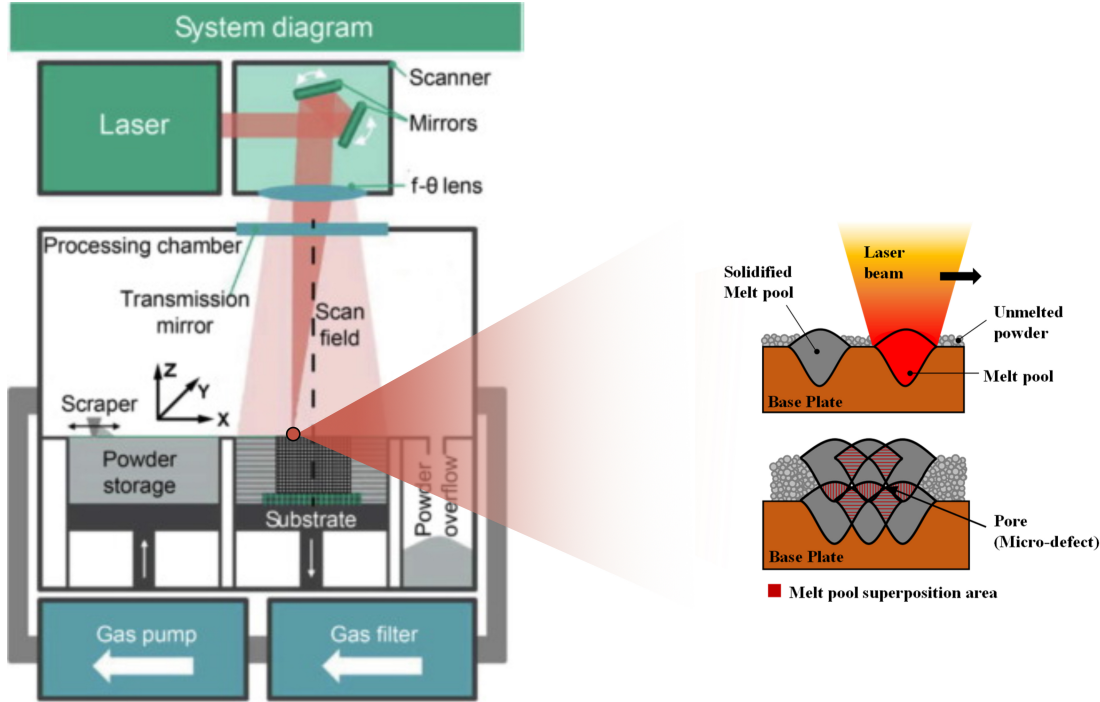


Figure 3: Schematic diagram of LPBF process [26] and [27].

Once printing is complete, the part can be stripped of the remaining unmelted powders. The part can then undergo post-treatment if necessary, to improve the mechanical characteristics and surface quality. Various post-treatment techniques are available. The most common is thermal treatment, but there are also laser polishing and conventional machining processes [28]. Their details are explained below.

### Thermal Treatment

Thermal treatment typically refers to a controlled heating and cooling process used to alter the microstructure of a metallic material, aiming to enhance its physical and/or mechanical properties [29]. More specifically, heat treatment can reduce crack formation, homogenise the microstructure and reduce residual stresses [28]. Because thermal cycling induces residual stresses in the printed parts, post-processing by heat treatment can attenuate the remaining residual stresses. After this heating, the cooling stage needs to be controlled to avoid the development of damaging thermal gradients [30].

### Laser Polishing

Laser polishing is a technique used to improve the surface roughness of parts manufactured by AM. When laser energy is applied to the surface of the material, the peak of the surface rapidly reaches melting temperature. Under the effect of gravity and surface tension, the liquefied material is being reorganised uniformly after the formation of the melting pool. The temperature of the melt pool drops rapidly as soon as the laser beam stops scanning the surface, leading to solidification of the melt pool and reduction in the surface roughness [31].

### Conventional Machining Processes

Conventional machining processes refer to processes such as milling, rolling, chemical machining and abrasive machining. These are conventional manufacturing techniques used to improve the form accuracy and surface finishing of functional parts in industry. They are commonly used as post-processing methods for AM parts due to their maturity and wide

accessibility [32].

The key challenge for LPBF is therefore to establish the appropriate process window for manufacturing the part, so that its microstructural and mechanical properties are optimised. Most defects can in fact be limited or even avoided by selecting the right printing parameters such as laser power, scanning speed or other slicing parameters [21].

#### 2.1.1.2 Rheological properties of powders

Some printed part properties are related to the powder. The morphology and spreadability of the powders are crucial characteristics for the printed part [33]. The term "spreadability" refers to the ability of metal powders layer to evenly and consistently cover the build platform during the powder deposition stage of the additive manufacturing process. The term morphology refers to the size and shape of powder particles, it can be described as irregular, blocky or spherical [34].

The powder morphology plays a role in the deposition level of the powder particles when depositing a new layer during printing. The more spherical the powders, the more uniform their distribution on the manufacturing platform. So, spherical particles enhance spreadability. If the spreadability of powders is optimal, this produces high-quality components with low surface roughness and porosity [35]. In the other hand, poor quality powders will produce a non-uniform powder bed, increasing the risk of spattering. Indeed, uniform dispersion of the powders is necessary to ensure an even heat distribution during laser melting [34]. In addition, the quality of the powder can influence physical properties such as hardness and ductility, and chemical properties including reactivity and impurities [36].

Morphology powder characteristics are significantly influenced by production methods [37]. The various methods used to produce powders are listed in FIGURE 4, and the most common process is explained. There are three types of production: physical, including atomisation processes, melt spinning, and rotating electrode processes; mechanical and chemical. Each of these methods has its own advantages and disadvantages, and the chosen method should be selected based on the desired application, price and chosen elements [38].

##### Atomisation Process

The atomisation process enables the production of spherical powders with controlled diameters, although these powders typically exhibit satellite [38]. Atomisation is a two-stage process involving initial shearing of the liquid metal followed by rapid freezing of the resulting liquid droplets. During the second stage, the molten droplets, created during shearing, seek to minimise their surface energy by adopting spherical shapes before solidification. The efficiency and speed of this process depend on the surface tension of the molten metal and the temperature of the superheated liquid droplets [36].

##### Rotating Electrode Process

The Rotating Electrode Process produces high purity powders with excellent properties for 3D printing [39]. In this method, the rotating electrode undergoes melting through either electric arc application or high-temperature plasma utilisation. This melting action generates molten droplets that are propelled away from the electrode's surface due to centrifugal forces, subsequently encountering a surrounding gas jet. Upon collision and interaction with the gas



jet, the droplets undergo secondary fragmentation induced by aerodynamic drag [36].

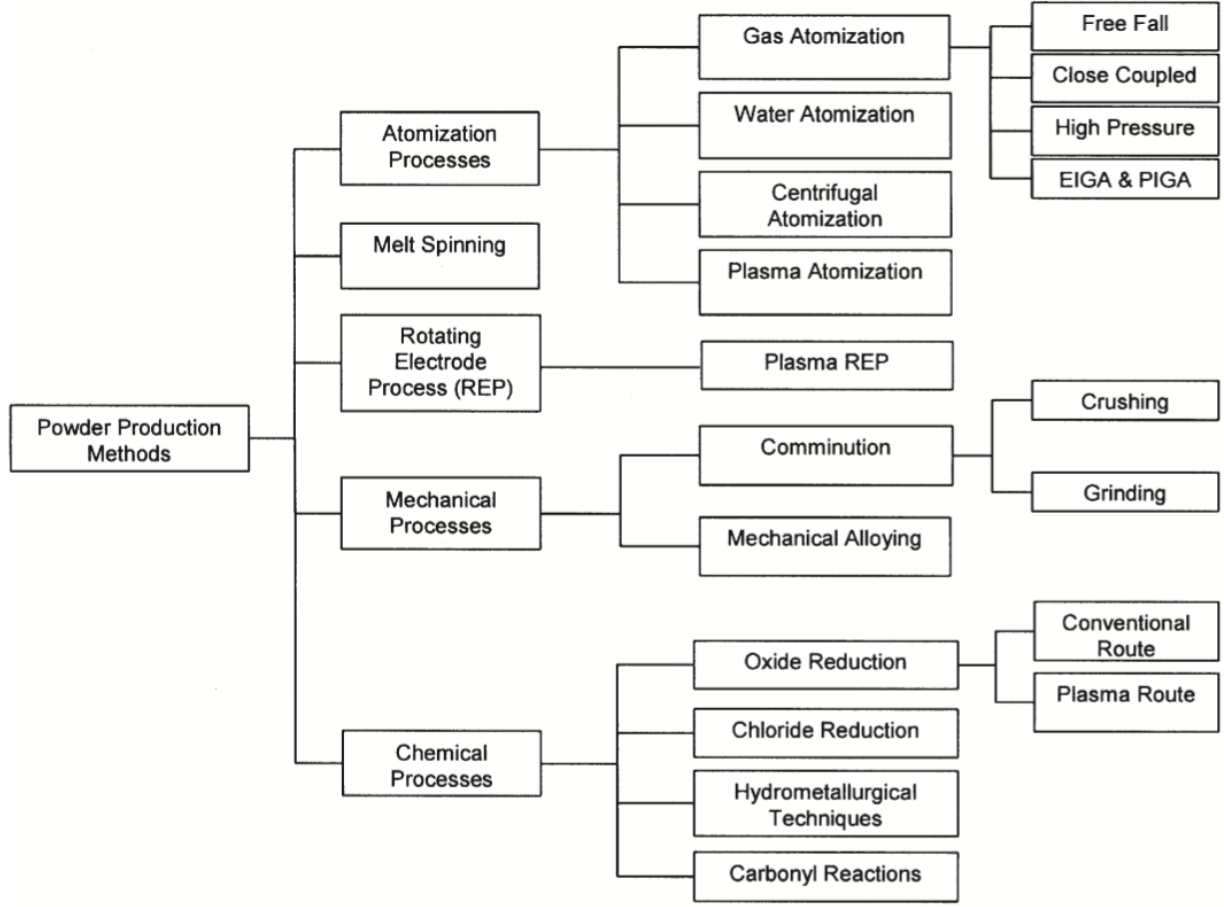


Figure 4: Different processes for powder production [38].

### Mechanical Process

In mechanical process, small particles are produced from larger ones, using crushing or milling method, for example [38].

### Chemical Process

Concerning chemical process, reduction reactions are often used to obtain powders [39].

#### 2.1.1.3 Influence of parameters and defects

The quality of the part can be influenced by parameters other than the quality of the powder. As explained above, some of the defects that can be found in parts printed by LPBF (TABLE 2) can be minimised by choosing the right printing parameters [25]. Typical LPBF parameters include powder layer thickness, beam focus, scanning speed, laser power intensity, hatch spacing and scanning strategy [40].

Table 2: Defect and associated causes [21].

Defects	Causes
Porosity	Insufficient laser energy for sufficient penetration
Balling	Powders in suspension in the powder bed
High Surface Roughness	Presence of gas causing oxidation and adhesion of partially molten powders to the surface of the part
Residual stress, Distortion, and Cracking	Unequal heating of different areas Heating and cooling quickly
Composition change / Loss of alloying element	Vaporisation caused by overheating
Oxide Inclusion	High affinity with oxygen, causing oxide inclusion

Some of these defects are explained in detail below, as well as the process parameters.

### Porosity

Among the defects mentioned, pores are the most common and the most problematic. They have a major impact on the mechanical properties of the parts produced, such as fatigue strength and tensile strength, for example [41].

Porosity can be classified in three categories depending on the formation mechanism: keyholes, lack of fusion and trapped gases [42].

#### • Keyholes

As shown in FIGURE 5, keyhole formation occurs when excessive power density is applied during the melting process of the material, causing the power beam to penetrate deep in the underlying layers [9].

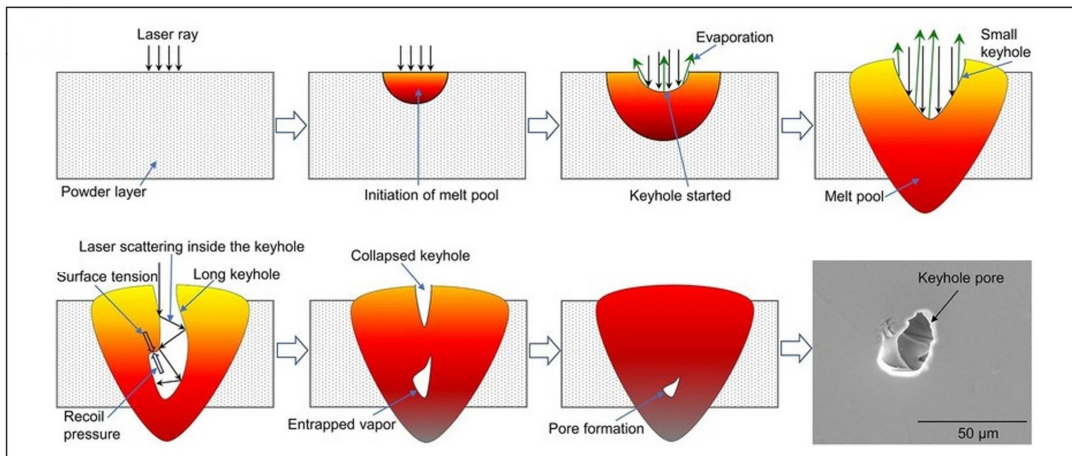


Figure 5: Keyhole formation [43].

#### • Lack of Fusion

Lack of fusion pores form where the laser's energy density is insufficient. This leads to poor heat penetration, preventing the powders from melting completely, or to a poor penetration of the liquid metal in the layer that has previously solidified [44]. These pores are then mainly dominated by the process parameters [45]. As shown in FIGURE 6, these pores often have an irregular shape.

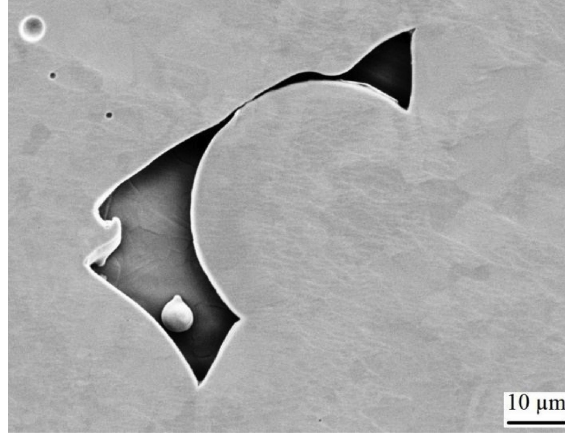


Figure 6: Micrograph of fusion pore [46].

- **Trapped Gases**

The presence of trapped gases in the powders during the powder atomisation process or trapped gases in the melting pool during LPBF processes can lead to the formation of these pores [47]. As shown in FIGURE 7, the observed spherical shape of these pores is due to surface tension [48].

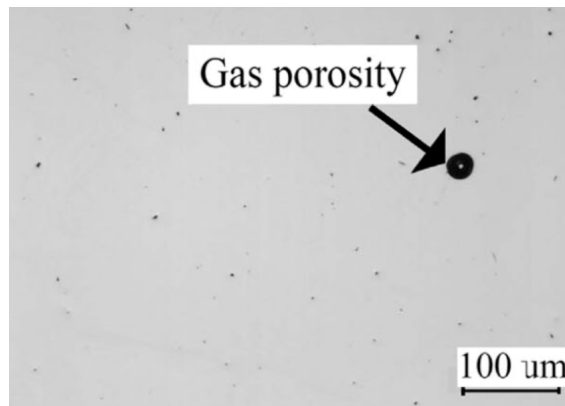


Figure 7: Micrograph of gas porosity [49].

### **Balling**

As shown in FIGURE 8, balling refers to a phenomenon where molten material forms balls or droplets instead of solidifying uniformly on the substrate or base metal [50]. This phenomenon is generally the result of poor wetting between the pools of molten metal and the solid surface, leading to unstable and discontinuous melt tracks. Balling can manifest itself in different ways, notably in the form of spherical balls resulting from splashes of molten metal [51]. Indeed, when the molten metal does not have good contact with the substrate or base metal, in accordance with the principle of minimum surface energy, it tends to separate in small spheres due to surface tension [52]. These spheres can form defects in the manufactured parts, leading to problems such as discontinuous scan tracks, and when the part is manufactured layer by layer, this can lead to unwanted roughness or porosity in the printed part [52].

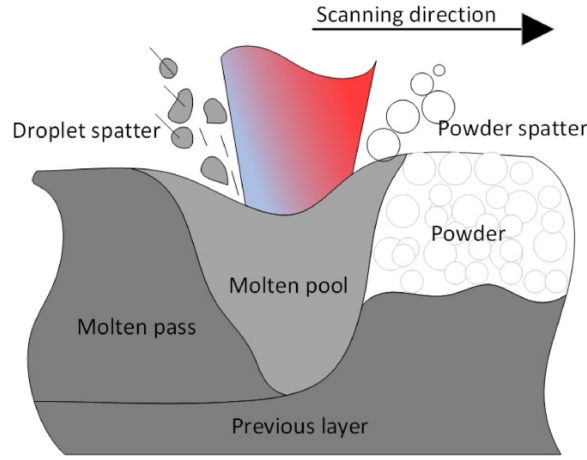


Figure 8: Droplet splash in LPBF causing balling [21].

### Cracks

Cracks are often caused by severe thermal stresses. Cracking in the LPBF process can be divided in solidification cracking and liquefaction cracking [47]. During the solidification of alloys, liquefaction and solidification cracking occur in the presence of a liquid phase, either during the initial solidification process or when the terminal liquid in the heat-affected zone remelts [53].

The main cause of hot cracking in these alloys is the existence of a large mushy zone, the size of which is related to the wide solidification range between liquidus and solidus [54]. Solidification cracking occurs within the molten pool or fusion zone when liquid flow is constrained by increased viscosity at lower temperature, and interdendritic liquid flow is obstructed by solidified dendrite arms [55]. FIGURE 9 illustrates this phenomenon.

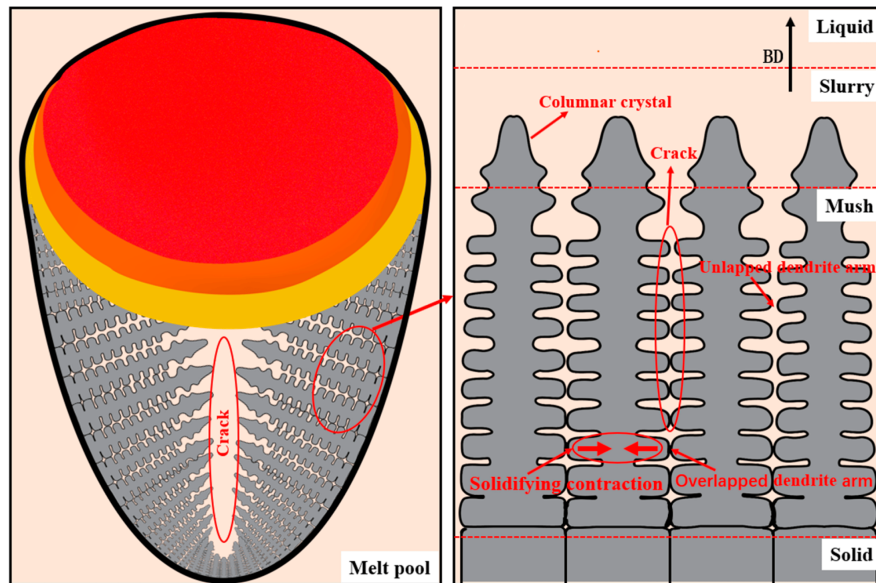


Figure 9: Schematic diagram of the solidification of molten pool [56].

Cold cracks are caused by residual stresses. As the LPBF part is subjected to continuous thermal cycling, the solidified structures undergo rapid contraction and expansion, which can lead to cracks, known as cold cracks [21].

### Printing Parameters

One of the most important printing parameters influencing the quality of the piece is the energy density [25]. In this study, two of these are used: linear energy density (El) and volumetric energy density (Ed). The energy densities group together several of the printing parameters. More specifically, El is the basic density consider the single melt track [57], while Ed reflects the laser beam energy transmitted to a volumetric unit of powder material and is correlated with several relevant parameters of the laser and scanning. The energy density is a crucial parameter in 3D printing, allowing, among other things, the maximisation of material density [58].

The El [J/mm] and Ed [J/mm<sup>3</sup>] can be calculated using the following formulae:

$$El = \frac{P}{v_s} \quad (1)$$

$$Ed = \frac{P}{D_h \cdot D_s \cdot v_s} \quad (2)$$

With  $P$  as the power of the laser [W],  $D_h$  as the hatch spacing [mm];  $D_s$  as the layer thickness [mm], and  $v_s$  as the scanning speed [mm/s]. FIGURE 10 illustrates these various parameters.

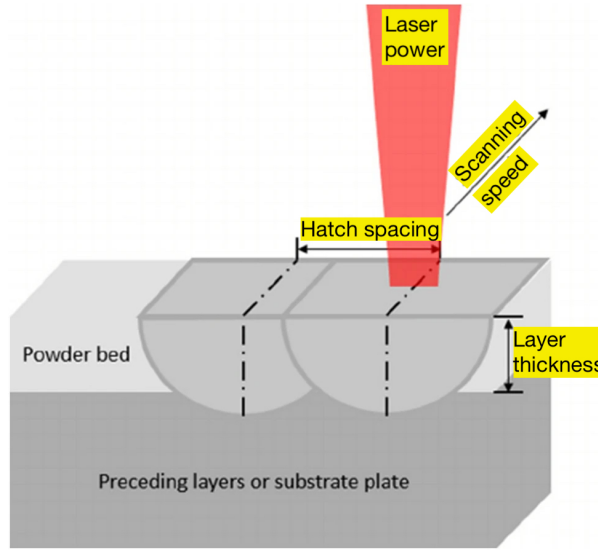


Figure 10: Illustration of all four parameters that contribute to the Ed used in LPBF [59].

These four elements are crucial for ensuring good quality. In addition to having a good overall combination (where Ed must be in appropriate values), each independent element has its importance.

- **Laser Power**

The choice of the appropriate laser power is crucial. The laser power cannot be too low as enough laser power is needed to fully melt the powder layers. Too low laser power may result in partial melting, leading to incomplete fusion of the powder layers. On the other hand, excessively high laser power should be avoided as it can induce the formation of a deep keyhole, introducing pores [43].

- **Scanning Speed**

The choice of scanning speed is also crucial. The scanning speed plays a vital role in

impacting the density and microstructure of a part, as a low scanning speed can lead to irregularities and distortion. Conversely, a high scanning speed can induce a warping phenomenon [60].

One way of selecting these two printing parameters is the single track. In a single track, a single layer of material is deposited and then melted by the laser [57]. On this layer, several El (EQUATION 1), i.e. a combination of scanning speed and laser power, are tested. An analysis of the microstructure is then carried out with the aim of rejecting parameters that lead to too many defects [61].

- **Hatch Spacing**

Hatch spacing defines the distance between centre lines of two adjacent tracks. The amount of overlap must be appropriately chosen to avoid poor fusion of particles. A small hatch distance will result in excessive overlap, which will then extend the manufacturing time [62]. In the other hand, a large hatch distance can limit the maximum layer height that can be used [63].

- **Layer Thickness**

The layer thickness must be sufficient to enable the manufacturing of parts. However, it is crucial to avoid excessive layer thickness as it could lead to defects such as balls, dimensional inaccuracies, and incomplete melting. Partial melting occurs when there is not enough time for the laser to fully reach the entire height of the powder layer [59].

In addition to these four parameters, the scanning strategy can also influence the result of the part but is not related to Ed. The scanning strategy is the spatial displacement pattern of the laser. It varies based on different scanning directions, scanning sequence, rotation angle of the scanning vector, length of the scanning vector, scanning time and hatch space [64]. FIGURE 11 illustrates some of scanning strategy.

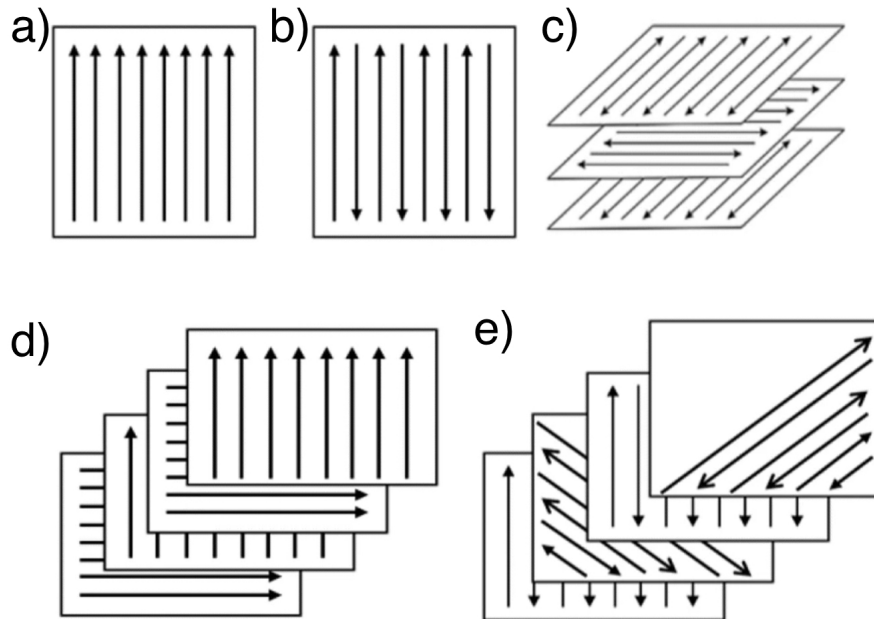


Figure 11: Schematic of different types of scanning strategy. (a) uni-directional scan, (b) bi-directional scan, (c) bi-directional, 90° rotation of scan, (d) 90° rotation of uni-directional scan between successive layers, (e) 45° rotation of scan vector [64].



The right choice of scanning strategy can reduce the defects created during printing. Indeed, the non-uniform thermal gradients induced during printing can lead to defects. These include residual stresses and poor surface finish. A scanning strategy can deal with the problem of thermal gradients during the heating and cooling phases [65].

## 2.2 High Entropy Alloys (HEAs)

### 2.2.1 Introduction

The conventional alloys are one of the most important discoveries in the field of metallurgy. Conventional alloys, primarily composed of a principal single element, have been used for millennia and have played a pivotal role in historical revolutions such as the Bronze Age, Iron Age and the Industrial Revolution [66]. In contrast to pure elements, alloys provide the ability to combine properties from multiple elements. To satisfy increasingly demanding needs, humans are developing and continuing to investigate new alloys with better properties [67]. The HEAs have made advances in this field, attributed to their internal arrangement and high entropy [66]. FIGURE 12 shows the evolution of engineering materials over time.

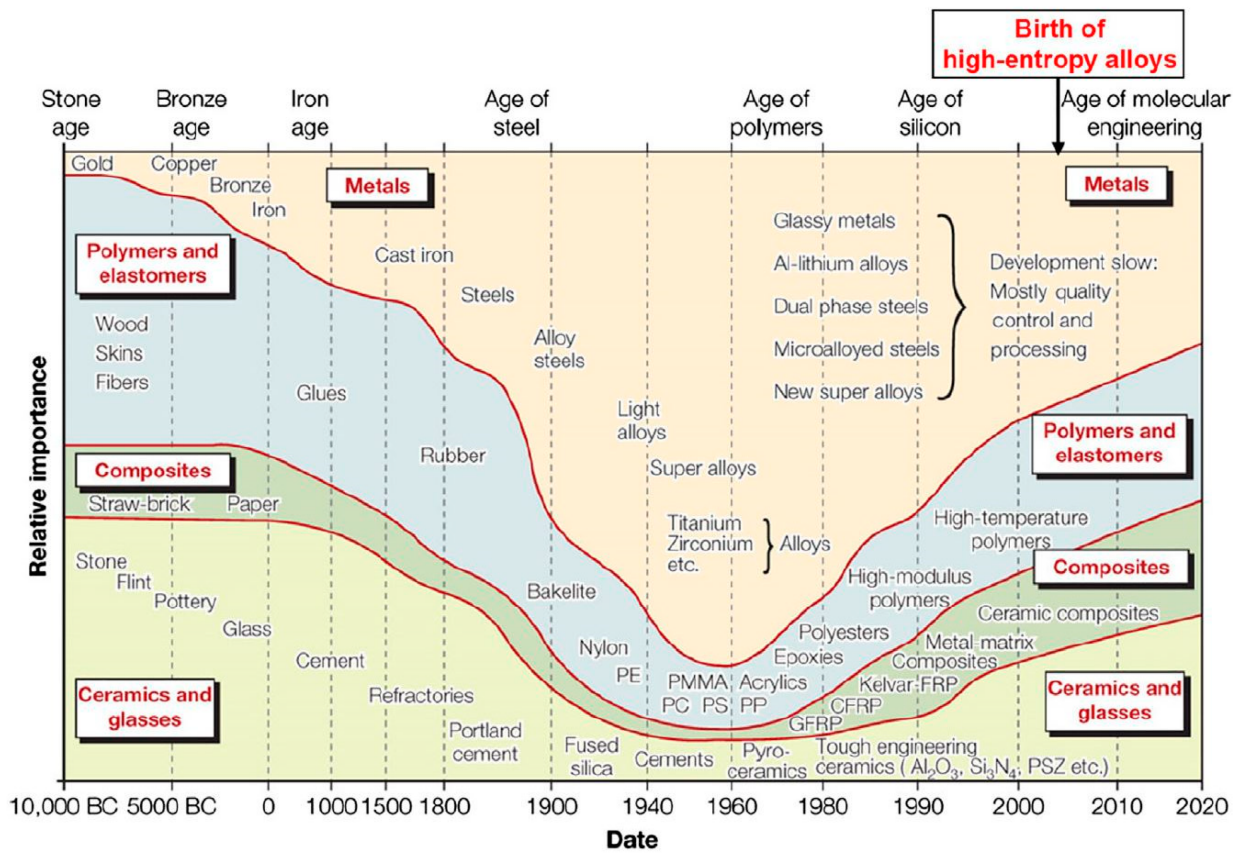


Figure 12: Evolution of engineering materials [68].

HEAs are a new category of alloys discovered simultaneously by two independent researchers, Cantor [69] and Yeh [70]. The two researchers published articles in 2004, after years of research [68]. Cantor et al. designed and prepared an equimolar CoCrFeMnNi alloy [68]. Using this alloy, Cantor et al. have investigated the unexplored central region of multicomponent alloy phase space [71]. Yeh et al. introduced the term HEA and its concept. Based on his own concept that high mixing entropy is linked to a reduction in the number of

phases in alloys, Yeh et al. have designed alloys with equi-atomic or close to equi-atomic chemical compositions [68]. Cantor and Yeh observed that their alloy formed a single phase [71].

HEAs represent a highly promising discovery in research due to their multitude of advantageous properties, such as corrosion resistance, high fatigue strength or high hardness. Owing to the growing interest in this field, HEAs are used in a variety of engineering domains, spanning from aerospace to nuclear, energy to chemistry, and automotive to biomedical. Their interest comes from their unique compositions, microstructures, and adjustable properties [72]. A schematic diagram of HEAs and how they differ from traditional alloys is shown in FIGURE 13.

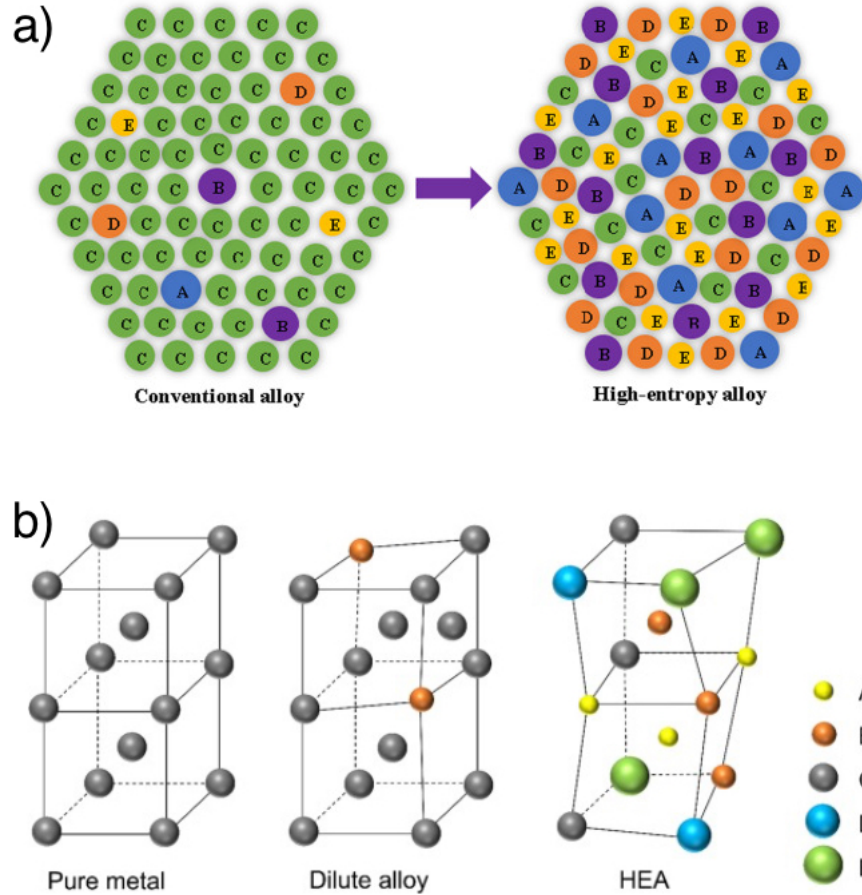


Figure 13: Schematic HEA and conventional alloy. A – E represent different element species in general. (a) Difference based on the atomic structure [4], (b) Difference based lattice distortion in body-centered cubic [67].

Regarding their production, the majority of HEAs are produced using traditional methods like conventional vacuum arc melting or induction melting, combined with casting; as well as through mechanical alloying associated by spark plasma sintering. However, recently, there is an increasing focus on creating HEAs through additive manufacturing. Due to the higher heating and cooling rates of this method ( $10^5$  to  $10^8$  K/s [22]), it can significantly inhibit atomic diffusion, thereby suppressing phase transition and intermetallic formation during the manufacturing process. This is, therefore, a considerable advantage for achieving a single-phase solid solution [5].



### 2.2.2 Definitions and interpretations

There is no single definition for HEAs. The two most common are based on the composition and entropy of alloys [73].

#### Definition Based on Composition

HEAs were initially defined as alloys composed of at least five principal elements in equimolar ratios. The definition has been extended to include alloys having these principal elements in concentrations ranging from 5 to 35 atm%. HEAs may also incorporate minor elements to modify the properties of the base HEAs [3].

#### Definition Based on Entropy

There are three groups of alloys according to their entropy. The three groups of alloys are as follows: high entropy alloys, (which have  $\Delta S_{\text{conf}} \geq 1.61 R$ ); medium entropy alloys, ( $1.61 R \geq \Delta S_{\text{conf}} \geq 0.69 R$ ), and low entropy alloys ( $\Delta S_{\text{conf}} \leq 0.69 R$ ) [3].

Entropy, a fundamental concept in thermodynamics, quantifies the degree of disorder or randomness in a system. The term "entropy configuration of a system" refers to the way in which particles or components are distributed in a system to maximise entropy [74].

The molar configurational entropy is defined by this equation:

$$\Delta S_{\text{conf}} = -R \sum_{i=1}^n X_i \ln X_i \quad (3)$$

where X is the mole fraction, and R is the perfect gas constant, i.e.  $8.31 \text{ J mol}^{-1} \text{ K}^{-1}$ .

This equation is based on the Boltzmann equation, a statistical thermodynamic equation. The Boltzmann equation is defined as follows:

$$\Delta S_{\text{conf}} = k \ln w \quad (4)$$

where k is Boltzmann's constant and w is the number of ways in which the available energy can be mixed among the particles of the system [68].

However, these two definitions are not automatically compatible. Specifically, the maximum configurational entropy of a 5-element HEA is  $1.61R$  (for the equimolar alloy), but the minimum value is  $1.36R$  (for an alloy with 5% A, 5% B, 20% C, 35% D and 35% E). Indeed, HEAs lack a universally agreed-upon definition, but there exist multiple interpretations. The term "multi-component" is also often used to cover these concepts [71].

### 2.2.3 The four core effects

HEAs are often defined as having four "core effects": the high entropy effect; the lattice distortion effect; the sluggish diffusion effect; and the 'cocktail' effect [75]. However, in recent years these effects have been debated.

- **High Entropy Effect**

An entropy greater than  $1.63 R$  (HEAs definition) is considered sufficiently high to avoid the enthalpies of the formation of intermetallic phases, resulting in stable solid solutions

[3]. Indeed, a higher mixing entropy in HEAs reduces the free energy of solid solution phases, facilitating their formation, especially at higher temperatures. The free energy is defined by the Gibbs equation as follows:

$$G = H - TS \quad (5)$$

where  $G$  is Gibbs free energy,  $H$  is enthalpy,  $T$  is temperature and  $S$  is entropy.

According to this equation, entropy can stabilise a phase with higher entropy, provided that the temperature is sufficiently high. Therefore, it is very likely that solid solution phases become the stable phases in HEAs at elevated temperatures [76].

This theory was initially confirmed by examining the HEAs and the microstructures observed within each of them. This approach implicitly assumes that the alloys studied and the microstructures produced represent a random sample of all possible HEAs systems. However, the listed HEAs alloys are not a random sample of the hundreds of millions of potential HEAs alloy combinations. As explained above, given the definition of HEAs, there may be an infinite number. Furthermore, the HEA studies that have led to this "core effect" idea have certain biases. These include: the alloys are generally studied in the as-cast state; the elements and alloys are not randomly selected; the alloys studied often have low enthalpies of mixing; incomplete characterisation of the microstructure; and inconsistent classification of the SS phases [73].

- **Lattice Distortion Effect**

In HEAs, the lattice is composed of various types of elements, each with a different size. These size differences inevitably lead to lattice distortion. Larger atoms push against their neighbors, while smaller atoms have extra space around them. The deformation energy associated with lattice distortion increases the overall free energy of the HEA lattice [76].

- **Sluggish Diffusion Effect**

It has been proposed that the kinetics of diffusion and phase transformation in HEAs are slower than those of their conventional alloys. The observations that inspired the hypothesis of slow diffusion included the presence of nanocrystals in the cast material, high recrystallization temperatures, and the formation of nanocrystals or amorphous materials in thin films deposited by sputtering [3].

- **Cocktail Effect**

The cocktail effect states that there are mutual interactions between components. The overall characteristics of the alloy are conditioned by the configuration, dispersion and boundaries of the phases, as well as by the overall contribution of the properties of each phase to the constituents of the material. Nevertheless, each phase is presented as a solid solution with multiple compositions, considered as a composite on an atomic scale. Its aggregate performance results not only from the intrinsic properties of the elements in accordance with the mixing rule, but also from interactions between these elements and substantial deformation of the crystal lattice. Overall, the cocktail effect extends from a composite effect with multiple compositions on an atomic scale to a microscopic scale [75].

### 2.2.4 Properties of HEAs

For conventional alloys that contain only one main element, the dominant mechanical properties are dictated by the major element. For HEAs, their properties can be different from any of the constituent elements. The phases present are the main factor in controlling their mechanical properties, such as corrosion resistance or hardness [72]. The microstructure also has a major impact on the properties. It is influenced, among other things, by the modification of the HEA compounds, but also by its production method [71].

#### 2.2.4.1 Corrosion properties

Due to the high mixing entropy effect, HEAs tend to have simple structures rather than complex intermetallic compounds. This results in excellent corrosion properties, superior to those of conventional alloys. In particular, HEAs composed of Cr, Ni, Mo, Co, Cu or Ti have high corrosion resistance [77].

#### 2.2.4.2 Hardness properties

Because all the elements have different atomic radii, the alloy is subject to intense lattice distortion. This prevents the movement of dislocations and leads to very high strength and hardness. According to experimental studies, HEA alloys have hardness values ranging from 150 to 1200 HV [78].

In addition to the structural features of the HEAs that give them their specific properties, the properties are also linked to the phases present.

### 2.2.5 Phases property and influence of the elements

The two phases most frequently encountered in HEAs are the Face Centered Cubic (FCC) and Body-Centered Cubic (BCC) phases. According to experimental studies, FCC and BCC phases occur at 56% and 43% of samples respectively [71]. However, as shown in FIGURE 14, HEAs can present other phases, such as the sigma intermetallic phase.

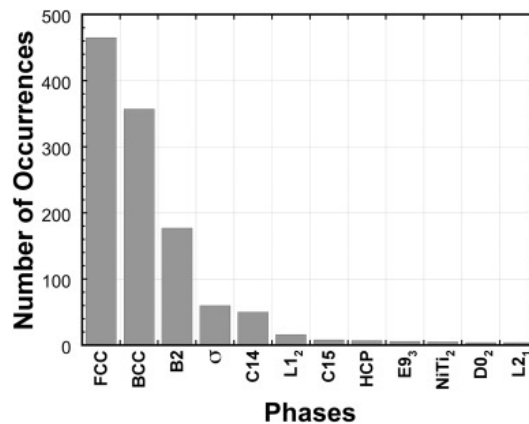


Figure 14: The number of times each phase is present in 648 studies on the microstructure of HEAs [71].

The FCC phase is a crystalline structure where atoms are arranged to form cubes, with atoms at the corners and an extra atom at the center of each face of the cube, as shown in FIGURE 15a. Similarly, the BCC phase refers to a crystalline structure where atoms are arranged to form body-centered cubes, with each atom located at a corner and an additional atom at the center of the cube, as shown in FIGURE 15b [79].

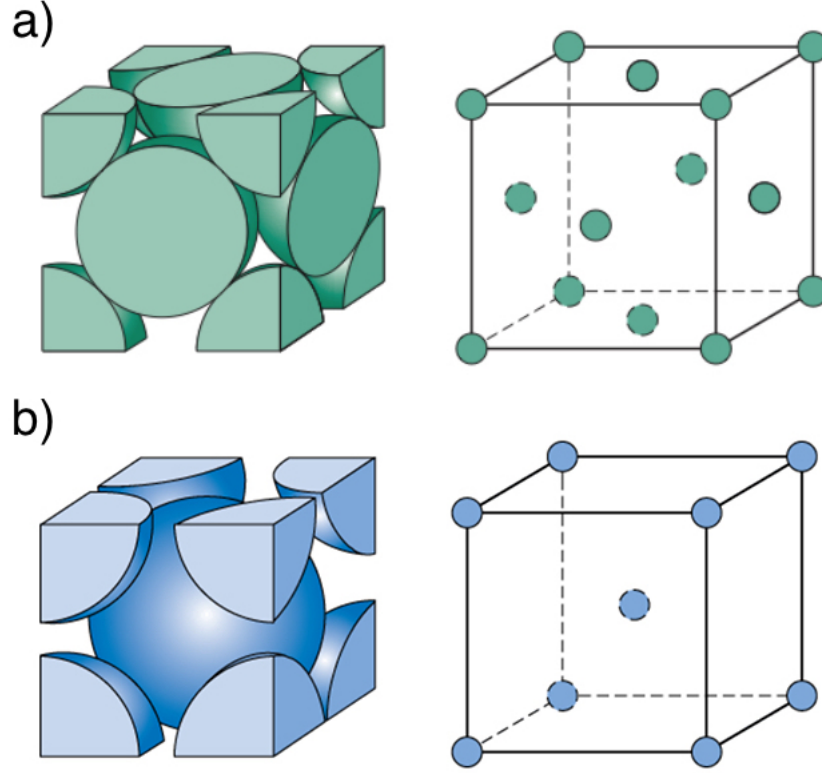


Figure 15: (a) Face Centered Cubic Structure, (b) Body-Centered Cubic Structure [80].

As said above, these two phases exhibit different behaviours concerning their mechanical properties. Regarding hardness, monophase FCC alloys show a Vickers hardness ranging between 100 and 200 HV, while monophase BCC alloys have a hardness higher than 600 HV. Alloys combining BCC and FCC phases demonstrate hardness values that increase from lower to higher levels with an increasing BCC content [71]. On the other hand, FCC phase has higher corrosion resistance [81].

As shown in FIGURE 14, the sigma phase, a complex phase which is an intermetallic compound, is also present in HEAs. The sigma phase is a very hard phase [82]. However, it decreases ductility and corrosion resistance and increases brittleness and cracks formation [83].

Predicting the phases present is thus essential when designing an alloy. To predict the formation of these complex phases, parameters derived from thermodynamics and physics have been proposed, based on the many experimental data on HEAs, [84]. Valence Electron Concentration (VEC) was used in this study.

The valence electron is intricately linked to the chemical reactivity of alloys, influencing the bonding and impacting the stacking of the structure. Electron concentration is determined as the mean number of itinerant electrons per atom, and the VEC encompasses all electrons,

including the d-electrons located in the valence band [85]. The VEC is expressed as follows:

$$\text{VEC} = \sum_{i=1}^n c_i \text{VEC}_i \quad (6)$$

where  $c_i$  is the atomic percentage of  $i$ th element,  $\text{VEC}_i$  is the VEC of  $i$ th element.

The VEC of the elements used in this thesis are listed in TABLE 3.

Table 3: VEC of the element [86].

Element	VEC
<b>Al</b>	3
<b>Mo</b>	6
<b>Cr</b>	6
<b>Fe</b>	8
<b>Ni</b>	10
<b>Mn</b>	7

This thesis uses two existing theories to predict existing phases as a function of the value of the VEC of the HEA.

A theory predicts that when the  $\text{VEC} \geq 8$ , FCC structure's solid-solution phase is formed. When  $6.87 \leq \text{VEC} < 8$ , both the FCC and BCC structure's solid-solution phases are formed. And when the  $\text{VEC} < 6.87$ , only a single BCC solid-solution phase is present [87].

The other theory, about the sigma phase, posits that, in HEAs containing chromium and/or vanadium, the sigma phase forms when the VEC falls within the range of 6.88 to 7.84 [82].

The presence of sigma phase was also estimated in a wider range than HEAs, using the Equivalent Chromium Content (ECC). The theory based on the equivalent chromium content posits that if the ECC (EQUATION 7) is greater than 17–18%, the alloy tends to form sigma phase [88].

$$\begin{aligned} \text{ECC} = & \% \text{Cr}(\text{wt}) + 0.31\% \text{Mn}(\text{wt}) + 1.76\% \text{Mo}(\text{wt}) + 0.97\% \text{W}(\text{wt}) \\ & + 2.02\% \text{V}(\text{wt}) + 1.58\% \text{Si}(\text{wt}) + 2.44\% \text{Ti}(\text{wt}) + 1.7\% \text{Nb}(\text{wt}) \\ & + 1.22\% \text{Ta}(\text{wt}) - 0.226\% \text{Ni}(\text{wt}) - 0.177\% \text{Co}(\text{wt}) \end{aligned} \quad (7)$$

In addition to these theories, it is also important to know the link between the elements and the phases present. It is well-established that aluminium [89] and chromium [90] promote the formation of BCC phase, while iron and nickel [91] act as precursors to the FCC phase. Molybdenum, on the other hand, can favour the formation of sigma phase precipitation or laves [92].

### 3 Materials and methods

In this chapter, the description of the materials and techniques employed in this study is provided. Both the powders and the prepared samples are detailed, along with all the equipment used, whether for the creation of the samples or their analysis. The methodologies employed are also outlined.

#### 3.1 Original powders

To develop a corrosion-resistant alloy, several elements are selected. Based on the known influence of elements on the microstructure and the properties of the alloys (SECTION 2.2.5), the elements listed in TABLE 4 were chosen. The 316L steel powder, which contains most of the selected elements, was also employed for this study (ANNEX A). In TABLE 5, the chemical composition of the 316L steel powder is shown.

Elemental powders were added to 316L steel powder to achieve the desired compositions. The elemental powders include powders of Al, Mo, Cr, Ni, and Mn. These powders and their morphology were observed using Scanning Electron Microscopy (SEM). The morphology of the powders is shown in FIGURE 16. The Ni and 316L steel powders have spherical morphology, whereas the other powders, namely Al, Mo, Cr, and Mn, are irregular in shape.

Table 4: Selected elements used in this work.

Element	Chemical symbol
Nickel	Ni
Aluminium	Al
Iron	Fe
Chromium	Cr
Manganese	Mn
Molybdenum	Mo

Table 5: Chemical composition of the 316L steel powder.

Powder	Comp % wt										
	C	Cr	Fe	Mn	Mo	Ni	N	O	P	Si	S
<b>316L</b>	0.021	17.6	65.723	0.91	2.24	12.6	0.09	0.03	0.008	0.67	0.008

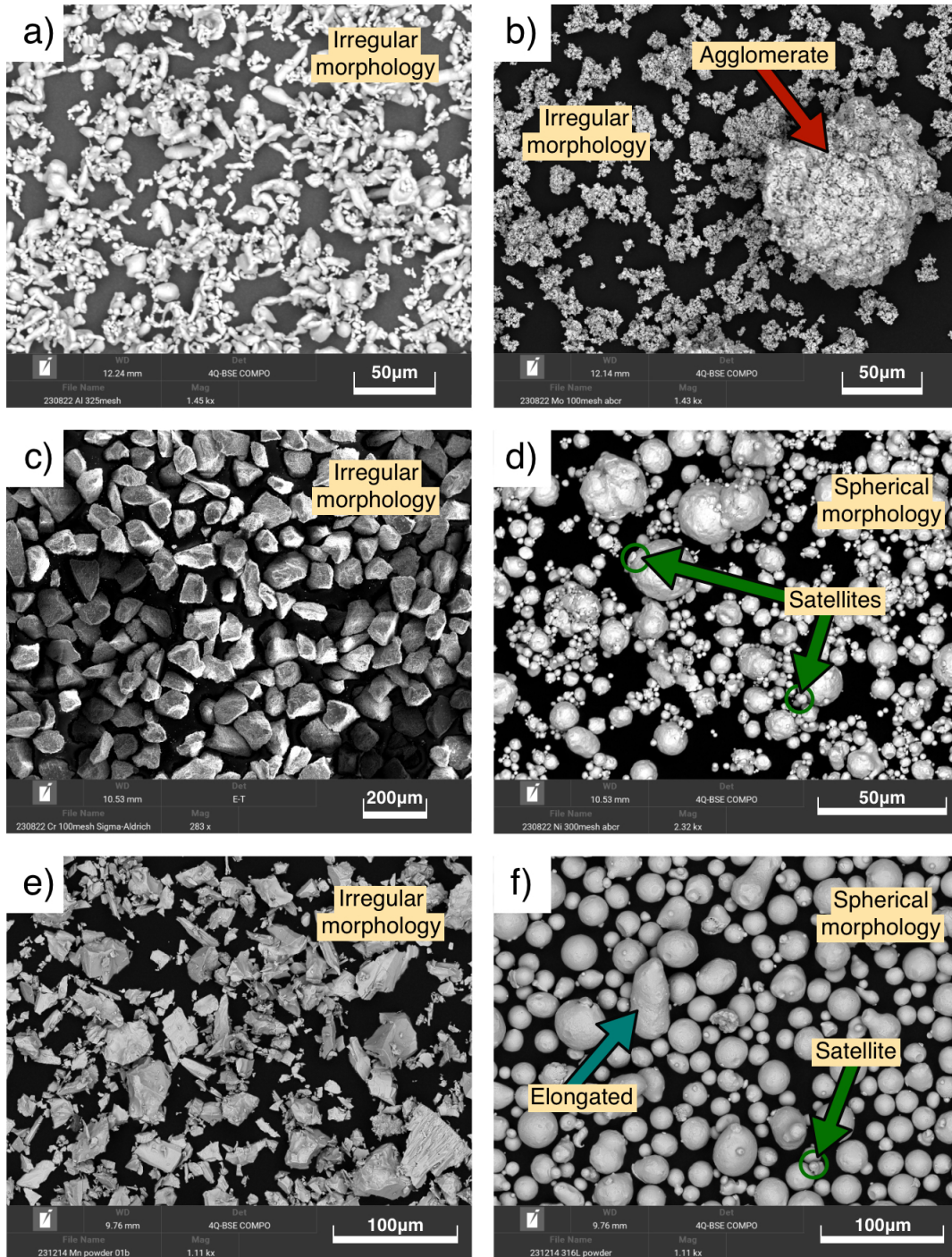


Figure 16: SEM micrographs of powders used. (a) Al powder, (b) Mo powder, (c) Cr powder, (d) Ni powder, (e) Mn powder, (f) 316L steel powder.

## 3.2 Powder preparation

### 3.2.1 Powder preparation for Differential Thermal Analysis (DTA)

Small quantities about 700mg were needed to make the DTA samples. The different powders were mixed manually for a few minutes.

### 3.2.2 Laser Powder Bed Fusion (LPBF) powder preparation

For use in the 3D printer, each elemental powder was first sieved, then the selected powders were manually mixed.

Single track experiments (SECTION 3.3.2.1) on the powder mixture with the detailed composition shown in TABLE 6 was carried out. The choice of this powder mixture was because it contains nearly all desired elements. Furthermore, the FCC phase is desired in the alloy because it has good corrosion resistance [81]. According to the element proportions, the alloy  $AlCrFe_2MnNi_2$  should exhibit a singular FCC phase. And the Thermocalc software, a thermodynamic calculation software used to predict phases and phase equilibrium in metallic alloys, also predicts full FCC for this alloy.

Table 6: Chemical composition of single track:  $AlCrFe_2MnNi_2$ .

Comp % atm				
Ni	Al	Fe	Cr	Mn
28.57	14.29	28.57	14.29	14.29

After more in-depth thought on the proportions of each element and spreadability tests carried out on certain mixtures (see SECTION 4.2.2), the composition detailed in TABLE 7 has been selected for cube printing.

Table 7: Chemical composition of LPBF printed cubes:  $Al_{0.2}Cr_{0.68}Fe_{1.79}MnMo_{0.1}Ni_{1.47}$ .

Comp % atm					
Ni	Al	Fe	Cr	Mn	Mo
28.05	3.82	34.16	12.98	19.08	1.91

The powders used for the single track and the LPBF printed cubes are illustrated in FIGURE 16.

To ensure the proper particle diameter of the powders, powders of Al, Fe, Ni, Cr and Mo were sieved using the sieve shakers HAVER EML 200 Premium [93] with mesh sizes of 63, 50 and 40  $\mu m$ . The device, as shown in FIGURE 17, induces vibrations of an amplitude of 1.5mm with an interval of time of 5 second to facilitate the passage of powders through the sieves. Haver & Boecker test sieve shakers produce a three-dimensional sieving motion. The screenings are accelerated vertically out of the meshes and simultaneously distributed over the screen surface in a circular motion. In this way, the sieving results are available quickly and they are also optimally reproducible at the same time [93].





Figure 17: HAVER EML 200 Premium.

The correct amount of powder, detailed in TABLE 8 for the single track and for LPBF printed cubes, was then weighed and mixed manually over a period of several hours.

Table 8: Powder used for single track of  $AlCrFe_2MnNi_2$ .

Powder	$AlCrFe_2MnNi_2$ Quantity [g]	$Al_{0.2}Cr_{0.68}Fe_{1.79}MnMo_{0.1}Ni_{1.47}$ Quantity [g]
Ni	264.40	621.58
Al	74.33	49.98
Cr	60.85	79.54
Mn	147.09	495.99
Mo	0	55.90
316L	468.17	1408.65

FIGURE 18 shows  $Al_{0.2}Cr_{0.68}Fe_{1.79}MnMo_{0.1}Ni_{1.47}$  after manually mixing during 5h.

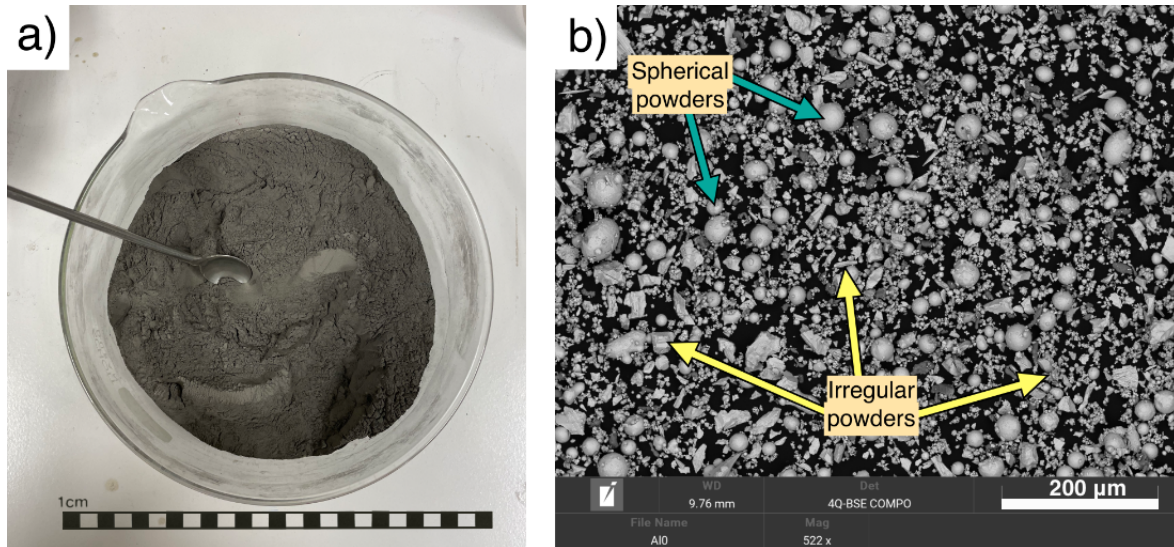


Figure 18:  $Al_{0.2}Cr_{0.68}Fe_{1.79}MnMo_{0.1}Ni_{1.47}$  after manually mixing. (a) Macroscopic view of  $Al_{0.2}Cr_{0.68}Fe_{1.79}MnMo_{0.1}Ni_{1.47}$ , (b) SEM-micrograph of  $Al_{0.2}Cr_{0.68}Fe_{1.79}MnMo_{0.1}Ni_{1.47}$ .

Thanks to the diversity of the powders' morphology, a well blended mix was observed. However, not all the powders have the expected spherical morphology required for LPBF printing. The irregular morphology of many powders has been observed.

### 3.3 Sample production

#### 3.3.1 Differential thermal analysis

DTA tests were performed using NETZCH STA 449C Jupiter DTA shown on FIGURE 19 [94]. The device can heat up the sample up to 1600°C and can perform a Thermo Gravimetric Analysis (TGA) simultaneously with the DTA. In addition, it has the capability to operate in either a high vacuum environment or under a protective atmosphere. The samples were produced through this method. The NETZCH STA 449C Jupiter DTA's capability to heat the samples to high temperatures enabled the melting of the powders. Upon cooling, solid samples were obtained. In DTA, the sample and an inert reference are subjected to identical thermal cycles, while recording any temperature difference between the sample and the reference. The resulting temperature difference is then plotted as a function of time or temperature, producing a DTA curve. Chemical reaction in the sample, whether exothermic or endothermic, can be detected in comparison to the inert reference. Therefore, a DTA curve provides data on the transformations that have occurred. It provides information regarding temperature changes and the heat absorbed or released by the sample per unit mass [94].



Figure 19: NETZCH STA 449C Jupiter DTA.

TABLE 9 lists the compositions of the various samples prepared and studied.

Table 9: Chemical composition of the DTA samples.

Sample	Comp % atm					
	Ni	Al	Fe	Cr	Mn	Mo
$Al_{0.1}Cr_2Fe_{3.4}Mn_1Mo_{0.2}Ni_{3.2}$	32.18	1.02	33.83	20	10	2
$CrFeMnNi$	25	-	25	25	25	-
$Cr_2Fe_2MnNi$	16.67	-	33.33	33.33	16.67	-
$CrFe_2MnNi_2$	33.33	-	33.33	16.667	16.67	-
$CrFe_2MnMo_{0.3}Ni_2$	31.75	-	31.75	15.87	15.87	4.76
$AlCrFeMnNi$	20	20	20	20	20	-
$AlCrFe_2MnNi_2$	28.57	14.29	28.57	14.29	14.29	-
$AlCrFe_2Ni_2$	33.33	16.67	33.33	16.67	-	-
$AlCrFe_2MnMo_{0.3}Ni_2$	27.4	13.7	27.4	13.7	13.7	4.1
$AlCrFe_2Mo_{0.3}Ni_2$	31.75	15.87	31.75	15.87	-	4.76

The DTA samples were produced to analyse and understand the various effects of the elements on the microstructure. The samples were heated up to 1550°C at 25°C/min and then cooled down to room temperature at 5°C/min.

### 3.3.2 Laser powder bed fusion

The LPBF printed cubes were produced using the AconityMINI printer [95], shown in the FIGURE 20. The AconityMINI has a build space of 140 mm of diameter, optionally reduced to



Figure 20: Aconity MINI printer.

55 mm of diameter. It has also full access to all relevant process parameters. It enables efficient material exploration and rapid part production, including for small batches. The AconityMINI is highly gas-tight, with low residual oxygen levels ( $< 100$  ppm). Equipped with robust recirculation, the system can handle highly reactive materials that produce significant amounts of welding fumes.

Like all Aconity systems, the AconityMINI can be equipped with additional options such as pre-heating to 500°C, as well as a unique vacuum option and micro-configuration.

The AconitySTUDIO control software provides comprehensive control over all relevant process parameters and allows remote access via the web interface.

All the technical specifications of the printer are listed in the TABLE 10.

#### 3.3.2.1 Single track

To determine the most optimal printing parameters for the alloy studied, single track experiments were performed on the composition  $AlCrFe_2MnNi_2$ . 1kg of manually mixed powders has been prepared. The quantity of powder used for each element is given in TABLE 8.

Table 10: Specification of Aconity MINI SLM printer.

Build Space	Diameter of 140 mm Height of 200 mm
Laser configuration	Single Mode Fibre 200W
Optics configuration / Spot size	F-Theta/ 50 $\mu\text{m}$ 3D Scanning / 80-500 $\mu\text{m}$
Pre-heating Temperature/ Build Space	500°C/ Diameter of 140 mm x Height of 180 mm
Max. Scan Speed	12m/s
Layer Thickness	Down to 10 $\mu\text{m}$
Inert gas Type/ Pressure	Argon 4.6 / 6 bars Nitrogen / 6 mbar Vacuum / < 2 mbar
Residual Oxygen content	<100 ppm
Pressurised air Type/ Pressure	ISO 8573-1:2010 [1:4:1]/ 6 bars

To select the final parameters, 53 tracks were performed with different parameters. The scanning speed varied from 200 to 2000 mm/s in increments of 200, and the laser power was tested at six different powers: 50, 100, 150, 175, 185, and 200W. These different parameters of scanning speed and laser power led to variations in  $E_l$  (EQUATION 1), in a range between 0.042 to 1 J/mm. ANNEX B includes the table detailing the laser power, scanning speed, and energy for each tested track.

Then the 53 tracks were analysed under an optical microscope to determine the optimal parameters. 15 pairs of laser power and scanning speed have been selected for printing cubes.

### 3.3.2.2 Cubes

Based on the analyses of the single tracks, the selected parameters are summarised in TABLE 11. The laser power varies between 150 and 200W, and scanning speed varies between 400 and 1200 mm/s. For the printing, other parameters such as the hatch distance, layer thickness, supply factor and scanning strategy were set at 90  $\mu\text{m}$ , 30  $\mu\text{m}$ , 4 and 90°/90° respectively. The volumetric energy density ( $E_d$ ) (EQUATION 2) varies between 50 and 125 J/mm<sup>3</sup>.

20 cubic samples (10mm x 10mm x 10mm) were printed with different parameters of scanning speed and laser power. The last five have the particularity of having two laser passes on each layer, as shown in the TABLE 11.

Table 11: 3D printing parameters.

Sample	Laser power [W]	Scanning speed [mm/s]	Volumetric Energy Density [ $J/mm^3$ ]	Number of laser passes
1	150	400	125.000	1
2	150	600	83.333	1
3	150	800	62.500	1
4	150	1000	50.000	1
5	175	400	145.833	1
6	175	600	97.222	1
7	175	800	72.917	1
8	175	1000	58.333	1
9	185	600	102.778	1
10	185	800	77.083	1
11	185	1000	61.667	1
12	185	1200	51.389	1
13	200	600	111.111	1
14	200	800	83.333	1
15	200	1000	66.667	1
16	150	800	62.500	2
17	175	800	72.917	2
18	185	800	77.083	2
19	200	800	83.333	2
20	200	1000	66.667	2

### 3.4 Pycnometer analysis

To determine the surface density of each sample produced using the 3D printer, the AccuPyc II Series 1345 Pycnometer [96] was employed, shown in FIGURE 21. This pycnometer is a gas pycnometer.



Figure 21: AccuPyc II Series 1345 Pycnometer.

Gas pycnometry is recognised as one of the most reliable techniques for obtaining true, absolute, skeletal, and apparent volume and surface density. This non-destructive technique utilises the gas displacement method to measure the volume of a material. Inert gases, such as helium or nitrogen, are commonly used as the displacement medium for gas pycnometry. The test conducted during this study was done with helium. Surface density determinations from the gas displacement method are more accurate, reproducible, and faster than the traditional

Archimedes water displacement method [96].

By precisely measuring the volume occupied by the sample inside the pycnometer, the surface density of the cubes is calculated.

For each sample, five tests were performed. The five given values were then averaged to obtain the surface density value for each sample.

The relative density of each sample can also be calculated. The density of the alloy is calculable by knowing the density and quantity of each element. The calculated value is then 7.86482 ( $\rho_{\text{bulk}}$ ). The relative density of each sample can be calculated using the following formula:

$$\% \text{ Density} = \frac{\rho \cdot 100}{\rho_{\text{bulk}}} \quad (8)$$

With  $\rho$  as the density evaluated by the pycnometer, and  $\rho_{\text{bulk}}$  as the theoretical density of the mixture.

### 3.5 Profilometer analysis

In order to analyse the surface of the printed samples, the Alicona InfiniteFocus G5 profilometer [97] was used, as shown in FIGURE 22.



Figure 22: Alicona InfiniteFocus G5.

Alicona InfiniteFocus G5 can generate 3D images that effectively emphasise surface characteristics while also having the capability to gauge the depth of the observed valleys. The magnification of the instrument's objectives can reach up to 100x. This apparatus employs a non-contact, three-dimensional optical measurement principle based on focal variation. The key component of the system comprises a precision optical setup housing multiple lens systems, which can be outfitted with various objectives, thereby enabling measurements with various magnification [97].

### 3.6 Microstructural characterisation

#### 3.6.1 Sample preparation

A well-polished surface is essential for using the microscope. The samples are first placed in Bakelite cylinder using Struers Citopress-1 [98].



The sample is then polished using STRUERS Tegramin-30 [98]. The polishing methodology employed starts with a pre-polishing step conducted with a rotational speed of 200 revolutions per minute (rpm) using abrasive clothes. Three papers with different grits were successively employed for 1 minute under water: SiC 400 paper, SiC 800 paper and SiC 1200 paper.

Subsequently, the final polishing step was carried out using synthetic material cloths with a rotational speed of 150 rpm. Four different clothes were utilised. MD Dac Cloth for 3 minutes with a  $9\text{ }\mu\text{m}$  diamond solution ( $9\text{ }\mu\text{m}$  is the diamond size in the solution), MD Nap Cloth for 3 minutes with a  $3\text{ }\mu\text{m}$  diamond solution, MD Nap Cloth for 2 minutes with a  $1\text{ }\mu\text{m}$  diamond solution, and finally, MD Chem Cloth for 5 minutes with an OPS diamond solution. All papers and products come from the supplier Struers [98].



Figure 23: STRUERS Tegramin-30.

The samples had to undergo another preparation step specifically tailored for SEM analysis. The SEM analyses relies on the electrical conductivity of the sample that must be sufficient to ensure that incoming electrons can be grounded. For this study, silver paint was used as conductive material. It bonds the sample embedded in bakelite to the support, as shown in FIGURE 24.

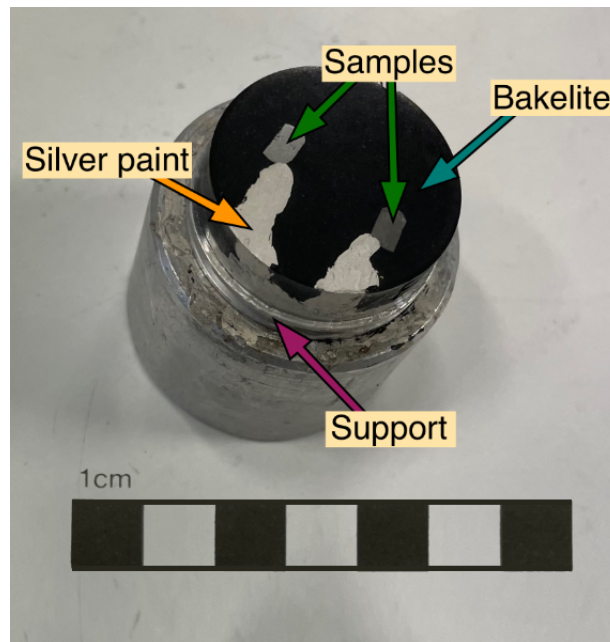


Figure 24: Sample prepared for SEM, in Bakelite and with silver paint.

Etching with nital (97% ethanol and 3% concentrated nitric acid) was achieved on the  $CrFeMnNi$  and  $Cr_2Fe_2MnNi$  samples. This helped to highlight the different phases that formed these samples, as well as the grain boundaries.

### 3.6.2 Optical microscope (OM) and Stream Analysis software

The samples were observed using the optical microscope Olympus BX60 [99], shown in FIGURE 25.



Figure 25: Olympus BX60.

Different magnifications (2.5x, 5x, 10x, 20x and 50x) were used for the observation of the microstructures. The microscope was used to acquire overviews of the samples, as well as more zoomed-in views to identify potential defects, such as porosity. Stream Analysis Software was used for image acquisition and processing. It is also used for the quantification of porosity and the quantification of the phases based on the different tints of the phases. The software relies on a manually established colour threshold to process the images.

### 3.6.3 Scanning Electron Microscope

Using the Tescan Clara Ultra-High Resolution SEM [100], shown in FIGURE 26, observations were conducted to enhance the scrutiny of samples owing to the microscope's higher magnification. For these direct observations, images of the samples were captured in Secondary Electrons mode. Profiles and the composition of specific points were acquired using Energy Dispersive Spectrometry (EDX), contributing to a more comprehensive understanding of the chemical composition in different zones. Furthermore, Electron Back Scattered Diffraction (EBSD) was employed to discern the distinct crystallographic lattices in various zones.





Figure 26: Tescan Clara Ultra-High Resolution.

### 3.7 Hardness

Macrohardness has been measured using EMCO M1C 010 [101], shown on FIGURE 27a. The EMCO M1C 010 gives sample hardness values in Vickers. The method is based on this principle, applying a load via a point, then measuring the imprint to calculate the hardness of the material (FIGURE 27b).

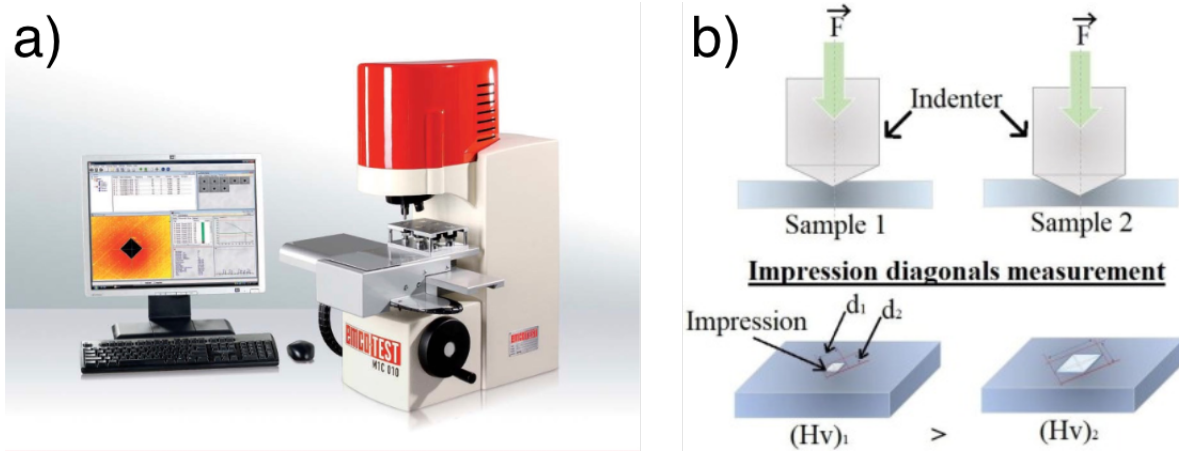


Figure 27: (a) EMCO M1C 010, (b) Schematic of Vickers hardness setup [102].

In Vickers hardness tests, the indenter is a diamond pyramid with a square base. The pyramid has a precise shape with an included angle between opposite faces of  $136^\circ$ . The square base of the pyramid creates a uniform load distribution during the indentation process. This allows reliable and reproducible hardness values to be obtained for different samples and test conditions [101]. The EMCO M1C 010 is used for low-load hardness testing, and gives hardness values in Vickers. Using the Vickers scale, the hardness is expressed in MPa. FIGURE 28 is an example of the trace left by EMCO M1C 010 after the load has been applied. The diagonals of the indentation are then measured to calculate the Vickers hardness. The formula for calculating Vickers hardness (HV) is as follows:

$$HV = \frac{2F \cdot \sin\left(\frac{136^\circ}{2}\right)}{9.80665 \cdot d^2} \quad (9)$$

where  $F$  is the applied force [N],  $d$  is the average of the print diagonals ( $d_1$  and  $d_2$  in FIGURE 28) [mm] and 9.80665 is a conversion factor between Newton and kilogram-force.

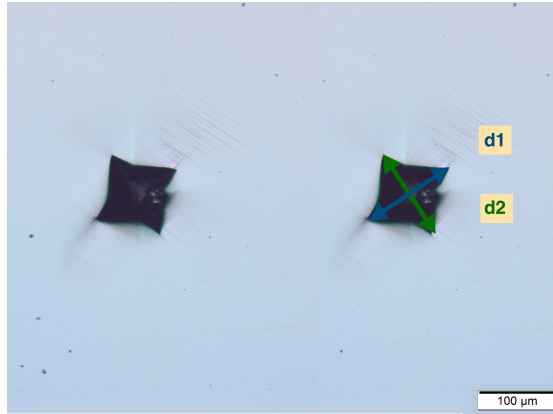


Figure 28: Optical micrograph of hardness Vickers indentation.

## 4 Results

The current chapter presents the results obtained from the study of near-equilibrium samples, where the solidification path and the microstructural characterisation will be examined. Subsequently, the chapter presents the results obtained from the analysis of the printed samples, where the spreadability and the optimal printing parameters will be discussed.

### 4.1 Differential thermal analysis samples

This section covers the results derived from the DTA samples. The DTA curves were used, as well as the observations made under the microscope, both OM and SEM micrographs. In addition, Energy Dispersive Spectroscopy (EDX) and electron backscatter diffraction (EBSD) were used to determine the composition and phases present. Since the solidification path is investigated, only the DTA cooling curves have been taken into account. After the analyses of the cooling DTA curves, OM and SEM-micrographs and EDX results, the DTA samples (TABLE 9) have been grouped based on their respective phases: one single phase microstructure, dual phase microstructure and triple phase microstructure. As will be shown in this chapter, the samples  $Al_{0.1}Cr_2Fe_{3.4}MnMo_{0.2}Ni_{3.2}$ ,  $CrFe_2MnNi_2$  and  $CrFe_2MnMo_{0.3}Ni_2$  have a single phase microstructure, the samples  $CrFeMnNi$ ,  $Cr_2Fe_2MnNi$ ,  $AlCrFeMnNi$ ,  $AlCrFe_2MnNi_2$  and  $AlCrFe_2Ni_2$  have a dual phase microstructure, and the samples  $AlCrFe_2MnMo_{0.3}Ni_2$  and  $AlCrFe_2Mo_{0.3}Ni_2$  have a triple phase microstructure.

#### 4.1.1 Single phase microstructure

$Al_{0.1}Cr_2Fe_{3.4}MnMo_{0.2}Ni_{3.2}$ ,  $CrFe_2MnNi_2$  and  $CrFe_2MnMo_{0.3}Ni_2$  samples are included in this group.

The cooling curves of these samples are shown in FIGURE 29. The curves share similarities, characterised by the presence of a prominent peak, indicative of a transformation from the liquid phase to the FCC phase.

The reaction or phase transformation associated to the peaks are presented in TABLE 12.

Table 12: Principal cooling peaks for  $Al_{0.1}Cr_2Fe_{3.4}MnMo_{0.2}Ni_{3.2}$ ,  $CrFe_2MnNi_2$  and  $CrFe_2MnMo_{0.3}Ni_2$  samples.

Peak	Start temperature [°C]	End temperature [°C]	Reaction or phase transformation
<b>A1</b>	1336	1300	Liquid to FCC
<b>B1</b>	1355	1283	Liquid to FCC
<b>C1 and C2</b>	1265	1235	Liquid to FCC + IM

$Al_{0.1}Cr_2Fe_{3.4}MnMo_{0.2}Ni_{3.2}$ ,  $CrFe_2MnNi_2$  and  $CrFe_2MnMo_{0.3}Ni_2$  samples exhibit a FCC single-phase matrix, as shown in FIGURE 30a. In the  $CrFe_2MnMo_{0.3}Ni_2$  sample, in addition to the FCC matrix, intermetallics (IM) were formed at grain boundaries, as shown FIGURE 30b.

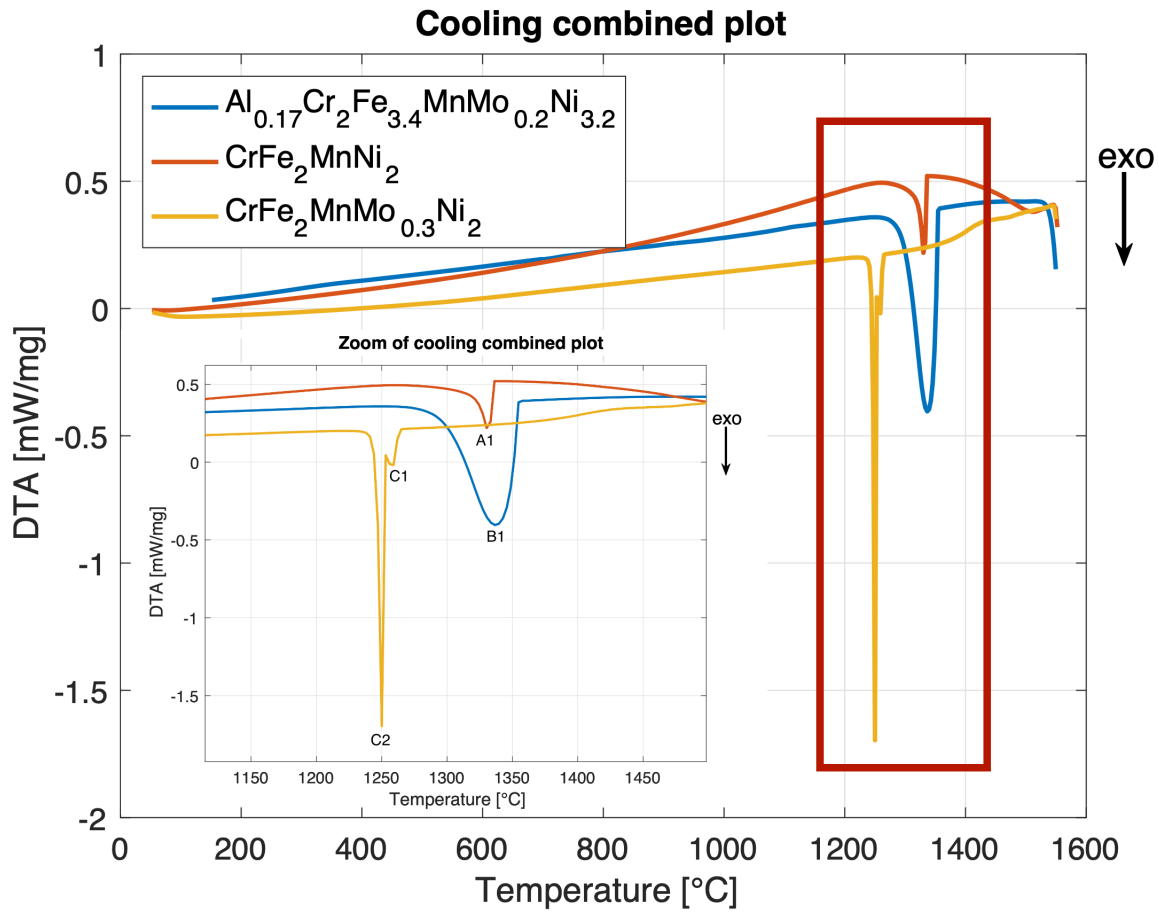


Figure 29: DTA cooling plot at 20°C /min for  $Al_{0.1}Cr_2Fe_{3.4}MnMo_{0.2}Ni_{3.2}$  and at 5 °C /min for  $CrFe_2MnNi_2$  and  $CrFe_2MnMo_{0.3}Ni_2$  samples.

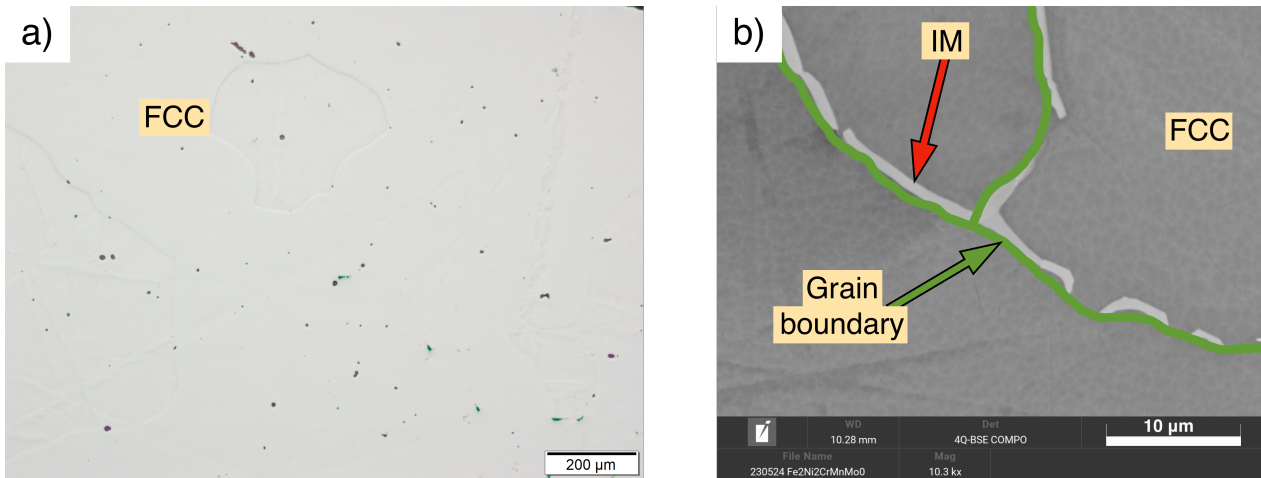


Figure 30: OM and SEM-micrographs of sample. (a) OM-micrograph of  $CrFe_2MnNi_2$  sample, (b) SEM-micrograph of  $CrFe_2MnMo_{0.3}Ni_2$  sample.

The composition of the different phases present in the microstructures was evaluated using EDX for semi-quantitative analysis, as shown in TABLE 13. EDX analysis shows that the IM phase is enriched in molybdenum, accounting for 16.2% by atomic percentage.

Table 13: EDX analysis of chemical composition of  $Al_{0.1}Cr_2Fe_{3.4}MnMo_{0.2}Ni_{3.2}$ ,  $CrFe_2MnNi_2$  and  $CrFe_2MnMo_{0.3}Ni_2$  samples.

Sample	Phase	Comp % atm					
		Al	Mo	Cr	Fe	Ni	Mn
$Al_{0.1}Cr_2Fe_{3.4}MnMo_{0.3}Ni_{3.2}$	FCC	0.0	$3.8 \pm 0.4$	$17.1 \pm 0.4$	$34.4 \pm 2.7$	$36.9 \pm 1.2$	$7.8 \pm 1.5$
$CrFe_2MnNi_2$	FCC	-	-	14.2	35.3	37.3	13.2
$CrFe_2MnMo_{0.3}Ni_2$	FCC	-	$5.7 \pm 0.2$	$17.4 \pm 0.2$	$35.5 \pm 0.3$	$28.9 \pm 0.4$	$12.5 \pm 0.2$
	IM	-	$16.2 \pm 4.6$	$25.3 \pm 3.6$	$31.3 \pm 1.0$	$17.6 \pm 5.8$	$9.7 \pm 1.5$

#### 4.1.2 Dual phases

$CrFeMnNi$ ,  $Cr_2Fe_2MnNi$ ,  $AlCrFeMnNi$ ,  $AlCrFe_2MnNi_2$  and  $AlCrFe_2Ni_2$  samples are included in this group.

In this group, two types of samples are identified according to their composition : the CrFeMnNi-based, including  $CrFeMnNi$  and  $Cr_2Fe_2MnNi$  samples; and the AlCrFeMnNi-based, including  $AlCrFeMnNi$ ,  $AlCrFe_2MnNi_2$ , and  $AlCrFe_2Ni_2$  samples.

##### 4.1.2.1 CrFeMnNi-based

The cooling curves of the CrFeMnNi-based samples are shown in FIGURE 31. Each of them exhibits the presence of two peaks, corresponding to two liquid-solid transformations. The reaction or phase transformation associated to the peaks are presented in TABLE 14. Some start and end temperatures of peaks cannot be identified (marked with "?" in the table). This is attributed to the occurrence of a new peak too close to the preceding one.

Table 14: Principal cooling peaks for  $CrFeMnNi$  and  $Cr_2Fe_2MnNi$  samples.

Peak	Start temperature [°C]	End temperature [°C]	Reaction or phase transformation
A1	1331	?	Liquid ( $L_0$ ) to FCC + $L_1$
A2	?	1247	Liquid ( $L_1$ ) to BCC
B1	1366	?	Liquid ( $L_0$ ) to FCC + $L_1$
B2	?	1264	Liquid ( $L_1$ ) to BCC

The microstructure of these samples is shown in FIGURE 32 for  $CrFeMnNi$  sample. The etching of nital revealed certain grain boundaries and highlights the two phases. The FCC and BCC phases are distinguishable. The composition of the different phases present in the microstructures was evaluated using EDX for semi-quantitative analysis. It was observed that the phase 1 (later identified as the FCC phase) is enriched in nickel, while the phase 2 (later identified as the BCC phase) is enriched in chromium, as shown in TABLE 15. To identify them, EBSD analysis was carried out on the samples.

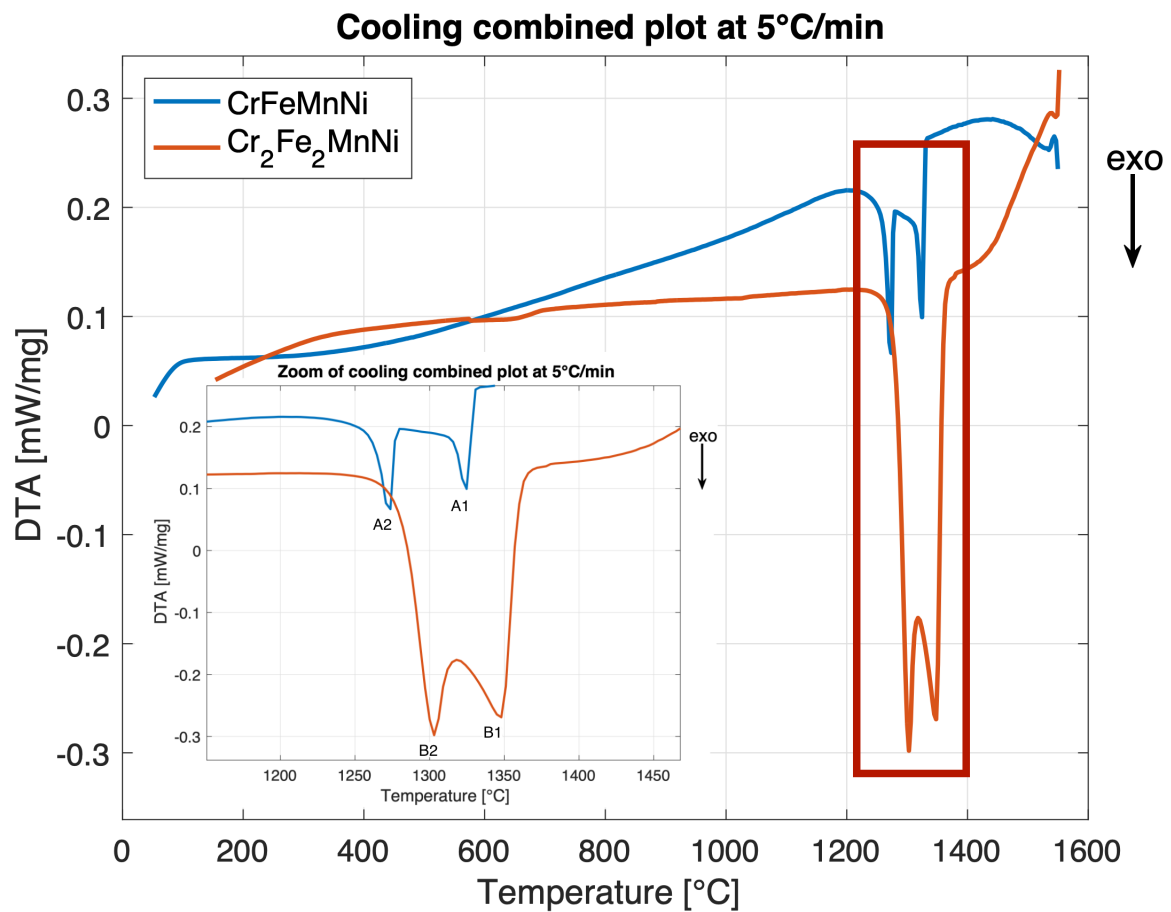


Figure 31: DTA cooling plot for *CrFeMnNi* and *Cr<sub>2</sub>Fe<sub>2</sub>MnNi* samples.

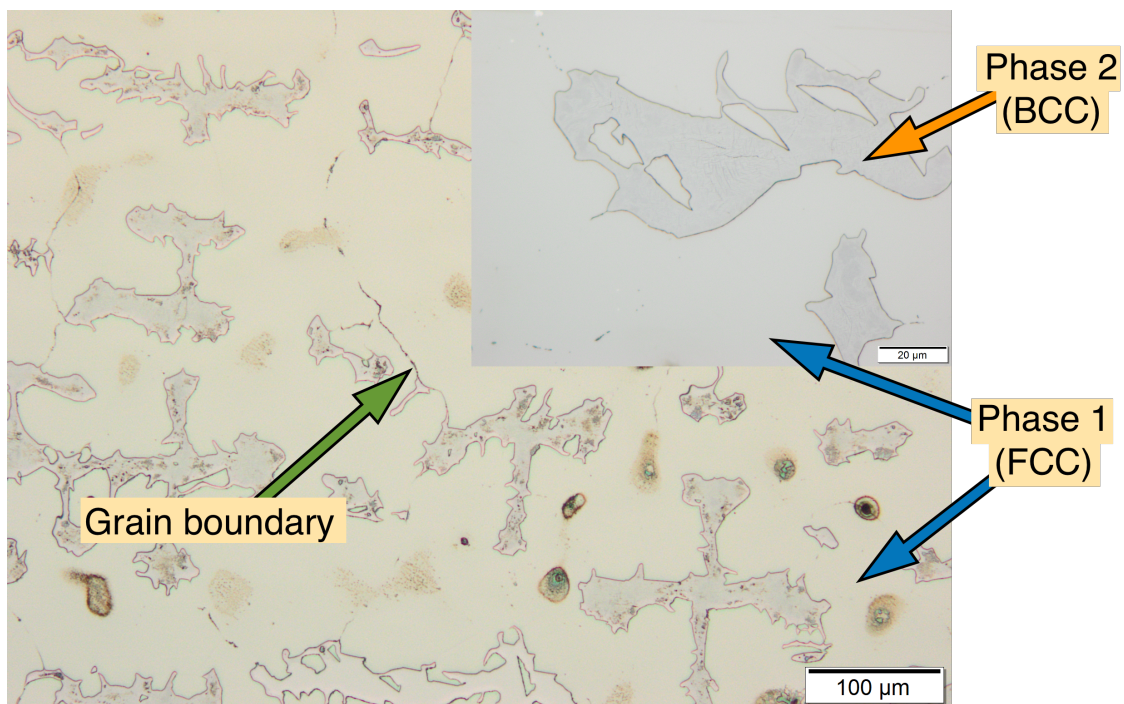


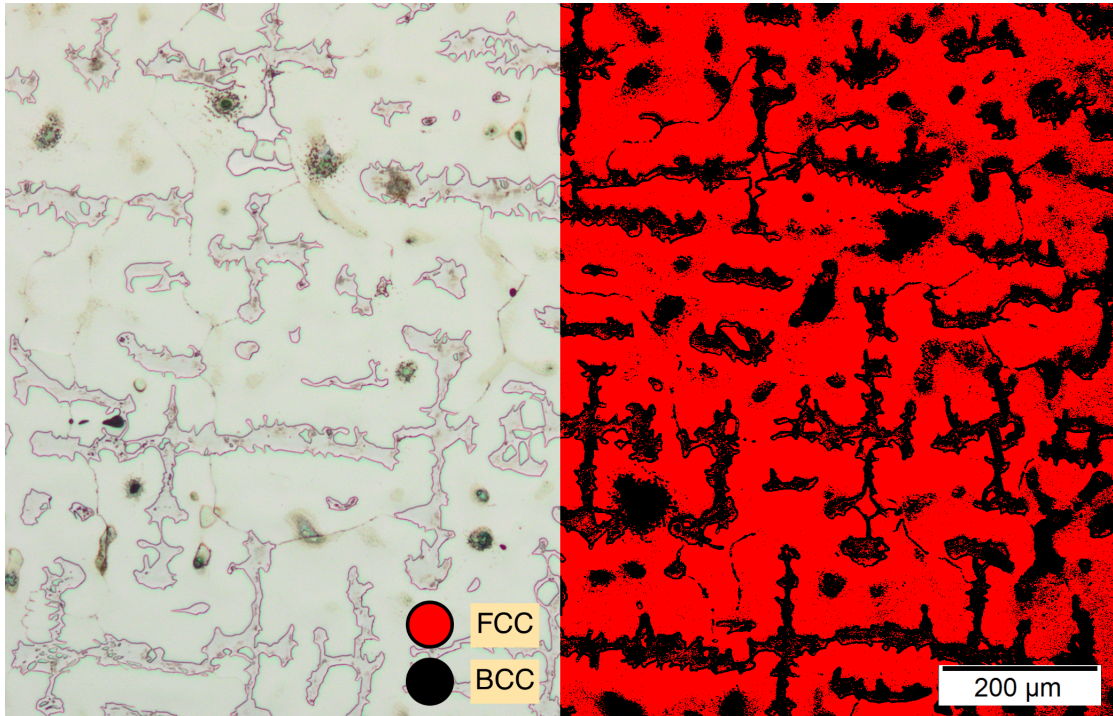
Figure 32: OM-micrograph of *CrFeMnNi* sample.



Table 15: EDX analysis of chemical composition of  $CrFeMnNi$  and  $Cr_2Fe_2MnNi$  samples.

Sample	Phase	Comp % atm			
		Cr	Fe	Ni	Mn
$CrFeMnNi$	Phase 1 (FCC)	$25 \pm 1.4$	$29.5 \pm 2.5$	$19.5 \pm 1.7$	$26 \pm 2$
	Phase 2 (BCC)	$46.2 \pm 2$	$30.3 \pm 1.0$	$6 \pm 1.4$	$17.5 \pm 0.4$
$Cr_2Fe_2MnNi$	Phase 1 (FCC)	$28.4 \pm 1$	$34.8 \pm 1.5$	$22 \pm 1.5$	$14.8 \pm 1$
	Phase 2 (BCC)	$47 \pm 0.7$	$33.2 \pm 0.5$	$8.9 \pm 0.5$	$10.9 \pm 0.4$

To quantify the two phases present in the microstructure, the Stream analysis software was used. This was applied on the optical micrograph of the  $CrFeMnNi$  sample after nital etching. FIGURE 33 shows the optical micrograph on the left side, and the image treated by Stream analysis software on the right side. The quantification of the two phases is calculated by measuring the red area for the FCC phase and the black area for the BCC phase in relation to the sum of these two areas. For each sample, the percentage results are indicated in TABLE 16.

Figure 33: Quantification of the phases in the microstructure of  $CrFeMnNi$ .Table 16: Quantification of the BCC and FCC phases for  $CrFeMnNi$  and  $Cr_2Fe_2MnNi$  samples.

Sample	Quantification of BCC	Quantification of FCC
$CrFeMnNi$	34.70%	65.30%
$Cr_2Fe_2MnNi$	40.30%	59.70%

#### 4.1.2.2 AlCrFeMnNi-based

The cooling curves of  $AlCrFeMnNi$ ,  $AlCrFe_2MnNi_2$ , and  $AlCrFe_2Ni_2$  samples are shown in FIGURE 34. Multiple peaks are observed, each representing a liquid-solid or a solid-state

transformation. The reaction or phase transformation associated to the peaks are presented in TABLE 17.

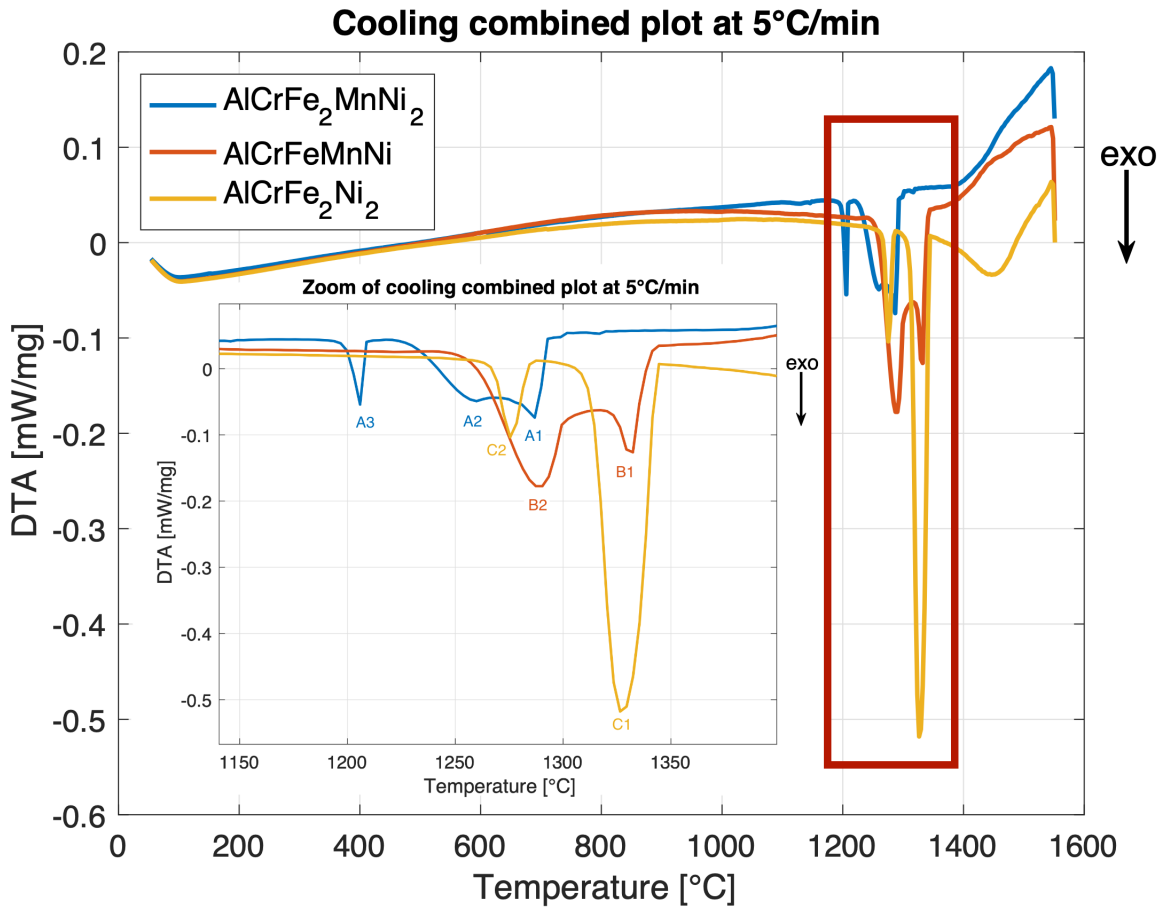


Figure 34: DTA cooling plot for  $\text{AlCrFeMnNi}$ ,  $\text{AlCrFe}_2\text{MnNi}_2$ , and  $\text{AlCrFe}_2\text{Ni}_2$  samples.

Table 17: Principal cooling peaks for  $\text{AlCrFeMnNi}$ ,  $\text{AlCrFe}_2\text{MnNi}_2$ , and  $\text{AlCrFe}_2\text{Ni}_2$  samples.

Peak	Start temperature [°C]	End temperature [°C]	Reaction or phase transformation
A1	1293	?	Liquid ( $L_0$ ) to FCC + $L_1$
A2	?	1227	Liquid ( $L_1$ ) to BCC
A3	1209	1197	BCC to BCC/B2 and BCC/A2
B1	1344	?	Liquid ( $L_0$ ) to FCC + $L_1$
B2	?	1254	Liquid ( $L_1$ ) to BCC
C1	1344	1305	Liquid ( $L_0$ ) to BCC/B2 + $L_1$
C2	1287	1263	Liquid ( $L_1$ ) to BCC/A2

The microstructure of these samples is shown in FIGURE 35.



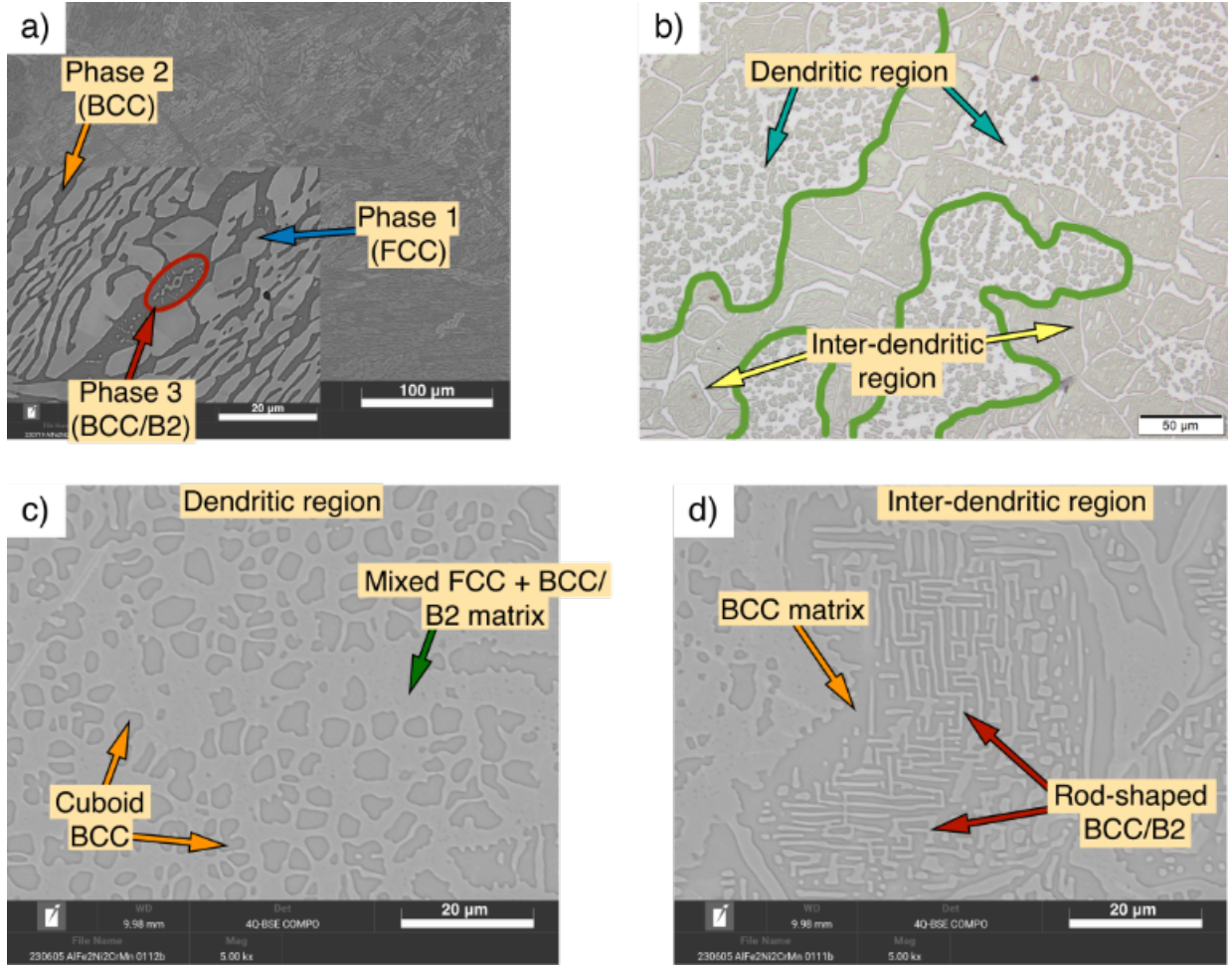


Figure 35: SEM and OM-micrographs of samples. (a) SEM-micrograph of  $AlCrFe_2MnNi_2$  sample, (b) OM-micrograph of  $AlCrFeMnNi$  sample, (c) SEM-micrograph of dendritic region of  $AlCrFeMnNi$  sample, (d) SEM-micrograph of inter-dendritic region of  $AlCrFeMnNi$  sample.

For  $AlCrFe_2MnNi_2$  and  $AlCrFe_2Ni_2$  samples, the microstructure has lamellar structure, as shown in FIGURE 35a. Three phases are distinguishable. The composition of the different phases present in the microstructures of  $AlCrFe_2MnNi_2$  and  $AlCrFe_2Ni_2$  was evaluated using EDX for semi-quantitative analysis. It was observed that the phase 1 (FCC) is enriched in chromium and iron, while the phase 2 (BCC) and phase 3 (BCC/B2) are enriched in aluminium and nickel, as shown in TABLE 18. To identify them, EBSD analysis was carried out on the samples.

Dendritic and interdendritic regions are only observed in the  $AlCrFeMnNi$  sample, as shown in FIGURE 35b. The dendritic and interdendritic regions are composed of both phases in different proportions. The organisation of the phases varies depending on whether they are in the interdendritic or dendritic region. Consistent with previous study [103], the dendritic region exhibits a mixed FCC + B2 matrix with high concentrations of chromium and iron. Within this matrix, cuboid precipitates rich in aluminium and nickel are embedded (FIGURE 35c). The interdendritic region features a BCC matrix abundant in aluminium and nickel, with rod-shaped BCC/B2 precipitates enriched in chromium and iron (FIGURE 35d). These results were confirmed by EDX for semi-quantitative analysis, as shown in TABLE 18.

Table 18: EDX analysis of chemical composition of  $AlCrFe_2MnNi_2$ ,  $AlCrFe_2Ni_2$  and  $AlCrFeMnNi$  samples.

Sample	Phase	Comp % atm				
		Al	Cr	Fe	Ni	Mn
$AlCrFe_2MnNi_2$	Phase 1 (FCC)	$4.7 \pm 0.4$	$18.6 \pm 0.9$	$39.6 \pm 0.6$	$22.9 \pm 0.8$	$14.2 \pm 0.3$
	Phase 2 (BCC)	$20.3 \pm 5.6$	$10.5 \pm 7.9$	$16.8 \pm 8.9$	$38.4 \pm 9.8$	$14 \pm 1.5$
	Phase 3 (BCC/B2)	$25.9 \pm 0.6$	$2.1 \pm 0.2$	$7.9 \pm 0.4$	$48.1 \pm 0.5$	$15.9 \pm 0.5$
$AlCrFe_2Ni_2$	Phase 1 (FCC)	$6.8 \pm 0.5$	$22.8 \pm 0.1$	$42 \pm 1.1$	$28.4 \pm 0.7$	-
	Phase 2 (BCC)	$27 \pm 1.6$	$10.4 \pm 2.9$	$18.6 \pm 1.8$	$44 \pm 3.2$	-
	Phase 3 (BCC/B2)	$29.8 \pm 0.8$	$4.9 \pm 0.3$	$14.2 \pm 0.4$	$51.1 \pm 0.1$	-
$AlCrFeMnNi$	Precipitates	$7.7 \pm 1.1$	$34.6 \pm 1.8$	$29.9 \pm 0.8$	$3 \pm 1.6$	$24.7 \pm 0.5$
	Matrix	$29.4 \pm 4$	$6.5 \pm 6$	$9 \pm 4.3$	$39.1 \pm 7.9$	$16 \pm 1.5$

EBSD analysis was carried out to complete the characterisation, identifying the phases present in  $AlCrFe_2MnNi_2$  and  $AlCrFe_2Ni_2$  samples. The pattern quality, shown in FIGURE 36a, is used to assess the quality of the data obtained from the EBSD analysis. The dark regions in the pattern quality indicate areas with poor indexing of lattice structure, resulting in low-quality or unreachable results. Examination of the crystal lattice revealed the existence of the FCC and BCC phases, as shown in the phase map in FIGURE 36b.

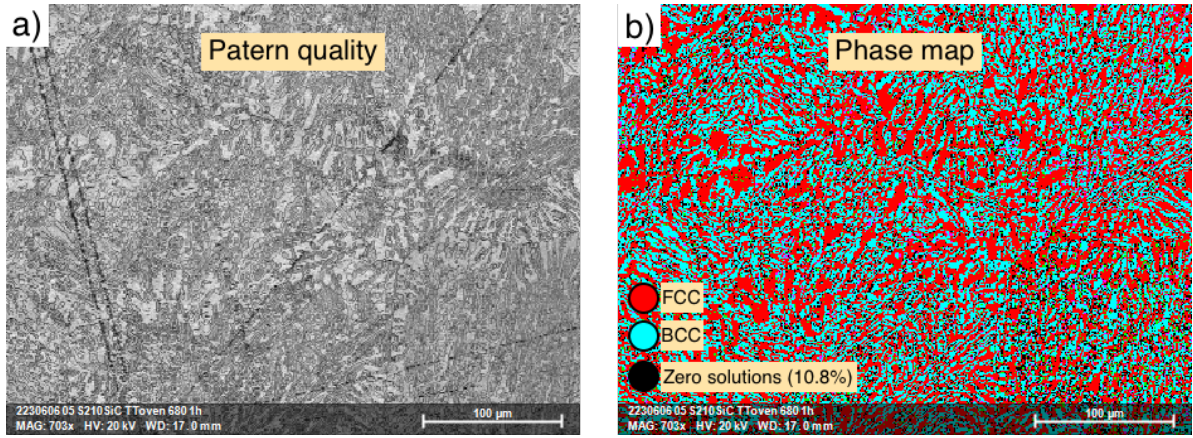


Figure 36: EBSD on  $AlCrFe_2MnNi_2$  sample (a) pattern quality, (b) phase map.

To quantify the two phases present in the microstructure, the Stream analysis software was used. This was applied on the optical micrograph of the  $AlCrFeMnNi$  and  $AlCrFe_2MnNi_2$  samples. FIGURE 37 shows, for these samples, the optical micrographs on the left side of each figure, and the images treated by Stream analysis software on the right side of each figure. The quantification of the two phases is calculated by measuring the red area for the BCC/B2 phase and the black area in relation to the sum of these two areas. In FIGURE 37a, the black area is the BCC phase. In FIGURE 37b, it is the FCC phase which is in black. For each sample, the percentage results are indicated in TABLE 16.

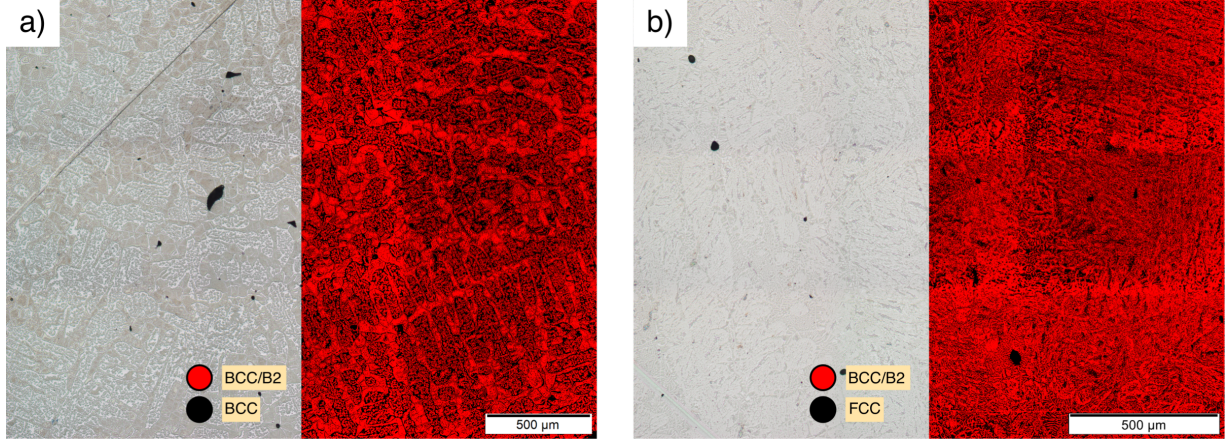


Figure 37: Quantification of the phases in the microstructure of AlCrFeMnNi-based samples. (a)  $AlCrFeMnNi$  sample, (b)  $AlCrFe_2MnNi_2$  sample.

Table 19: Quantification of the phases for  $AlCrFeMnNi$ ,  $AlCrFe_2MnNi_2$ , and  $AlCrFe_2Ni_2$  samples

Sample	Quantification of BCC	Quantification of BCC/B2
$AlCrFeMnNi$	43.10%	56.90%
Sample	Quantification of BCC/B2	Quantification of FCC
$AlCrFe_2MnNi_2$	60.20%	39.80%
$AlCrFe_2Ni_2$	47.40%	52.60%

#### 4.1.3 Triple phase

$AlCrFe_2Mo_{0.3}Ni_2$  and  $AlCrFe_2MnMo_{0.3}Ni_2$  samples are included in this group.

The cooling curves of these samples are shown in FIGURE 38. Multiple peaks are observed, each representing a liquid-solid or solid-state transformation. The reaction or phase transformation associated to the peaks are presented in TABLE 20.



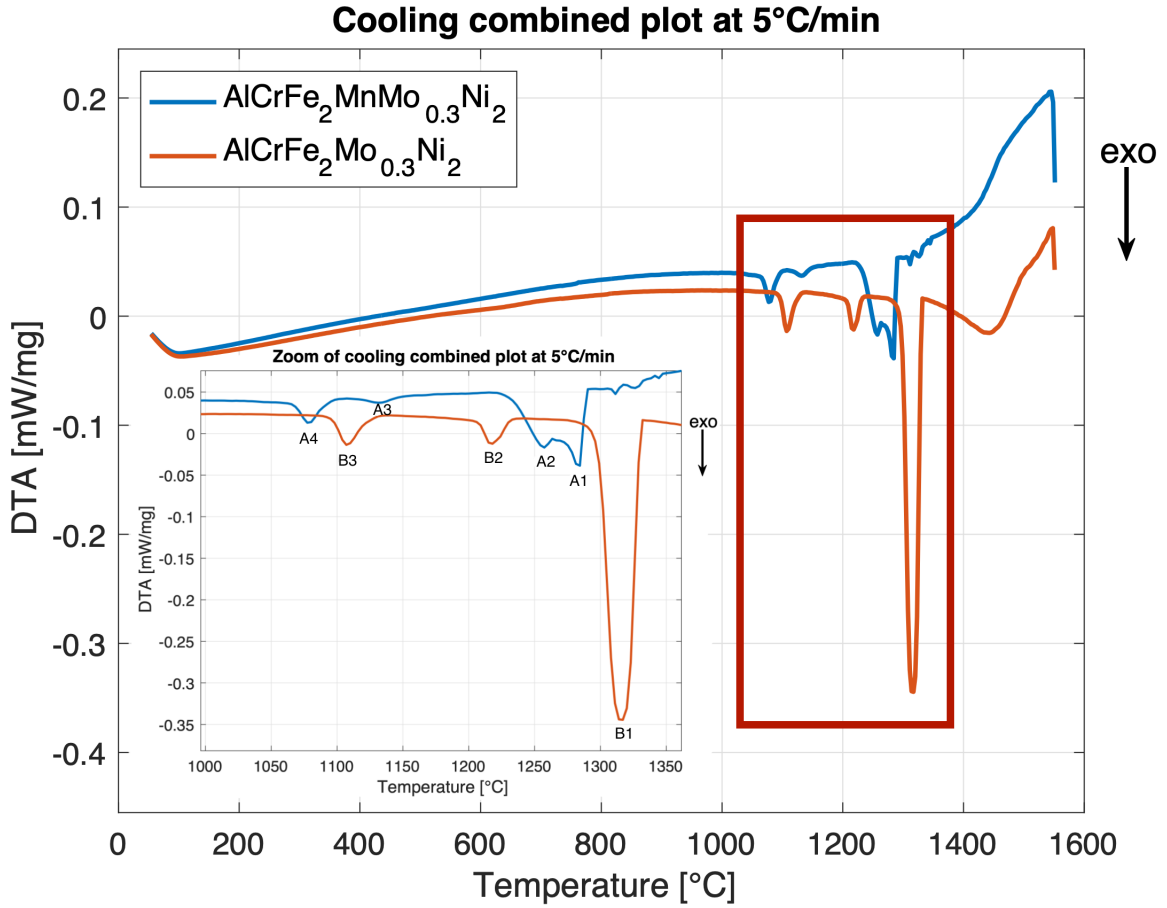


Figure 38: DTA cooling plot for  $AlCrFe_2Mo_{0.3}Ni_2$  and  $AlCrFe_2MnMo_{0.3}Ni_2$  samples.

Table 20: Principal cooling peaks for  $AlCrFe_2Mo_{0.3}Ni_2$  and  $AlCrFe_2MnMo_{0.3}Ni_2$  samples.

Peak	Start temperature [°C]	End temperature [°C]	Reaction or phase transformation
A1	1290	?	Liquid ( $L_0$ ) to FCC + $L_1$
A2	?	1221	Liquid ( $L_1$ ) to BCC
A3	1149	1119	BCC to BCC/B2 and BCC/A2
A4	1098	1065	FCC to Sigma
B1	1332	1287	Liquid to FCC
B2	1238	1206	FCC to BCC
B3	1128	1095	FCC to Sigma

$AlCrFe_2Mo_{0.3}Ni_2$  and  $AlCrFe_2MnMo_{0.3}Ni_2$  samples are characterised by the presence of three phases intricately imbricated in their microstructures.

FIGURE 39 shows the microstructure of these samples. The two microstructures are very similar. The composition of the three phases present in the microstructures were evaluated using EDX for semi-quantitative analysis. It was found that the BCC phase is enriched in aluminium and nickel, the FCC phase is rich in iron and chromium, and the sigma phase is enriched in molybdenum, as shown in TABLE 21.

BCC-rich areas are visible along the grain boundaries. In these areas the sigma phase is intricately shaped within the BCC phase. While inside the grains, there are regions with only the BCC phase and regions where the BCC phase is mixed with sigma phase in small lamellae, as shown in FIGURE 39a.

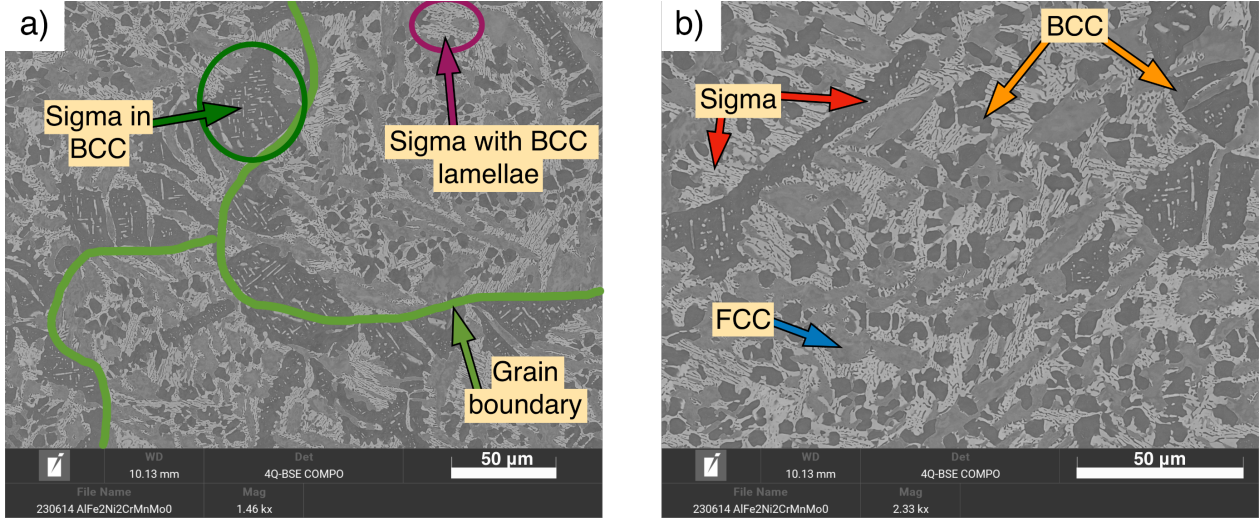


Figure 39: SEM-micrograph of  $AlCrFe_2Mo_{0.3}MnNi_2$ .

Table 21: EDX analysis of chemical composition of  $AlCrFe_2MnMo_{0.3}Ni_2$  and  $AlCrFe_2Mo_{0.3}Ni_2$  samples.

Sample	Phase	Comp % atm					
		Al	Mo	Cr	Fe	Ni	Mn
$AlCrFe_2MnMo_{0.3}Ni_2$	FCC	$5.5 \pm 0.3$	$3 \pm 0.2$	$14.6 \pm 0.2$	$35.8 \pm 0.8$	$25.9 \pm 0.3$	$15.2 \pm 0.3$
	BCC	$25.4 \pm 0.8$	$0.2 \pm 0.1$	$1.7 \pm 0.3$	$8.3 \pm 0.3$	$48.3 \pm 0.6$	$16.1 \pm 0.3$
	Sigma	$2.6 \pm 0.7$	$11.2 \pm 0.4$	$27.3 \pm 0.8$	$37.9 \pm 1.6$	$9.9 \pm 0.9$	$11.1 \pm 0.4$
$AlCrFe_2Mo_{0.3}Ni_2$	FCC	$6.7 \pm 0.8$	$4.2 \pm 0.1$	$18.2 \pm 0.2$	$40 \pm 1.1$	$31.1 \pm 0.5$	-
	BCC	$31.9 \pm 0.7$	$0.2 \pm 0.1$	$3.1 \pm 0.3$	$13.6 \pm 0.5$	$51.3 \pm 0.2$	-
	Sigma	$2.1 \pm 0.4$	$15 \pm 1.3$	$32.2 \pm 0.7$	$37.6 \pm 1.2$	$13.2 \pm 0.7$	-

## 4.2 Spreadability

Spreadability refers to the ability of metal powders layer to evenly and consistently cover the build platform during the powder deposition stage of the additive manufacturing process. As explained in SECTION 2.1.1.2, this characteristic is essential for a successful printing.

### 4.2.1 Single Track

Four different powder mixtures were prepared with the aim of achieving the best spreadability. Two different composition were prepared,  $CrFe_2MnNi_2$  and  $AlCrFe_2MnNi_2$ . Each of these compositions was produced twice, with a difference in the powders used, as shown in FIGURE 40.

Regarding the composition  $CrFe_2MnNi_2$ , two types of Cr powders were tested. Non-spherical Cr powder of size  $10 \mu m$ , as depicted in FIGURE 40a, and larger non-spherical

Cr powder, of  $149\ \mu\text{m}$ , as illustrated in FIGURE 40b.

For the  $\text{AlCrFe}_2\text{MnNi}_2$  composition, the variation was examined in the Ni powders. In one case, Ni cuboid-shaped powder was used, as shown in FIGURE 40c, and in the other case, Ni spherical powder was used, as shown in FIGURE 40d.

To test the spreadability, in the printer using the scraper, a thin layer of powder of each preparation was spread, as shown in FIGURE 40. It was then evaluated visually.

The  $\text{CrFe}_2\text{MnNi}_2$  composition, prepared with the  $10\ \mu\text{m}$  Cr powders, shown in FIGURE 40a, presents a good spreadability. The  $\text{AlCrFe}_2\text{MnNi}_2$  composition, prepared with Cuboid Ni powders, shown in FIGURE 40c, presents a bad spreadability, with a lot of caking. The  $\text{CrFe}_2\text{MnNi}_2$  prepared with the  $149\ \mu\text{m}$  Cr powders, shown in FIGURE 40b, and  $\text{AlCrFe}_2\text{MnNi}_2$  composition, prepared with spherical Ni powders, shown in FIGURE 40d, present an acceptable spreadability for 3D printing.

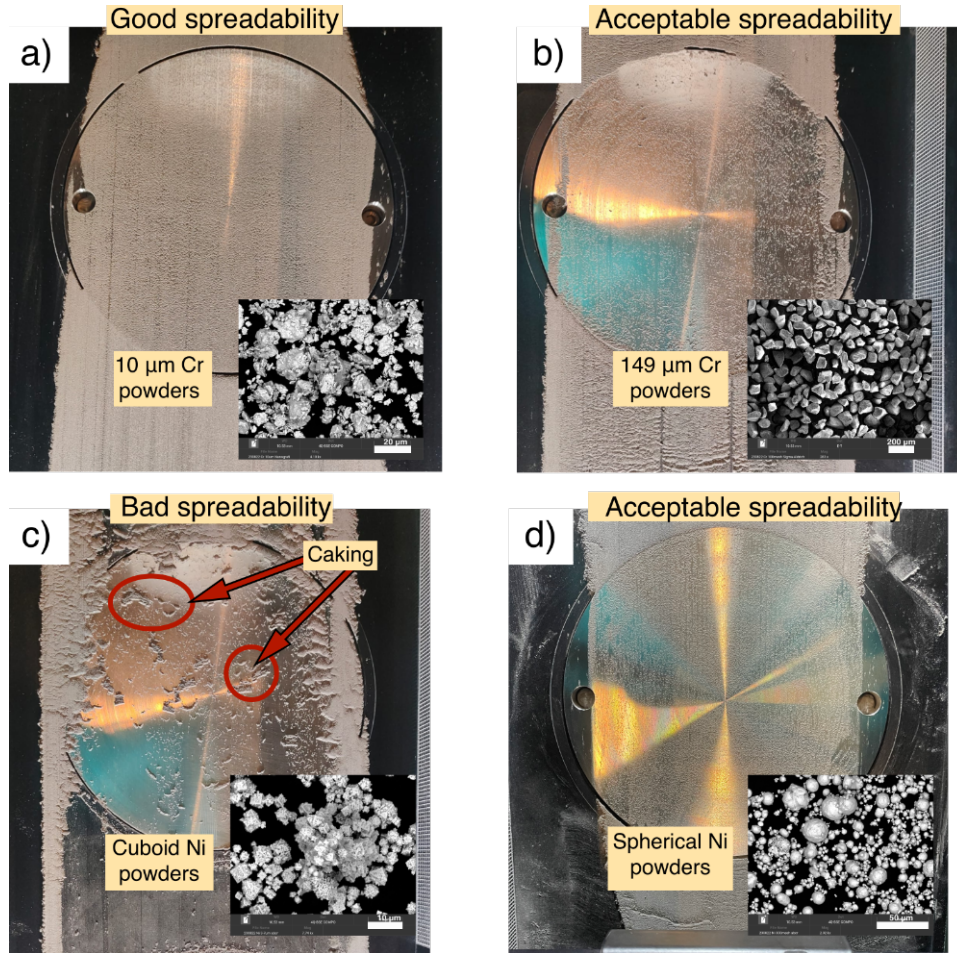


Figure 40: Test for spreadability. (a)  $\text{CrFe}_2\text{MnNi}_2$  with  $10\ \mu\text{m}$  Cr powders, (b)  $\text{CrFe}_2\text{MnNi}_2$  with  $149\ \mu\text{m}$  Cr powders, (c)  $\text{AlCrFe}_2\text{MnNi}_2$  with cuboid Ni powder, (d)  $\text{AlCrFe}_2\text{MnNi}_2$  with spherical Ni powder.



### 4.2.2 LPBF printed cubes

The composition initially chosen for printing was  $Al_{0.4}Cr_{0.7}Fe_{2.3}MnMo_{0.1}Ni_{2.3}$ . However, the spreadability of this powder mixture is poor. It is impossible to get a thin layer of powder without caking. The poor spreadability of the first mix is illustrated in FIGURE 41a.

The composition therefore had to be revised and was adjusted using  $Al_{0.4}Cr_{0.7}Fe_{2.3}MnMo_{0.1}Ni_{2.3}$  with the addition of 316L steel powder, which is a powder with an ideal morphology for LPBF. Other elements were also added in smaller quantities, to obtain a composition with a phase estimated by Thermocalc software, in equilibrium condition, as FCC. The printed alloy is then  $Al_{0.2}Cr_{0.68}Fe_{1.79}MnMo_{0.1}Ni_{1.47}$ . The composition is specified in TABLE 7. It was observed that pre-heating to 200°C also improves the spreadability of the powder mixture. FIGURE 41b shows the good spreadability of  $Al_{0.2}Cr_{0.68}Fe_{1.79}MnMo_{0.1}Ni_{1.47}$ .

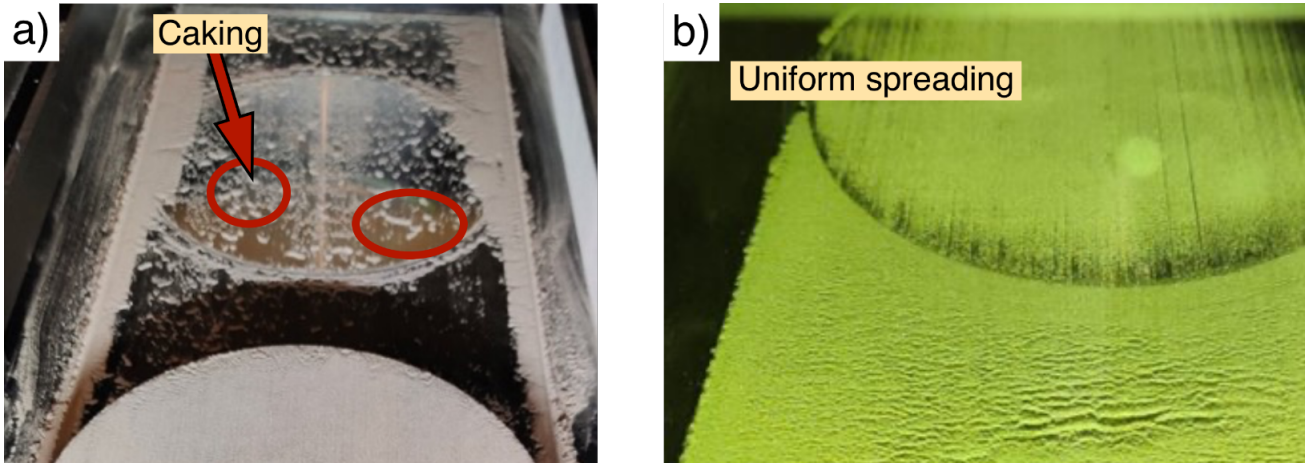


Figure 41: Effect of morphology of powder in spreadability. (a) Initial mix:  $Al_{0.4}Cr_{0.7}Fe_{2.3}MnMo_{0.1}Ni_{2.3}$ , (b) Mix after addition of 316L steel powder:  $Al_{0.2}Cr_{0.68}Fe_{1.79}MnMo_{0.1}Ni_{1.47}$  and pre-heating at 200 °C.

## 4.3 Laser powder bed fusion samples

### 4.3.1 Single tracks

As explained in SECTION 3.3.2.1, single tracks were made from on  $AlCrFe_2MnNi_2$  varying the laser power and scanning speed parameters between respectively 50 to 200W and 200 to 2000 mm/s. To select the optimal parameters, the tracks were examined with an optical microscope to identify three types of defects: unmelting and melting discontinuity, irregular and/or non-linear tracks, and powder spatter. FIGURE 42 illustrates these defects.

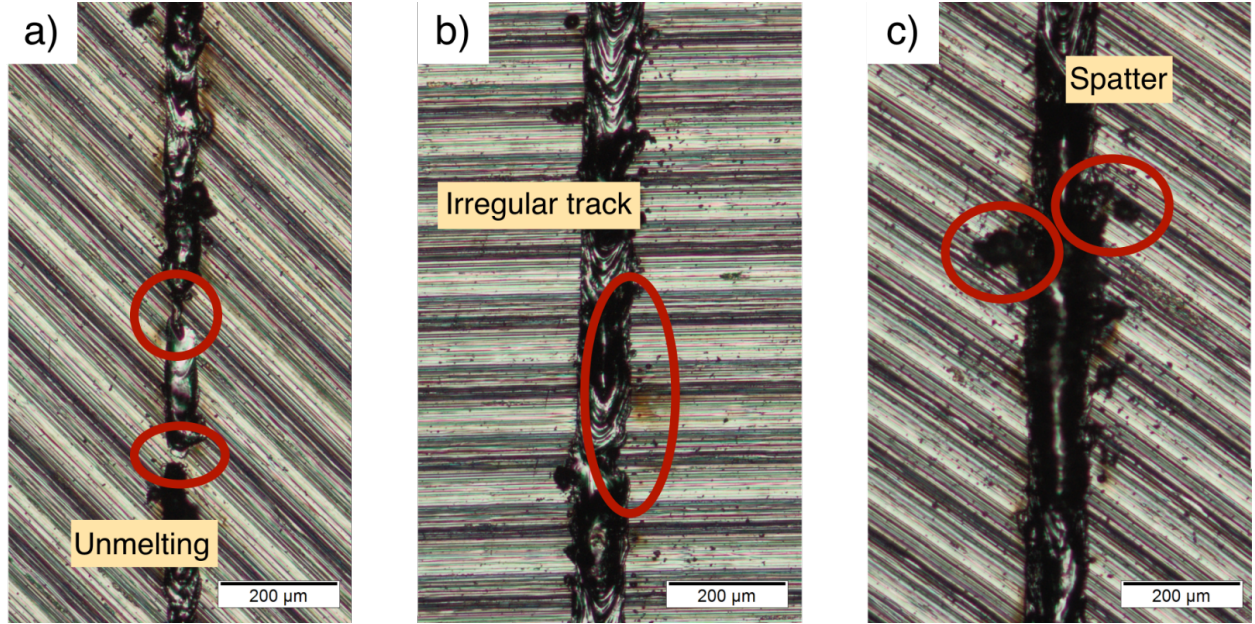


Figure 42: OM-micrographs of defects in single track  $AlCrFe_2MnNi_2$ . (a) Unmelting defect at 50W and 1200mm/s, (b) Irregular track defect at 150W and 1800mm/s, (c) Spatter defect at 175W and 1400mm/s.

The mean width of each track was measured. FIGURE 43 shows the evolution of the track width in relation to the laser power and scanning speed. The width decreases as the scanning speed increases and the laser power decreases.

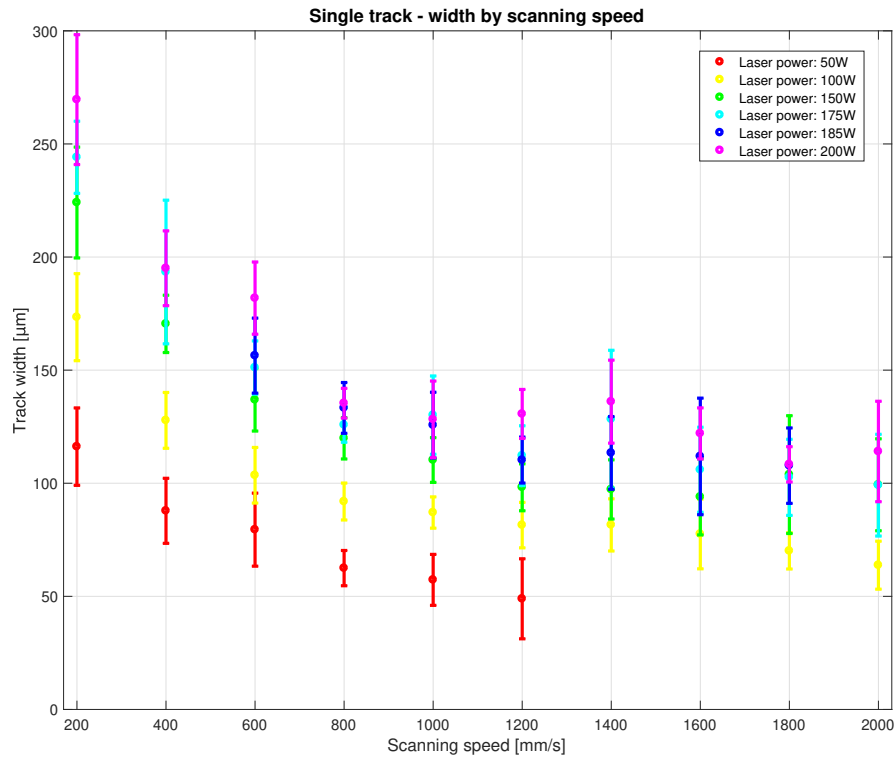


Figure 43: Width by applied parameters of  $AlCrFe_2MnNi_2$ .



FIGURE 44 shows the quality of each track according to the laser power and scanning speed parameters. 15 tracks, represented by green dots in FIGURE 44, show a sufficient quality. Because of their minor defects, the scanning speed and laser power parameters corresponding to these 15 tracks are selected for printing cubes. Their laser power parameters are set at 150 W or higher, while their scanning speed parameter is maintained at 1200 mm/s or lower.

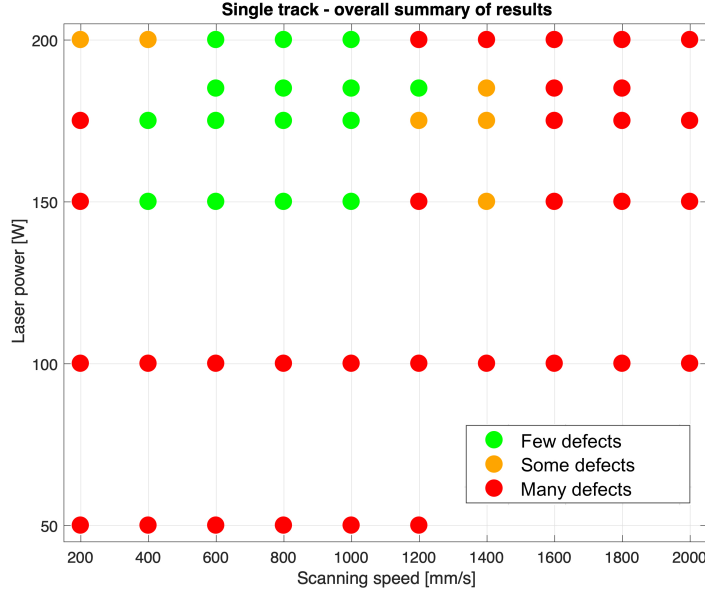


Figure 44: Quality of track based on laser power and scanning speed of  $AlCrFe_2MnNi_2$ .

#### 4.3.2 LPBF printed cubes

FIGURE 45 shows the 20 different printed samples, with variation of laser power, scanning speed and number of laser passes, as summarised in TABLE 11.

Of the 20 cubes printed, two of them, samples 1 and 5, were not printed correctly. Due to their poor surface quality, they were not systematically included in the studies conducted on the cubes.

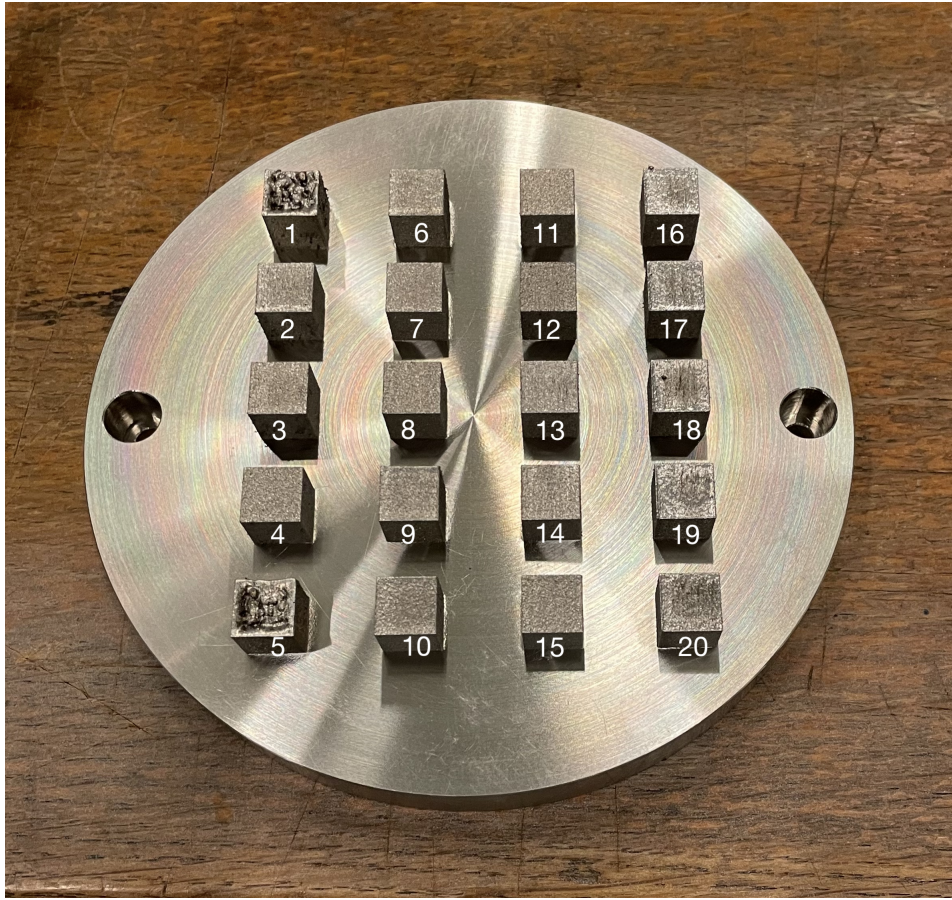


Figure 45: Cubes of  $Al_{0.2}Cr_{0.68}Fe_{1.79}MnMo_{0.1}Ni_{1.47}$  printed.

During printing, for samples 1 and 5, spatter was visible after the laser pass, as shown in FIGURE 46.

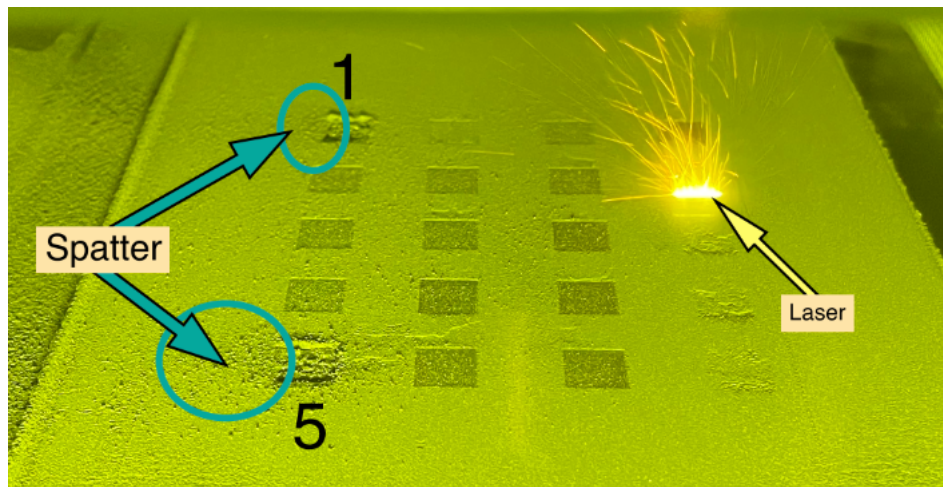


Figure 46: Defect during printing of  $Al_{0.2}Cr_{0.68}Fe_{1.79}MnMo_{0.1}Ni_{1.47}$ .

#### 4.3.2.1 Density

As explained in SECTION 3.4, the surface density of the printed cubes was determined using a pycnometer. The percentage surface density of each sample can be calculated

using EQUATION 8.

FIGURE 47 illustrates the correlation between a high Ed (EQUATION 2) and a high surface density. Cubes with a high Ed are also those with a high surface density. Samples 1 and 5 are not included in this graph due to the poor print quality. Their surface density percentages were respectively 96.33939% and 96.31625%. The samples that underwent two laser passes are highlighted in red and have a better density than the sample with the same printing parameters but with one laser pass.

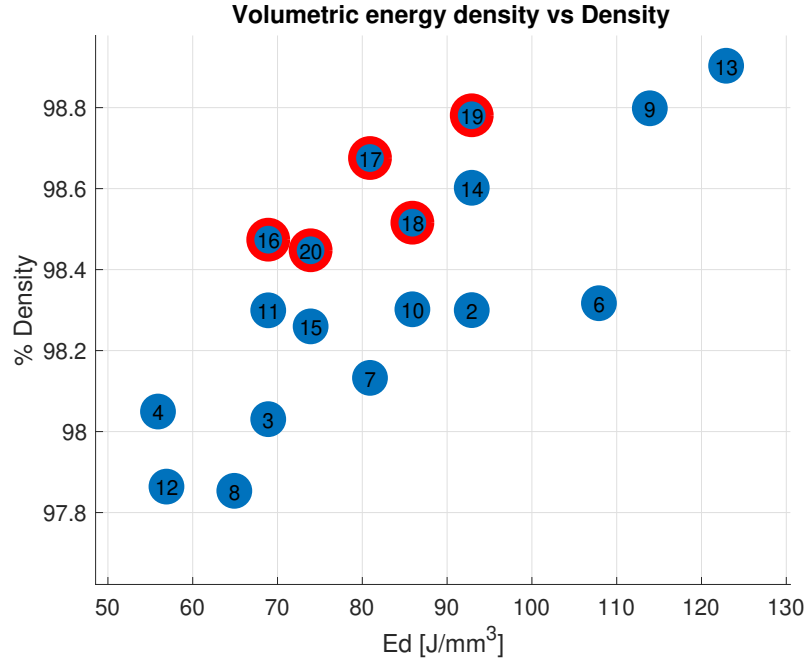


Figure 47: Graphical correlation between Ed values and percentages of density.

#### 4.3.2.2 Surface characterisation

The surface quality of all samples was assessed using a profilometer.

Surface quality also depends on Ed (EQUATION 2). For samples with low Ed, the surfaces have many peaks and valleys, while samples with high Ed exhibit the presence of spatter and poor surface quality. FIGURE 48 illustrates this correlation.

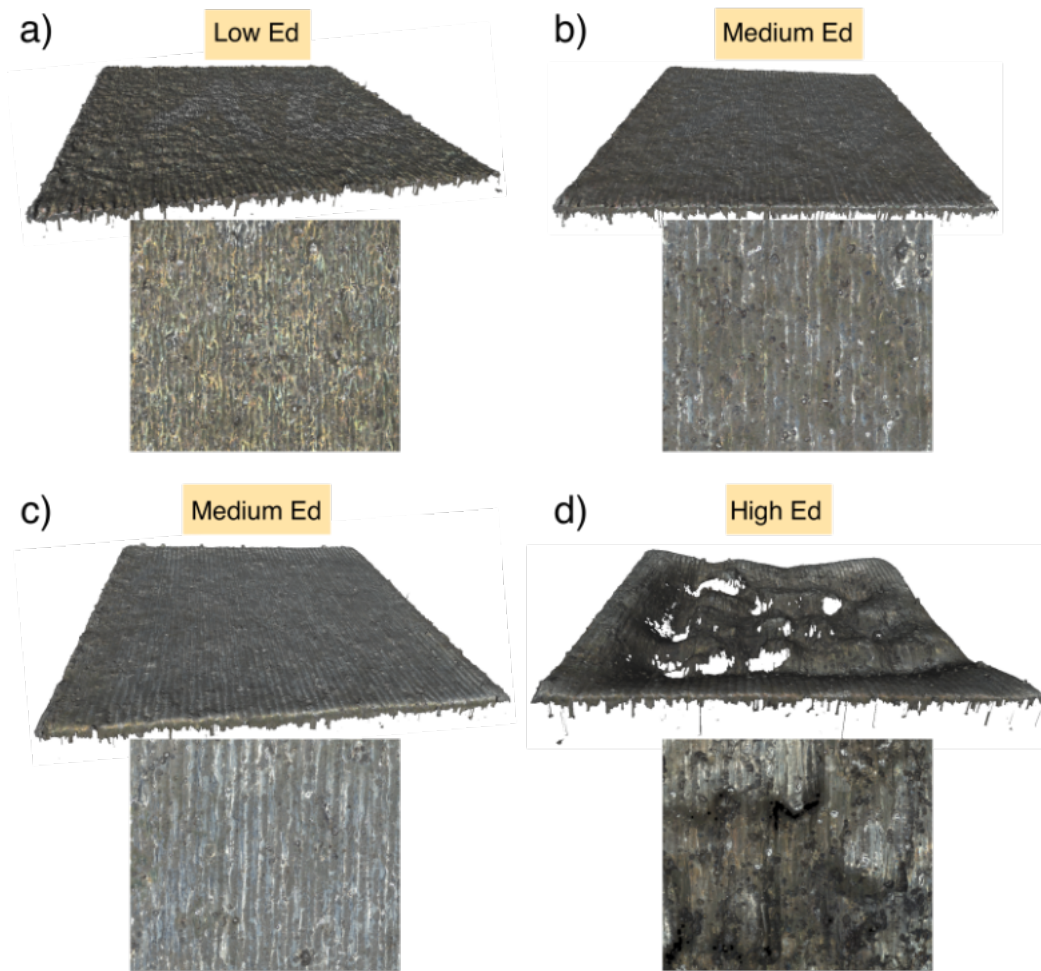


Figure 48: Surface roughness of the samples  $Al_{0.2}Cr_{0.68}Fe_{1.79}MnMo_{0.1}Ni_{1.47}$  for difference Ed. (a) Low Ed:  $57 J/mm^3$ , (b) Medium Ed:  $86 J/mm^3$ , (c) Medium Ed:  $114 J/mm^3$ , (d) High Ed:  $162 J/mm^3$ .

The surface quality is not directly correlated to the average roughness of the profile ( $R_a$ ), which remains quite constant with Ed. Nevertheless, there is a tendency for mean spacing of profile irregularities of roughness profile ( $R_{sm}$ ) to slightly elevate when Ed is high. This correlation is visually depicted in FIGURE 49.



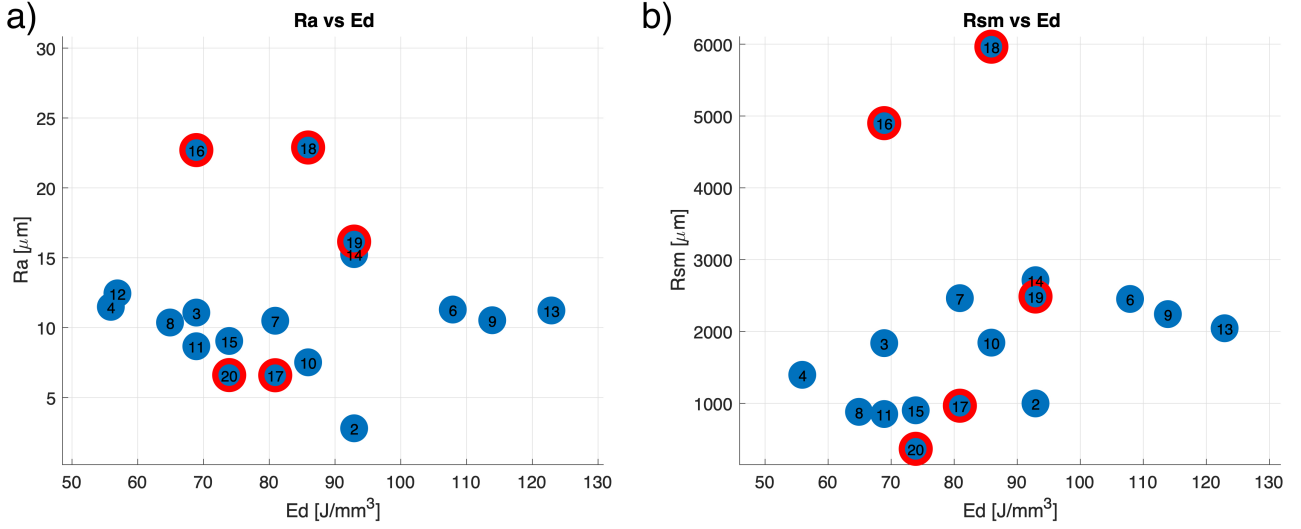


Figure 49: Correlation between quality surface and energy density (Ed). (a) Average roughness of profile plotted in relation to Ed, (b) Mean spacing of profile irregularities of roughness profile plotted in relation to Ed.

About the effect of the second laser pass, wider valleys are observed for samples that have undergone two laser passes, as shown in FIGURE 50.

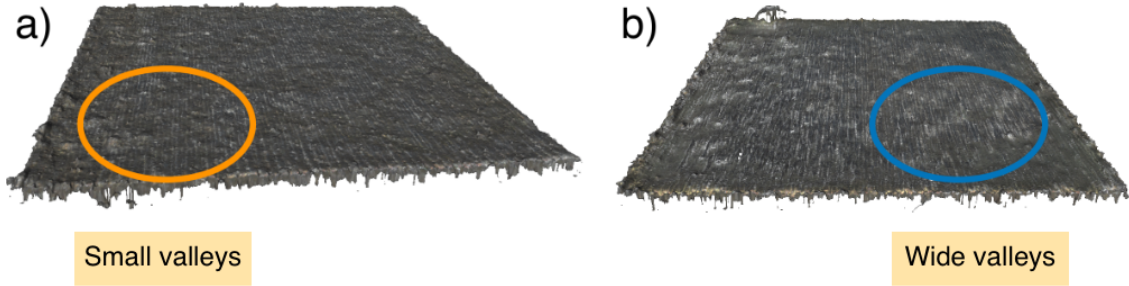


Figure 50: Surface roughness of the samples  $Al_{0.2}Cr_{0.68}Fe_{1.79}MnMo_{0.1}Ni_{1.47}$  for different laser passes (a) One laser pass, (b) Two laser passes.

#### 4.4 Hardness analysis

Hardness tests were conducted using a Vickers hardness tester (SECTION 3.7). These tests were exclusively performed on the DTA samples to gain further insights in the effects of elements and phases present in the samples.

The comparative results of hardness across the samples are shown in TABLE 22.

Table 22: Hardness of the DTA sample.

Sample	Hardness[MPa]
$Al_{0.1}Cr_2Fe_{3.4}Mn_1Mo_{0.2}Ni_{3.2}$	$505.67 \pm 28.87$
$CrFeMnNi$	$752.75 \pm 73.05$
$Cr_2Fe_2MnNi$	$666.20 \pm 65.98$
$CrFe_2MnNi_2$	$448.33 \pm 65.24$
$CrFe_2MnMo_{0.3}Ni_2$	$417.75 \pm 34.82$
$AlCrFeMnNi$	$1044.33 \pm 44.00$
$AlCrFe_2MnNi_2$	$756.00 \pm 55.57$
$AlCrFe_2Ni_2$	$752.33 \pm 48.56$
$AlCrFe_2MnMo_{0.3}Ni_2$	$1293.00 \pm 42.32$
$AlCrFe_2Mo_{0.3}Ni_2$	$1118.33 \pm 127.02$

The hardness of the samples correlates with the phases present in each sample. As illustrated in FIGURE 22, the FCC phase exhibits low hardness, the addition of the BCC phase increases hardness and the samples with an additional sigma phase display the highest hardness.

## 5 Discussion

In this chapter, the results obtained through the analyses of equilibrium and out of equilibrium solidified samples will be discussed, as well as the implications of these findings. The influence of the elements and the reliability of the phase prediction theory are discussed, as well as the importance of powder rheology and printing parameters on the quality of the printed cubes.

### 5.1 Near equilibrium solidification

The samples that are the subject of this section were produced using the DTA technique. The slow cooling rate (5 °C /min) ensures that the solidification process occurs under near equilibrium conditions.

#### 5.1.1 Influence of elements

Modifications to the composition impact the current phases or the solidification pathway. The solidification of a liquid is characterised by exothermic transitions and transformations. It can be observed that exothermic transformations are discernible during DTA, with the resultant curve exhibiting peaks. Indeed, these exothermic peaks in the DTA cooling curves, as shown in FIGURE 29, 31, 34 and 38, correspond to the energy released during the solidification of the liquid phase. The compositions exhibit a degree of variability that depends on the elements present and their respective quantities. This research examines the influence of Mo, Mn and Al on the samples. Some samples were prepared in two forms: with and without one of the elements in question (TABLE 9). The effect of Cr will also be discussed.

Mo has been demonstrated to facilitate the formation of sigma phases when incorporated in HEAs [104]. The findings of this study are consistent with those reported in the existing literature. Indeed, the addition of Mo leads to the formation of an additional phase. The presence of an IM is visible in  $CrFe_2MnMo_{0.3}Ni_2$  sample (FIGURE 30a), and the sigma phase is visible in  $AlCrFe_2MnMo_{0.3}Ni_2$  and  $AlCrFe_2Mo_{0.3}Ni_2$  samples (FIGURE 39). On the DTA curve, an additional peak is visible, corresponding to the exothermic formation of the IM or of the sigma phase. Moreover, the addition of Mo lowers the solidification temperature, as shown in FIGURE 51. The observed decrease in temperature is attributed to a change in the crystalline structure that has occurred because the addition of molybdenum [105].

In sample  $CrFe_2MnMo_{0.3}Ni_2$ , Mo and Cr segregates at the edge of the grain, to give rise to an intermetallic phase at this boundary [106]. These two elements promote the sigma phase. The formation of the sigma phase is more prevalent in alloys containing at least 20% (wt) of Cr. And the percentage in question is observed to decrease when Mo is present in the alloy [107]. A fixed Mo quantity cannot be determined, since the sigma phase depends not only on these two elements but also on many others, as shown by the ECC parameter (EQUATION 7). Nevertheless, an approximation of this percentage can be derived from observations made on HEAs that have already been studied. A threshold is observed in 27 alloys containing Cr and Mo, as included in a review article [71], which predicts the presence of the sigma phase. The threshold is found to be at 0.07 atm Mo. It should be noted that this value is not absolute and that there is already one exception in the list. The same can be said of this study. A partial of only 5% atm of Mo is sufficient to have the presence of the sigma phase, but does not guarantee it, as the  $CrFe_2MnMo_{0.3}Ni_2$  sample shows (TABLE 13 and 21). As will be discussed in SECTION 5.1.2, parameters other than the percentage of elements

favouring a phase are used to determine which phases are present.

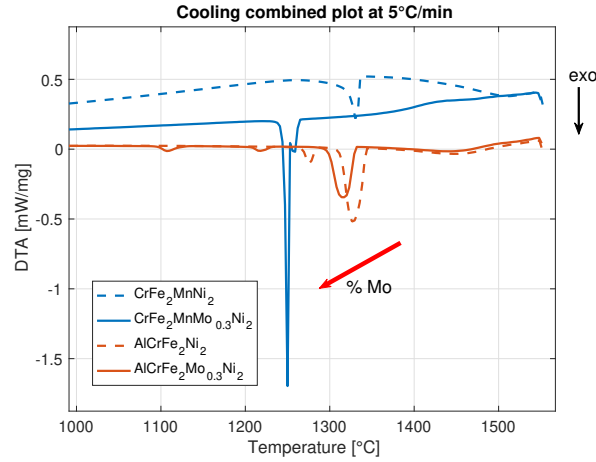


Figure 51: DTA cooling combined plots of temperature of eutectoid transformation with effect of Mo.

The addition of Mn also lowers the solidification temperature of the samples, as shown in FIGURE 52. Nevertheless, the impact on the microstructure, phase composition and solidification path appear to be relatively minor. As illustrated in TABLES 18 and 21, the proportions of the chemical composition of the phases are comparable, irrespective of the presence or absence of Mn. The addition of Mn to alloys does not generally influence the phases present as Mn tends to dissolve in the existing phases without significantly altering the overall phase structure. This behaviour is reinforced by the relative compatibility of Mn with the elements in a Cr-Fe-Ni system, thus satisfying the Hume-Rothery rules, which state that differences in atomic size, crystalline structure, valence electron concentration and electronegativity must be minimal to form continuous solid solutions [108]. In addition, Mn often acts as a solid solution strengthener rather than forming new intermetallic compounds. [109]. This feature is evident in HEAs, where phase stability is mainly governed by high configurational entropy, and Mn contributes to solid solution strengthening without inducing phase transformations [110].

The addition of Al does not have a systematic effect on a change of temperature at the start of solidification. However, it is well established that Al is a precursor of the BCC phase [89]. In  $CrFe_2MnNi_2$  and  $CrFe_2MnMo_{0.3}Ni_2$  samples that do not have a BCC phase, the addition of Al results in the formation of this phase. A peak associated with this new transformation is also observed on the DTA curves, as shown in FIGURE 34 and 38. The addition of Al tends to stabilise the BCC phase in comparison to the FCC phase. This behaviour is due to the difference in atomic size and the electronic structure of Al, which modifies the free energy, favouring the formation of the BCC phase. The average radius of Al is 13.5% greater than that of the Cr, Fe, Ni and Mn used in this study. The size difference results in a deformation of the crystal lattice, which stabilises the BCC phase in comparison to the FCC phase [111].



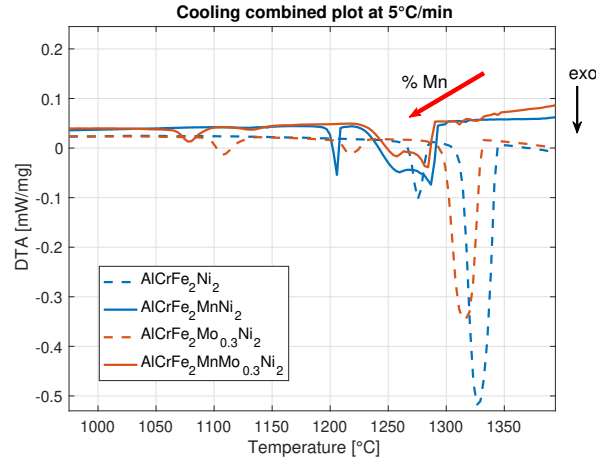


Figure 52: DTA cooling combined plots of temperature of eutectoid transformation with effect of Mn.

Moreover, the addition of Al leads to a solid-state transformation as demonstrated by the presence of cuboid and rod-shaped precipitates in the *AlCrFeMnNi* sample (FIGURE 35c and d). These precipitates are known to form through a spinodal decomposition [112]. Spinodal decomposition is also present in the *AlCrFe<sub>2</sub>MnNi<sub>2</sub>* sample, because of the addition of Al. Spinodal decomposition leads to the formation of an ordered phase (BCC/B2) and a disordered phase (BCC). The terms "ordered" and "disordered" refer to the arrangement of the atoms. The ordered B2 phase is characterised by a specific, regular atomic structure, in which the atoms are arranged in a defined pattern. In contrast, the disordered BCC phase lacks a specific long-range atomic arrangement, resulting in a more random distribution of atoms [113]. Because the spinodal decomposition is an entropy-reducing process and temperature can increase the entropy contribution, the occurrence of this decomposition is less frequent at elevated temperatures. Nevertheless, it is possible that spinodal decomposition may occur at 1200°C, particularly if the sample contains a significant number of elements. Spinodal decomposition is observed in approximately 30% of five-element alloys at 1200°C [114]. The exothermic peaks observed in the DTA cooling curves are typically of a lower intensity in the case of solid-state transformations than in the case of liquid-to-solid transformations (FIGURE 38). Solid-state transformations involve rearrangements of atoms within the solid phase [115]. This generally requires less energy than the initial solidification process, which releases a significant amount of latent heat because the material goes from a high-energy liquid state to a low-energy solid state [116].

### 5.1.2 Phase prediction theories

As explained in SECTION 2.2.5, different parameters are used to predict the phases present in the microstructures of HEAs. Specifically, the VEC is a significant parameter in determining phase structures such as FCC and BCC, while ECC is a significant parameter only in determining sigma phase.

#### 5.1.2.1 FCC and BCC phases

Given that the FCC phase is more corrosion-resistant than the BCC phase [81], the ability to identify a parameter that can predict the presence of a specific phase in a given sample is a valuable tool in the investigation of the composition of a corrosion-resistant alloy. It is established that a higher VEC corresponds to high atomic bonding forces, inducing atoms to

rearrange in the FCC structure with greater packing density. A low VEC results in low atomic bonding forces, causing atoms to preferentially form the BCC structure characterised by lower atomic packing density [117]. By knowing the VEC of each element (TABLE 3) and their respective composition in the powder mixture (TABLE 9), the VEC of each sample was calculated with EQUATION 6. As previously outlined in SECTION 2.2.5, the VEC theory posits two threshold values that can be employed to identify the presence of the FCC and / or BCC phases in a given sample. The value of the VEC and the observed phases in each sample are presented in TABLE 23. As illustrated in this table, the present study includes samples with VECs in these three categories.

Of the ten samples that were subjected to analysis, seven had the phases predicted by the theory. So, there are three inaccuracies in the predictions from the analysis observed. For the  $AlCrFe_2MnMo_{0.3}Ni_2$  and  $AlCrFe_2Mo_{0.3}Ni_2$  samples, the sigma phase is present while the VEC theory only predicts the BCC and FCC phases. And for the  $AlCrFeMnNi$  sample, it was expected that the sample was only composed of the BCC phase because the VEC of this sample is lower than 6.87.

These three samples are characterised by the presence of solid-state transformation or sigma phase. In the  $AlCrFeMnNi$  sample, the additional phases, which contradict the VEC theory, occur after solidification, at a lower temperature. Indeed, it has been demonstrated that, during the solidification of equiatomic  $AlCrFeMnNi$ , the first solid to form in dendritic and interdendritic regions is BCC. As the temperature continues to decrease, spinodal decomposition occurs, leading to precipitates formation [112]. Regarding the two samples featuring the sigma phase,  $AlCrFe_2MnMo_{0.3}Ni_2$  and  $AlCrFe_2Mo_{0.3}Ni_2$ , the sigma phase is also a solid-state transformation, which occurs at lower temperatures [118]. At the end of solidification, before these solid-state transformations occurred, the VEC theory correctly predicted the phases present. The VEC theory focuses on electronic considerations rather than kinetic or thermodynamic factors, which influence the formation of a phase [22].

The VEC theory does not consider the solid-state transformations occurring during cooling. Nonetheless, it remains a valuable tool for explaining microstructures in HEAs, particularly in predicting the phases that form during solidification. The microstructure is a significant factor in the properties of an alloy, and therefore the VEC is an essential parameter to consider when selecting the range composition of a corrosion-resistant HEA. Nevertheless, the presence of sigma phases indicates the potential validity of additional theories; these will be discussed in the subsequent section.

### 5.1.2.2 Sigma phases

The presence of the sigma phase is associated with a reduction in ductility and corrosion resistance, as well as an increase in brittleness and the formation of cracks [83]. As with the formation of the FCC and BCC phases, the identification of a predictive parameter that correlates with their formation is a useful tool in the design of all-alike structures. The prediction of the sigma phase has been attempted using different parameters, employing both the VEC [82] and the Equivalent Chrome Content (ECC) [88]. As explained in SECTION 2.2.5, the theory posits that, in HEAs containing Cr and/or V, the sigma phase forms when the VEC (EQUATION 6) falls within the range of 6.88 to 7.84. The theory based on the equivalent chromium content posits that if the ECC (EQUATION 7) is greater than

17–18%, the alloy tends to form sigma phase.

The VEC and ECC values for each sample and the phases observed are shown in TABLE 23.

Table 23: VEC and phases observed of DTA samples.

Sample	VEC	ECC	Observed phases
$Al_{0.1}Cr_2Fe_{3.4}Mn_1Mo_{0.2}Ni_{3.2}Si_{0.1}$	8.02	21%	FCC
$CrFeMnNi$	7.75	25%	BCC and FCC
$Cr_2Fe_2MnNi$	7.5	33%	BCC and FCC
$CrFe_2MnNi_2$	8.17	13%	FCC
$CrFe_2MnMo_{0.3}Ni_2$	8.06	26%	FCC
$AlCrFeMnNi$	6.8	25%	BCC and FCC
$AlCrFe_2MnNi_2$	7.48	25%	BCC and FCC
$AlCrFe_2Ni_2$	7.5	25%	BCC and FCC
$AlCrFe_2MnMo_{0.3}Ni_2$	7.37	25%	FCC, BCC and sigma
$AlCrFe_2Mo_{0.3}Ni_2$	7.47	25%	FCC, BCC and sigma

All the samples contained Cr, and six of them met the expected VEC values for the prediction of the sigma phase. However, only  $AlCrFe_2MnMo_{0.3}Ni_2$  and  $AlCrFe_2Mo_{0.3}Ni_2$  samples actually contained sigma in their microstructure.

For the ECC prediction, all the samples except  $CrFe_2MnNi_2$  have ECC values that satisfy the ECC theory. Theoretically, all of them should contain the sigma phase. However, only  $AlCrFe_2MnMo_{0.3}Ni_2$  and  $AlCrFe_2Mo_{0.3}Ni_2$  have sigma phase.

It is observed that the two samples exhibiting the sigma phase are those containing Mo. A single exception can be observed in  $Al_{0.1}Cr_2Fe_{3.4}Mn_1Mo_{0.2}Ni_{3.2}Si_{0.1}$  sample, but this sample contains IM and has a VEC > 7.84. It can be inferred that if the samples meet both theoretical criteria (VEC and ECC) and contain Mo, they will exhibit the sigma phase. This result is expected, given that, as explained in SECTION 5.1.1, the presence of the Mo element is often associated with the formation of the sigma phase [104]. It can therefore be postulated that the presence of the sigma phase can be assumed if the VEC is between 6.88 and 7.84, the ECC is grater 18% and the alloy contains elements that promotes the sigma phase. Mo is not a necessary component of the sigma phase; it can be substituted by other elements that promote sigma phase formation, such as Ti [119].

Consequently, even though phase prediction theory helps interpret and predict the phases present in HEA, it is not infallible. These values should be considered as indications rather than facts. Moreover, it is essential to consider that the VEC theory does not account for solid-state transformations that occur during cooling. These theories are unable to predict the microstructures present, such as the dendritic and interdendritic regions. Even if the phases are correctly predicted, the proportion of each phase cannot be known.

All the samples were produced by DTA, and therefore with a slow cooling rate (5°C /min), to favour equilibrium transformation. However, the way the HEA is processed is also crucial to consider; the cooling rate impacts the phases present. This can alter atomic diffusion, potentially eliminating phase transitions and intermetallic formation during the cooling process [5].

## 5.2 Out of equilibrium solidification

The samples that are the subject of this section were produced using LPBF technology. The fast cooling rate ( $10^5$  to  $10^8$  K/s) ensures that the solidification process occurs out equilibrium conditions.

### 5.2.1 Rheology of powders

The spreadability of powders in AM, such as LPBF, is significantly influenced by the shape of the particles. This study highlights how different particle morphologies (spherical and non-spherical) and a pre-heating affect the spreadability of powder mixtures. As explained in SECTION 2.1.1.2, a high degree of spreadability is crucial for a good power bed, which affects the density and surface of the piece.

The incorporation of spherical or non-spherical powder in the powder mixture has the effect of influencing the spreadability of the powder mixture. The incorporation of 316L steel powder, a spherical powder with ideal rheological properties for 3D printing, enhance the spreadability of the powder mixture (FIGURE 41), even when the powder mixture is still partially composed of non-spherical powder (FIGURE 16). Indeed, spherical powders exhibit superior spreadability due to their reduced inter-particle friction and enhanced interlocking capabilities [120]. Conversely, the addition of non-spherical powder to the powder mixture (FIGURE 40c and d) results in an even spread. Non-spherical powders have a larger contact surface between them, increasing friction and cohesion [121]. This, in turn, decreases the spreadability of the powder mixture.

Another factor that alter the spreadability of a powder mixture is the presence of pre-heating. Improved spreadability has been observed after heating the powder mixture to 200 °C (FIGURE 41). The presence of moisture in our powders may have affected its spreadability. Preheating dried the powders, improving their spreadability [122].

### 5.2.2 Solidification

The printing parameters are importance achieve a piece with a high density, a smooth outer surface, and minimal cracking and porosity (SECTION 2.1.1.3). During the study, printing parameters that would result in the lowest defect rates were identified. This study tested 53 pairs of different laser power and scanning speed combinations (ANNEX B), and the effect of the number of laser passes (TABLE 11). Therefore, four parameters, namely laser power, scanning speed, energy density (both volumetric and linear) and the number of laser passes were investigated.

A pre-selection of parameters (laser power, scanning speed, and linear energy density) was conducted through a single track (SECTION 4.3.1), to establishing a correlation between the defects; i.e. spatter, discontinuity, or irregular track (FIGURE 42) and the parameters.

Low laser power has been associated to the formation of tracks that do not fully melt and those that exhibit irregularities in their track (FIGURE 42a). The energy delivered to the track was insufficient to achieve complete melting of the powder [123]. Consequently, the melt pool does not persist long enough for the track to propagate [124]. The volume of the molten

pool is therefore comparatively limited, resulting in a thinner width (FIGURE 43) [125]. Conversely, a high scanning speed and high power input can result in the formation of spatter defects FIGURE 42b. The excessive energy input in these tracks results in instability and spatter formation [125]. In the presence of spatter, the powder layer that is to be overlaid does not spread evenly. A combination of parameters to achieve average energy (between 0.2 and 0.5 J/mm), high power (>140 W) and moderate speed (between 600 and 1200mm/s) resulted in tracks with the fewest defects (FIGURE 44). For these tracks, the energy input enabled the melt pool to melt and to be continuous [125].

Based on the analysis of each defect in every track, FIGURE 53 was generated, outlining the ideal parameters and indicating which parameters tend to create specific defects.

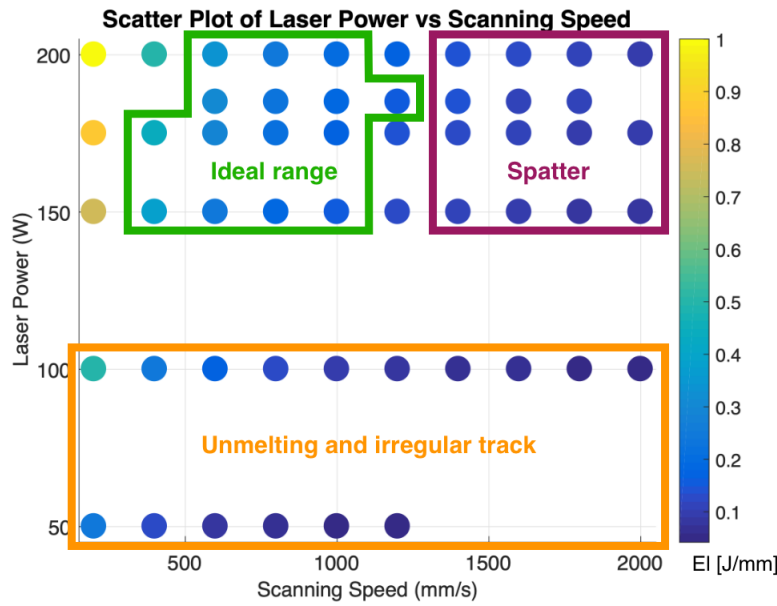


Figure 53: Process map with regards to the single track  $AlCrFe_2MnNi_2$ .

The parameters highlighted in green were employed during the printing of the cubes with the objective of evaluating the surface area and density of the samples produced (TABLE 11). The fixed printing parameters are defined in SECTION 3.3.2.2. Three varying parameters were the laser power, the scanning speed, and the number of laser passes. The 20 samples were compared based on their density and surface appearance.

The results indicate that samples printed with an excessively low scanning speed (400mm/s) and high  $Ed$ , namely samples 1 and 5, could not be printed effectively (FIGURE 45). This defect increased with each layer of printing (FIGURE 46), meaning that their surface area at the end of printing (FIGURE 48d), as well as their density (FIGURE 47), were not optimised.

In addition, samples with a high scanning speed, i.e. over 1000 mm/s, printed correctly but had the lowest density results. The high scanning speed of the samples resulted in a low energy density ( $Ed$ ), which prevented the input of sufficient energy for complete powder fusion and the formation of a sufficiently large melt pool. Indeed, the melting capacity of the powder decreases with low energy input [123]. Furthermore, samples with a low  $Ed$  also exhibit reduced surface quality (FIGURE 48 and 50), because of the insufficient energy input leading to inadequate remelting. The reduction in roughness is attributed to the reduced

reabsorption of unmelted particles [126]

With an average energy (between 77 and 111 J/mm<sup>3</sup>), no remarkable problems were identified about the quality of the surface of the parts and the density. At this step, FIGURE 54, considering the occurrence of defects, has been drawn, based on the above considerations obtained from the microscopic and macroscopic characterisation of the samples. This figure is attributed to a process map that gives an idea of the optimised parameters used to achieve fully printed LPBF HEA parts with high density and optimum surface.

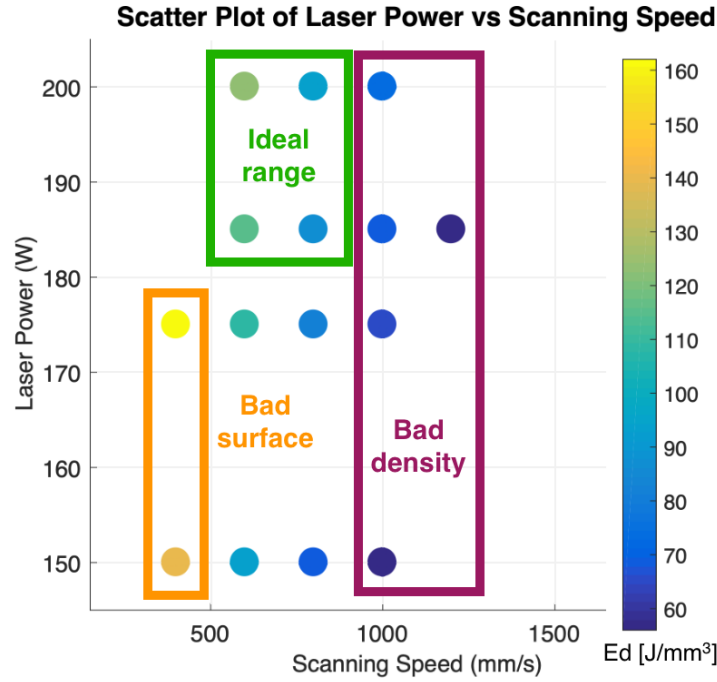


Figure 54: Process map with regards to the printing of  $Al_{0.2}Cr_{0.68}Fe_{1.79}MnMo_{0.1}Ni_{1.47}$  alloy.

As explained in SECTION 3.3.2.2, five samples have a double laser pass (samples 16 to 20 in TABLE 11). As the powder mixture is composed of mainly elemental powders with different rheological properties and morphology, a double laser pass increases homogeneity [127]. Further research is required to determine the impact of double laser on the microstructure and homogeneity. However, the effect of the double laser pass, there is an improvement of the density, ranging from 0.19 to 0.54% (FIGURE 47), but the surface is less smooth (FIGURE 50). At this stage, the double pass is not relevant because it considerably increases the printing time and energy. However, if the double laser considerably improves the homogeneity of samples, it would be interesting to test other Ed values for the second pass, to keep a less roughness surface.

### 5.3 Hardness analysis

As mentioned in SECTION 2.2.4.2, the hardness of an alloy is contingent upon the phases present. In this study, samples with a single FCC phase, a mixture of FCC and BCC phases and a mixture of FCC, BCC and sigma phases were subjected to an investigation and subjected to hardness testing (TABLE 22). The FCC phase exhibits a low hardness, in contrast to the BCC [71] and sigma phases [104]. This difference is due to their crystalline structure. The FCC phase has more

slip systems than the BCC phase, which makes it easier for dislocations to move. As a result the FCC phase is less hard than the BCC phase [128]. The hardness values of the samples are consistent with the expected range. In this study, the hardness values for samples that exhibit only FCC phase range from 417 to 505 MPa. The presence of the BCC phase in the samples has been found to significantly enhance the hardness of the samples in question. The hardness of the samples is between 666 and 1040 MPa. Finally, the presence of the sigma phase, also increases hardness, reaching 1118 to 1293 MPa. However, the hardness of the samples does not correlate with their proportion of FCC or BCC phase. The  $CrFeMnNi$  sample contains less BCC phase than the  $Cr_2Fe_2MnNi$  sample (TABLE 16), yet the measured hardness is higher. A similar observation is made with the  $AlCrFe_2MnNi_2$  sample, which contains a greater proportion of BCC phase than the  $AlCrFe_2Ni_2$  sample (TABLE 19). However, despite this difference in phase composition, the hardness of the two samples is comparable. Contrary to theoretical expectations [71], no correlation was observed between hardness and the quantification of BCC and FCC phases. Hypotheses were put forward to explain this difference. The small size of the indenter used could limit its interaction to a single phase during the test, thus underestimating the impact of the different phases on the hardness measured. In addition, the limited number of hardness tests carried out on each sample, generally between 3 and 5 due to their size, may not proportionally represent all the phases present, thus influencing the variation in hardness measured.

## 5.4 Limitations

Some limitations were encountered during the realisation of this master thesis. It is essential to highlight them and analyse them to improve the results obtained.

The LPBF process requires certain powder characteristics, such as spherical morphology and sizes between 30 and  $50\mu m$ . Unfortunately, given the preliminary nature of this research, there has been a restriction on the powders. They were available in small quantities and with non-spherical morphologies, not suitable for LPBF. In fact, these powders were intended to produce DTA samples, a system in which the rheology of powders contributes little. As explained in the previous section, the quality of the powders is a crucial parameter for the quality of the printed parts, and some of the defects observed on the printed parts might not occur if the powders were spherical. The solution found to achieve sufficient spreadability was to add more 316L steel powder in powder mixture, this had the consequence of changing the composition compared to the desired alloy. Moreover, 316L steel powder does not only contain the six elements desired for HEA, it also added six other unwanted elements in very small amount : Si, C, O, N, P and S (less than 0.67% wt, ANNEX A).

## 6 Future perspectives

- The analyses of the printed cubes should continue on their microstructures to see if the VEC theory is also functional for samples made from LPBF, and analyse the quality of the printed parts in greater depth (internal porosity, crack, homogeneity of elements, etc.).  
Microstructure analyses can also reveal the impact and/or need for a double laser pass on homogeneity.
- The analyses of the printed cubes should also focus on their mechanical properties to see if the sample is corrosion resistant and test other properties, to find applications for this alloy.
- Perform DTA sample with the printed composition to study the differences due to rapid or slow cooling rates.
- The selected composition should be reprinted using powders with optimal morphologies for 3D printing, specifically spherical particles with a diameter between 30 and 45  $\mu\text{m}$ .



## 7 Conclusion

- DTA curves can help to understand the solidification path. The transformation temperatures of the alloy can be identified by the exothermic or endothermic peak visible on the curves. Additionally, the number of transformations (liquid to solid or solid to solid) observed during solidification can be quantified.
- DTA is a fast and inexpensive way of preliminarily analysing HEA compositions. The powders used for this process do not need to have a particular morphology, and only a few are required. The present phases are easily observed by OM and SEM, and identifiable by EBSD. Tests on their mechanical properties such as hardness can easily be carried out. Therefore, the price and time to analyse a HEA made by DTA are lower.
- The theories, which can predict which phases will be present in a sample, has been used and confirmed. However, it does not consider solid-state transformations. The integration of multiple theories enables the prediction of the presence of the sigma phase.
- The morphology of the powders are essential for the spreadability. Pre-heating and spherical powders increase the spreadability of the powder mixture.
- The parameter  $E_d$ , which depends on the main printing parameters, is a crucial factor in determining the quality of printed samples. A process map can be generated on the basis of  $E_d$ . This provides a rapid overview of the defects associated with the various parameters, as well as the parameters that yielded the most optimal quality piece. In the context of  $Al_{0.2}Cr_{0.68}Fe_{1.79}MnMo_{0.1}Ni_{1.47}$  printing, the ideal value of  $E_d$  are between 77 and 111 J/mm<sup>3</sup>, with a scanning speed between 600 and 800 mm/s, and a laser power between 185 and 200 W. Low  $E_d$  (<70 J/mm<sup>3</sup>) results in poor quality samples in the density, while high  $E_d$  (>135 J/mm<sup>3</sup>) makes the low quality surface, also resulting in poor density.

## References

- [1] MERTENS Anne. Meca0139-1 - additive manufacturing and 3d printing. *Faculty of Applied Sciences (ULiège)*, 2021.
- [2] AmirMahyar Khorasani, Ian Gibson, Jithin Kozhuthala Veetil, and Amir Hossein Ghasemi. A review of technological improvements in laser-based powder bed fusion of metal printers. *The International Journal of Advanced Manufacturing Technology*, 108:191–209, 2020.
- [3] YEH Jien-Wei. Recent progress in high entropy alloys. *Ann. Chim. Sci. Mat*, 31(6):633–648, 2006.
- [4] Zia Ullah Arif, Muhammad Yasir Khalid, Ehtsham ur Rehman, Sibghat Ullah, Muhammad Atif, and Ali Tariq. A review on laser cladding of high-entropy alloys, their recent trends and potential applications. *Journal of Manufacturing Processes*, 68:225–273, 2021.
- [5] Ahmad Ostovari Moghaddam, Nataliya A Shaburova, Marina N Samodurova, Amin Abdollahzadeh, and Evgeny A Trofimov. Additive manufacturing of high entropy alloys: A practical review. *Journal of Materials Science & Technology*, 77:131–162, 2021.
- [6] John J Lewandowski and Mohsen Seifi. Metal additive manufacturing: a review of mechanical properties. *Annual review of materials research*, 46:151–186, 2016.
- [7] Walaa Abd-Elaziem, Sally Elkatatny, Abd-Elrahim Abd-Elaziem, Mahmoud Khedr, Marwa A. Abd El-baky, Mohamed Ali Hassan, Mohamed Abu-Okail, Moustafa Mohammed, Antti Järvenpää, Tarek Allam, and Atef Hamada. On the current research progress of metallic materials fabricated by laser powder bed fusion process: a review. *Journal of Materials Research and Technology*, 20:681–707, 2022.
- [8] Manu Srivastava, Sandeep Rathee, Vivek Patel, Atul Kumar, and Praveennath G. Koppad. A review of various materials for additive manufacturing: Recent trends and processing issues. *Journal of Materials Research and Technology*, 21:2612–2641, 2022.
- [9] Minh-Son Pham, Bogdan Dovggy, Paul A Hooper, Christopher M Gourlay, and Alessandro Piglione. The role of side-branching in microstructure development in laser powder-bed fusion. *Nature communications*, 11(1):749, 2020.
- [10] Yu Dong, Jamie Milentis, and Alokesh Pramanik. Additive manufacturing of mechanical testing samples based on virgin poly (lactic acid)(pla) and pla/wood fibre composites. *Advances in Manufacturing*, 6:71–82, 2018.
- [11] Manu Srivastava and Sandeep Rathee. Additive manufacturing: Recent trends, applications and future outlooks. *Progress in Additive Manufacturing*, 7(2):261–287, 2022.
- [12] Yihong Kok, Xi Peng Tan, Pan Wang, MLS Nai, Ngiaap Hiang Loh, Erjia Liu, and Shu Beng Tor. Anisotropy and heterogeneity of microstructure and mechanical properties in metal additive manufacturing: A critical review. *Materials & Design*, 139:565–586, 2018.
- [13] Ming-Wei Wu, Pang-Hsin Lai, and Jhewn-Kuang Chen. Anisotropy in the impact toughness of selective laser melted ti-6al-4v alloy. *Materials Science and Engineering: A*, 650:295–299, 2016.

- [14] Anketa Jandyal, Ikshita Chaturvedi, Ishika Wazir, Ankush Raina, and Mir Irfan Ul Haq. 3d printing—a review of processes, materials and applications in industry 4.0. *Sustainable Operations and Computers*, 3:33–42, 2022.
- [15] Rajat Kawalkar, Harrsh Kumar Dubey, and Satish P. Lokhande. A review for advancements in standardization for additive manufacturing. *Materials Today: Proceedings*, 50:1983–1990, 2022. 2nd International Conference on Functional Material, Manufacturing and Performances (ICFMMP-2021).
- [16] Ana Vafadar, Ferdinando Guzzomi, Alexander Rassau, and Kevin Hayward. Advances in metal additive manufacturing: a review of common processes, industrial applications, and current challenges. *Applied Sciences*, 11(3):1213, 2021.
- [17] Tim Marten Wischeropp, Hussein Tarhini, and Claus Emmelmann. Influence of laser beam profile on the selective laser melting process of alsil0mg. *Journal of laser applications*, 32(2), 2020.
- [18] Lai-Chang Zhang and Hooyar Attar. Selective laser melting of titanium alloys and titanium matrix composites for biomedical applications: A review. *Advanced Engineering Materials*, 18(4):463–475, 2016.
- [19] Ian Gibson, David Rosen, Brent Stucker, Mahyar Khorasani, Ian Gibson, David Rosen, Brent Stucker, and Mahyar Khorasani. Introduction and basic principles. *Additive manufacturing technologies*, pages 1–21, 2021.
- [20] L.C. Zhang, D. Klemm, J. Eckert, Y.L. Hao, and T.B. Sercombe. Manufacture by selective laser melting and mechanical behavior of a biomedical ti–24nb–4zr–8sn alloy. *Scripta Materialia*, 65(1):21–24, 2011.
- [21] Sohini Chowdhury, N. Yadaiah, Chander Prakash, Seeram Ramakrishna, Saurav Dixit, Lovi Raj Gupta, and Dharam Buddhi. Laser powder bed fusion: a state-of-the-art review of the technology, materials, properties & defects, and numerical modelling. *Journal of Materials Research and Technology*, 20:2109–2172, 2022.
- [22] B. Gorny, T. Niendorf, J. Lackmann, M. Thoene, T. Troester, and H.J. Maier. In situ characterization of the deformation and failure behavior of non-stochastic porous structures processed by selective laser melting. *Materials Science and Engineering: A*, 528(27):7962–7967, 2011.
- [23] Yu Wang, Jens Bergström, and Christer Burman. Characterization of an iron-based laser sintered material. *Journal of Materials Processing Technology*, 172(1):77–87, 2006.
- [24] Lore Thijs, Frederik Verhaeghe, Tom Craeghs, Jan Van Humbeeck, and Jean-Pierre Kruth. A study of the microstructural evolution during selective laser melting of ti–6al–4v. *Acta Materialia*, 58(9):3303–3312, 2010.
- [25] Bi Zhang, Yongtao Li, and Qian Bai. Defect formation mechanisms in selective laser melting: a review. *Chinese Journal of Mechanical Engineering*, 30:515–527, 2017.
- [26] Jinge Liu and Peng Wen. Metal vaporization and its influence during laser powder bed fusion process. *Materials & Design*, 215:110505, 2022.

- [27] Jee-Eun Jang, Woosung Kim, Ji-Hyun Sung, Young-Joo Kim, Sung-Hyuk Park, and Da-Hye Kim. Microstructural control strategy based on optimizing laser powder bed fusion for different hastelloy x powder size. *Materials*, 15(18):6191, 2022.
- [28] Muhammad Arif Mahmood, Diana Chioibas, Asif Ur Rehman, Sabin Mihai, and Andrei C Popescu. Post-processing techniques to enhance the quality of metallic parts produced by additive manufacturing. *Metals*, 12(1):77, 2022.
- [29] TV Rajan, CP Sharma, and Ashok Sharma. Chapter 1 - introduction. In *Heat treatment: principles and techniques*. PHI Learning Pvt. Ltd., 2023.
- [30] Majid Laleh, Esmaeil Sadeghi, Reynier I Revilla, Qi Chao, Nima Haghdadi, Anthony E Hughes, Wei Xu, Iris De Graeve, Ma Qian, Ian Gibson, et al. Heat treatment for metal additive manufacturing. *Progress in Materials Science*, 133:101051, 2023.
- [31] E Ukar, A Lamikiz, F Liébana, S Martínez, and I Tabernero. An industrial approach of laser polishing with different laser sources. *Materialwissenschaft und Werkstofftechnik*, 46(7):661–667, 2015.
- [32] Yuchao Bai, Akshay Chaudhari, and Hao Wang. Investigation on the microstructure and machinability of astm a131 steel manufactured by directed energy deposition. *Journal of Materials Processing Technology*, 276:116410, 2020.
- [33] H.J Niu and I.T.H Chang. Selective laser sintering of gas and water atomized high speed steel powders. *Scripta Materialia*, 41(1):25–30, 1999.
- [34] Andre Mussatto, Robert Groarke, Aidan O’Neill, Muhannad Ahmed Obeidi, Yan Delaure, and Dermot Brabazon. Influences of powder morphology and spreading parameters on the powder bed topography uniformity in powder bed fusion metal additive manufacturing. *Additive Manufacturing*, 38:101807, 2021.
- [35] Tatiana Fedina, Jesper Sundqvist, and Alexander FH Kaplan. The role of powder morphology in particle movement behavior in laser powder bed fusion with an emphasis on fluid drag. *Powder Technology*, 395:720–731, 2022.
- [36] Leo VM Antony and Ramana G Reddy. Processes for production of high-purity metal powders. *Jom*, 55:14–18, 2003.
- [37] Bochuan Liu, Ricky Wildman, Christopher Tuck, Ian Ashcroft, and Richard Hague. Investigation the effect of particle size distribution on processing parameters optimisation in selective laser melting process. *22nd Annual International Solid Freeform Fabrication Symposium - An Additive Manufacturing Conference, SFF 2011*, 01 2011.
- [38] Sunpreet Singh, Seeram Ramakrishna, and Roopkaran Singh. Material issues in additive manufacturing: A review. *Journal of Manufacturing Processes*, 25:185–200, 01 2017.
- [39] Gopal S Upadhyaya. Chapter 2 - metal powder production. In *Powder metallurgy technology*. Cambridge Int Science Publishing, 1997.
- [40] Tarasankar DebRoy, Huiliang L Wei, James S Zuback, Tuhin Mukherjee, John W Elmer, John O Milewski, Allison Michelle Beese, A de Wilson-Heid, Amitava De, and Wei Zhang. Additive manufacturing of metallic components—process, structure and properties. *Progress in Materials Science*, 92:112–224, 2018.

- [41] Anton Du Plessis, Ina Yadroitsava, and Igor Yadroitsev. Effects of defects on mechanical properties in metal additive manufacturing: A review focusing on x-ray tomography insights. *Materials & Design*, 187:108385, 2020.
- [42] K Wissenbach D D Gu, W Meiners and R Poprawe. Laser additive manufacturing of metallic components: materials, processes and mechanisms. *International Materials Reviews*, 57(3):133–164, 2012.
- [43] Snehashis Pal, Nenad Gubelj, Radovan Hudák, Gorazd Lojen, Viktória Rajtúková, Tomaz Brajlili, and Igor Drstvenšek. Evolution of the metallurgical properties of ti-6al-4v, produced with different laser processing parameters, at constant energy density in selective laser melting. *Results in Physics*, 17:103186, 2020.
- [44] Donghua Dai and Dongdong Gu. Thermal behavior and densification mechanism during selective laser melting of copper matrix composites: Simulation and experiments. *Materials & Design*, 55:482–491, 2014.
- [45] Noriko Read, Wei Wang, Khamis Essa, and Moataz M Attallah. Selective laser melting of alsil0mg alloy: Process optimisation and mechanical properties development. *Materials & Design (1980-2015)*, 65:417–424, 2015.
- [46] Majid Laleh, Anthony E Hughes, Sam Yang, Jianli Li, Wei Xu, Ian Gibson, and Mike Y Tan. Two and three-dimensional characterisation of localised corrosion affected by lack-of-fusion pores in 316l stainless steel produced by selective laser melting. *Corrosion Science*, 165:108394, 2020.
- [47] Shubhavardhan Ramadurga Narasimharaju, Wenhan Zeng, Tian Long See, Zicheng Zhu, Paul Scott, Xiangqian Jiang, and Shan Lou. A comprehensive review on laser powder bed fusion of steels: Processing, microstructure, defects and control methods, mechanical properties, current challenges and future trends. *Journal of Manufacturing Processes*, 75:375–414, 2022.
- [48] Chuanbin Du, Yanhua Zhao, Jingchao Jiang, Qian Wang, Haijin Wang, Nan Li, and Jie Sun. Pore defects in laser powder bed fusion: Formation mechanism, control method, and perspectives. *Journal of Alloys and Compounds*, 944:169215, 2023.
- [49] P Karimi, Tahira Raza, Joel Andersson, and L-E Svensson. Influence of laser exposure time and point distance on 75- $\mu$ m-thick layer of selective laser melted alloy 718. *The International Journal of Advanced Manufacturing Technology*, 94:2199–2207, 2018.
- [50] Wenjia Wang, Jinqiang Ning, and Steven Y Liang. Analytical prediction of balling, lack-of-fusion and keyholing thresholds in powder bed fusion. *Applied Sciences*, 11(24):12053, 2021.
- [51] M Shiomi, K Osakada, K Nakamura, T Yamashita, and F Abe. Residual stress within metallic model made by selective laser melting process. *CIRP annals*, 53(1):195–198, 2004.
- [52] Dongdong Gu and Yifu Shen. Balling phenomena in direct laser sintering of stainless steel powder: Metallurgical mechanisms and control methods. *Materials & Design*, 30(8):2903–2910, 2009.

- [53] Evan B Raeker, Kira M Pusch, Stéphane AJ Forsik, Ning Zhou, Austin D Dicus, Qing-Qiang Ren, Jonathan D Poplawsky, Michael M Kirka, and Tresa M Pollock. Minor elements and solidification cracking during laser powder-bed fusion of a high  $\gamma$  con-base superalloy. *Metallurgical and Materials Transactions A*, 54(5):1744–1757, 2023.
- [54] Nadia Kouraytem, Po-Ju Chiang, Runbo Jiang, Christopher Kantzos, Joseph Pauza, Ross Cunningham, Ziheng Wu, Guannan Tang, Niranjana Parab, Cang Zhao, et al. Solidification crack propagation and morphology dependence on processing parameters in aa6061 from ultra-high-speed x-ray visualization. *Additive Manufacturing*, 42:101959, 2021.
- [55] Sindo Kou. Solidification and liquation cracking issues in welding. *Jom*, 55:37–42, 2003.
- [56] Sen Yao, Jiajian Wang, Min Li, Zhen Chen, Bingheng Lu, Song Shen, and Yao Li. Lpbf-formed 2024al alloys: Process, microstructure, properties, and thermal cracking behavior. *Metals*, 13(2):268, 2023.
- [57] Jincheng Wang, Rui Zhu, Yujing Liu, and Laichang Zhang. Understanding melt pool characteristics in laser powder bed fusion: An overview of single-and multi-track melt pools for process optimization. *Advanced Powder Materials*, 2(4):100137, 2023.
- [58] Umberto Scipioni Bertoli, Alexander J. Wolfer, Manyalibo J. Matthews, Jean-Pierre R. Delplanque, and Julie M. Schoenung. On the limitations of volumetric energy density as a design parameter for selective laser melting. *Materials & Design*, 113:331–340, 2017.
- [59] Minhalina Ahmad Buhairi, Farhana Mohd Foudzi, Fathin Iliana Jamhari, Abu Bakar Sulong, Nabilah Afifah Mohd Radzuan, Norhamidi Muhamad, Intan Fadhlina Mohamed, Abdul Hadi Azman, Wan Sharuzi Wan Harun, and MSH Al-Furjan. Review on volumetric energy density: influence on morphology and mechanical properties of ti6al4v manufactured via laser powder bed fusion. *Progress in Additive Manufacturing*, 8(2):265–283, 2023.
- [60] A.B. Spierings, K. Dawson, P.J. Uggowitzer, and K. Wegener. Influence of slm scan-speed on microstructure, precipitation of al<sub>3</sub>sc particles and mechanical properties in sc- and zr-modified al-mg alloys. *Materials & Design*, 140:134–143, 2018.
- [61] Yining He, Ming Zhong, Jack Beuth, and Bryan Webler. A study of microstructure and cracking behavior of h13 tool steel produced by laser powder bed fusion using single-tracks, multi-track pads, and 3d cubes. *Journal of Materials Processing Technology*, 286:116802, 2020.
- [62] Taban Larimian, Manigandan Kannan, Dariusz Grzesiak, Bandar AlMangour, and Tushar Borkar. Effect of energy density and scanning strategy on densification, microstructure and mechanical properties of 316l stainless steel processed via selective laser melting. *Materials Science and Engineering: A*, 770:138455, 2020.
- [63] Armando Caballero, Wojciech Suder, Xin Chen, Goncalo Pardal, and Stewart Williams. Effect of shielding conditions on bead profile and melting behaviour in laser powder bed fusion additive manufacturing. *Additive Manufacturing*, 34:101342, 2020.
- [64] Haolin Jia, Hua Sun, Hongze Wang, Yi Wu, and Haowei Wang. Scanning strategy in selective laser melting (slm): a review. *The International Journal of Advanced Manufacturing Technology*, 113:2413–2435, 2021.

- [65] MM Dewidar, KW Dalgarno, and CS Wright. Processing conditions and mechanical properties of high-speed steel parts fabricated using direct selective laser sintering. *Proceedings of the Institution of Mechanical Engineers, Part B: Journal of Engineering Manufacture*, 217(12):1651–1663, 2003.
- [66] Weiran Zhang, Peter K Liaw, Yong Zhang, et al. Science and technology in high-entropy alloys. *Sci. China Mater*, 61(1):2–22, 2018.
- [67] Weidong Li, Di Xie, Dongyue Li, Yong Zhang, Yanfei Gao, and Peter K Liaw. Mechanical behavior of high-entropy alloys. *Progress in Materials Science*, 118:100777, 2021.
- [68] Bhagevatula Satyanarayana Murty, Jien-Wei Yeh, Srinivasa Ranganathan, and Pinaki Prasad Bhattacharjee. Chapter 1 - a brief history of alloys and the birth of high-entropy alloys and chapter 2 - high-entropy alloys: basic concepts. In *High-entropy alloys*. Elsevier, 2019.
- [69] Brain Cantor, ITH Chang, Peter Knight, and AJB Vincent. Microstructural development in equiatomic multicomponent alloys. *Materials Science and Engineering: A*, 375:213–218, 2004.
- [70] J-W Yeh, S-K Chen, S-J Lin, J-Y Gan, T-S Chin, T-T Shun, C-H Tsau, and S-Y Chang. Nanostructured high-entropy alloys with multiple principal elements: novel alloy design concepts and outcomes. *Advanced engineering materials*, 6(5):299–303, 2004.
- [71] Daniel B Miracle and Oleg N Senkov. A critical review of high entropy alloys and related concepts. *Acta Materialia*, 122:448–511, 2017.
- [72] Yong Zhang, Ting Ting Zuo, Zhi Tang, Michael C Gao, Karin A Dahmen, Peter K Liaw, and Zhao Ping Lu. Microstructures and properties of high-entropy alloys. *Progress in materials science*, 61:1–93, 2014.
- [73] Daniel B Miracle. High-entropy alloys: A current evaluation of founding ideas and core effects and exploring “nonlinear alloys”. *Jom*, 69(11):2130–2136, 2017.
- [74] Christopher Sutton and Sergey V Levchenko. First-principles atomistic thermodynamics and configurational entropy. *Frontiers in Chemistry*, 8:757, 2020.
- [75] Xin Wang, Wei Guo, and Yongzhu Fu. High-entropy alloys: emerging materials for advanced functional applications. *Journal of Materials Chemistry A*, 9(2):663–701, 2021.
- [76] Ming-Hung Tsai and Jien-Wei Yeh. High-entropy alloys: a critical review. *Materials Research Letters*, 2(3):107–123, 2014.
- [77] Tolulope Alo. Manufacturing of novel femnconizn high entropy alloy via powder metallurgy. *Ecole polytechnique de Louvain, Université catholique de Louvain*, 2021.
- [78] Zezhou Li, Shiteng Zhao, Robert O Ritchie, and Marc A Meyers. Mechanical properties of high-entropy alloys with emphasis on face-centered cubic alloys. *Progress in Materials Science*, 102:296–345, 2019.
- [79] MERTENS Anne. Phys0904-4 physique des matériaux. *Faculty of Applied Sciences (ULiège)*, 2022.



- [80] David G. Rethwisch William D. Callister Jr. Chapter 3 - structures of metals and ceramics. In *Fundamentals of Materials Science and Engineering: An Integrated Approach*. John Wiley & Sons, 2018.
- [81] S Shuang, ZY Ding, D Chung, SQ Shi, and Y Yang. Corrosion resistant nanostructured eutectic high entropy alloy. *Corrosion Science*, 164:108315, 2020.
- [82] Ming-Hung Tsai, Kun-Yo Tsai, Che-Wei Tsai, Chi Lee, Chien-Chang Juan, and Jien-Wei Yeh. Criterion for sigma phase formation in cr-and v-containing high-entropy alloys. *Materials Research Letters*, 1(4):207–212, 2013.
- [83] E. Kablman. Ab initio-based mean field theory of site occupation in binary sigma phases. *Institute of Materials Chemistry, Vienna University of Technology*, 2013.
- [84] Rui Feng, Michael C Gao, Chanhoo Lee, Michael Mathes, Tingting Zuo, Shuying Chen, Jeffrey A Hawk, Yong Zhang, and Peter K Liaw. Design of light-weight high-entropy alloys. *Entropy*, 18(9):333, 2016.
- [85] Xuejiao Chang, Mengqi Zeng, Keli Liu, and Lei Fu. Phase engineering of high-entropy alloys. *Advanced Materials*, 32(14):1907226, 2020.
- [86] GUO Sheng and Chain Tsuan Liu. Phase stability in high entropy alloys: Formation of solid-solution phase or amorphous phase. *Progress in Natural Science: Materials International*, 21(6):433–446, 2011.
- [87] Ruirun Chen, Gang Qin, Huiting Zheng, Liang Wang, Yanqing Su, YuLung Chiu, Hongsheng Ding, Jingjie Guo, and Hengzhi Fu. Composition design of high entropy alloys using the valence electron concentration to balance strength and ductility. *Acta Materialia*, 144:129–137, 2018.
- [88] Wei-Chen Hsu, Wei-Pin Kao, Jien-Wei Yeh, and Che-Wei Tsai. Effect of mo on the mechanical and corrosion behaviors in non-equal molar alcrfemnni bcc high-entropy alloys. *Materials*, 15(3):751, 2022.
- [89] C Li, JC Li, M Zhao, and Q Jiang. Effect of aluminum contents on microstructure and properties of alxcocrfeni alloys. *Journal of Alloys and Compounds*, 504:S515–S518, 2010.
- [90] Kan Ma, Thomas Blackburn, Johan P Magnussen, Michael Kerbstadt, Pedro A Ferreirós, Tatu Pinomaa, Christina Hofer, David G Hopkinson, Sarah J Day, Paul AJ Bagot, et al. Chromium-based bcc-superalloys strengthened by iron supplements. *Acta Materialia*, 257:119183, 2023.
- [91] SE Mousavi, AQ He, M Palimi, DL Chen, and DY Li. Influences of alloying elements on microstructure and tribological properties of a medium-weight high-entropy alloy. *Wear*, 524:204856, 2023.
- [92] Zhu Wang, Jie Jin, Guo-Hui Zhang, Xue-Hua Fan, and Lei Zhang. Effect of temperature on the passive film structure and corrosion performance of cocrfemnni high-entropy alloy. *Corrosion Science*, 208:110661, 2022.
- [93] Haver & boecker website. Available online. <https://www.haverboecker.com>, Accessed: 25 04 2024.

- [94] Netzsch website. Available online. <https://www.netzsch-thermal-analysis.com/en/>, Accessed: 25 04 2024.
- [95] Aconity website. Available online. <https://aconity3d.com/products/acnity-midi/>, Accessed: 25 04 2024.
- [96] Micromeritics website. Available online. <https://www.micromeritics.com/accupyc-ii/>, Accessed: 25 04 2024.
- [97] Bruker alicon. Available online. [www.alicon.com/en/products/infinitefocus/](http://www.alicon.com/en/products/infinitefocus/), Accessed: 25 04 2024.
- [98] Struers, knowledge and service. metallographic products. Available online. <https://www.struers.com/>, Accessed: 25 04 2024.
- [99] Olympus global homepage. Available online. <https://www.olympus-global.com/>, Accessed: 25 04 2024.
- [100] Tescan website. Available online. <https://www.tescan.com/tescan-clara-new-field-free-uhr-sem/>, Accessed: 25 04 2024.
- [101] Emco-test hardness testing machines acc. Available online. <https://www.emcotest.com/en/>, Accessed: 25 04 2024.
- [102] Amrit Jena, Rajesh Kumar Prusty, Bankim Chandra Ray, et al. Thermal behaviour and vickers indentation response of random discontinuous carbon/epoxy composites with nano-alumina fillers. *Materials Today: Proceedings*, 62:5911–5916, 2022.
- [103] Elias Anastasios Ananiadis, Konstantinos Lentzaris, Emmanuel Georgatis, Christina Mathiou, Anthoula Poulia, and Alexander E. Karantzalis. Al<sub>0.5</sub>CoCrFeNi equiatomic high entropy alloy: A further insight in its microstructural evolution, mechanical and surface degradation response. *Metals and Materials International*, 26:793–811, 2019.
- [104] YX Zhuang, XL Zhang, and XY Gu. Effect of molybdenum on phases, microstructure and mechanical properties of Al<sub>0.5</sub>CoCrFeNi high entropy alloys. *Journal of Alloys and Compounds*, 743:514–522, 2018.
- [105] Florin Ștefănescu, Gigel Neagu, Alexandrina Mihai, and Iuliana Stan. Controlled temperature distribution and heat transfer process in the unidirectional solidification of aluminium alloys. *Solid State Phenomena*, 188:314–317, 2012.
- [106] Chunxia Han, Yun Zhang, Jingshun Liu, Ze Li, Yanan Wu, Yaqiang Cui, Feng Wang, and Zetian Liu. Effect of Mo content on microstructure and mechanical properties of CoCrFeNi series high-entropy alloys. *Journal of Materials Research and Technology*, 2024.
- [107] Chih-Chun Hsieh and Weite Wu. Overview of intermetallic sigma ( $\sigma$ ) phase precipitation in stainless steels. *International Scholarly Research Notices*, 2012, 2012.
- [108] GA Salishchev, MA Tikhonovsky, DG Shaysultanov, ND Stepanov, AV Kuznetsov, IV Kolodiy, AS Tortika, and ON Senkov. Effect of Mn and V on structure and mechanical properties of high-entropy alloys based on CoCrFeNi system. *Journal of Alloys and Compounds*, 591:11–21, 2014.

- [109] Na Pang, Zhiming Shi, Cunquan Wang, Ninyu Li, and Yaming Lin. Influence of cr, mn, co and ni addition on crystallization behavior of al<sub>13</sub>fe<sub>4</sub> phase in al-5fe alloys based on thermodynamic calculations. *Materials*, 14(4):768, 2021.
- [110] Abhishek Mehta and Yongho Sohn. High entropy and sluggish diffusion “core” effects in senary fcc al-co-cr-fe-ni-mn alloys. *ACS Combinatorial Science*, 22(12):757–767, 2020.
- [111] Safia Alleg, Ahlem Bekhouche, Hacene Hachache, and Joan Jose Sunol. Effect of aluminum addition on the microstructure, magnetic, and mechanical properties of fccrconimn high-entropy alloy. *Crystals*, 13(10):1483, 2023.
- [112] A Munitz, L Meshi, and MJ Kaufman. Heat treatments’ effects on the microstructure and mechanical properties of an equiatomic al-cr-fe-mn-ni high entropy alloy. *Materials Science and Engineering: A*, 689:384–394, 2017.
- [113] Sriswaroop Dasari, Abhishek Sharma, Vishal Soni, Zachary Kloenne, Hamish Fraser, and Rajarshi Banerjee. Crystallographic and compositional evolution of ordered b2 and disordered bcc phases during isothermal annealing of refractory high-entropy alloys. *Microscopy and Microanalysis*, 29(1):303–313, 2023.
- [114] Hengwei Luan, Liufei Huang, Jingyi Kang, Bosang Luo, Xinglong Yang, Jinfeng Li, Zhi-dong Han, Jiajia Si, Yang Shao, Jian Lu, et al. Spinodal decomposition and the pseudo-binary decomposition in high-entropy alloys. *Acta Materialia*, 248:118775, 2023.
- [115] Upendra Kumar Mohanty and Hrushikesh Sarangi. Solidification of metals and alloys. *Casting Processes and Modelling of Metallic Materials*, pages 19–40, 2020.
- [116] Rada Novakovic, Donatella Giuranno, Joonho Lee, Markus Mohr, Simona Delsante, Gabriella Borzone, Fabio Miani, and Hans J Fecht. Thermophysical properties of metallic melts and their effects on solidification related processes. 2022.
- [117] Wei Zhang, Ali Chabok, Bart J Kooi, and Yutao Pei. Additive manufactured high entropy alloys: A review of the microstructure and properties. *Materials & Design*, 220:110875, 2022.
- [118] Rodrigo Magnabosco. Kinetics of sigma phase formation in a duplex stainless steel. *Materials Research*, 12:321–327, 2009.
- [119] Syuki Yamanaka, Ken-ichi Ikeda, and Seiji Miura. The effect of titanium and silicon addition on phase equilibrium and mechanical properties of co-cr-fem-ni-based high entropy alloy. *Journal of Materials Research*, 36(10):2056–2070, 2021.
- [120] Seungkyun Yim, Huakang Bian, Kenta Aoyagi, Kenta Yamanaka, and Akihiko Chiba. Effect of powder morphology on flowability and spreading behavior in powder bed fusion additive manufacturing process: a particle-scale modeling study. *Additive Manufacturing*, 72:103612, 2023.
- [121] Cekdar Vakifahmetoglu, Beyza Hasdemir, and Lisa Biasetto. Spreadability of metal powders for laser-powder bed fusion via simple image processing steps. *Materials*, 15(1):205, 2021.

- [122] Pelle Mellin, Masoud Rashidi, Marie Fischer, Lars Nyborg, Lorenzo Marchetti, Christopher Hulme-Smith, Markus Uhlirsch, and Annika Strondl. Moisture in metal powder and its implication for processability in l-pbf and elsewhere. *Berg-und Huttenmännische Monatshefte (BHM)*, 166(1):33–39, 2020.
- [123] Xiaoye Cai, Tong Liu, Xuan Yan, Zonghui Cheng, Lu Pan, Zongjun Tian, Liangshun Luo, and Yanqing Su. Effect of process parameters on microstructures and properties of al-42si alloy fabricated by selective laser melting. *Heliyon*, 8(6), 2022.
- [124] Zhiheng Hu, Haihong Zhu, Changchun Zhang, Hu Zhang, Ting Qi, and Xiaoyan Zeng. Contact angle evolution during selective laser melting. *Materials & Design*, 139:304–313, 2018.
- [125] Zhiheng Hu, Balasubramanian Nagarajan, Xu Song, Rui Huang, Wei Zhai, Jun Wei, et al. Formation of ss316l single tracks in micro selective laser melting: surface, geometry, and defects. *Advances in Materials Science and Engineering*, 2019, 2019.
- [126] Bo Song, Xiao Zhao, Shuai Li, Changjun Han, Qingsong Wei, Shifeng Wen, Jie Liu, and Yusheng Shi. Differences in microstructure and properties between selective laser melting and traditional manufacturing for fabrication of metal parts: A review. *Frontiers of Mechanical Engineering*, 10:111–125, 2015.
- [127] Huikai Li, Erin G Brodie, and Christopher Hutchinson. Predicting the chemical homogeneity in laser powder bed fusion (lpbf) of mixed powders after remelting. *Additive Manufacturing*, 65:103447, 2023.
- [128] Robert E Reed-Hill, Reza Abbaschian, and Reza Abbaschian. In *Physical metallurgy principles*, volume 17. Van Nostrand New York, 1973.

# Annex

## Annex A: Datasheet of 316L steel powder



**CARPENTER  
ADDITIVE®**

**PowderRange**

### Test Certificate

CT POWDERRANGE 316LF Rev4

Batch PR100466

Gas Atomised 316L Stainless Steel LPBF (Flexible)

For more information on Safety Data Sheets please contact:

[MSDS@CarpenterAdditive.com](mailto:MSDS@CarpenterAdditive.com)

#### CHEMICAL ANALYSIS

		Units	Min	Max	Result	Approved
C	Carbon	weight %	0	0.030	0.021	Pass
Cr	Chromium	weight %	16.0	18.0	17.6	Pass
Fe	Iron	weight %	Balance	-	Balance	Pass
Mn	Manganese	weight %	0	2.00	0.91	Pass
Mo	Molybdenum	weight %	2.00	3.00	2.34	Pass
Ni	Nickel	weight %	10.0	14.0	12.6	Pass
N	Nitrogen	weight %	0	0.10	0.09	Pass
O	Oxygen	weight %	0	0.10	0.03	Pass
P	Phosphorus	weight %	0	0.045	0.008	Pass
Si	Silicon	weight %	0	1.00	0.67	Pass
S	Sulphur	weight %	0	0.030	0.008	Pass

#### SIEVE ANALYSIS - ASTM B214

	Units	Min	Max	Result	Approved
+63 µm	weight %	0	0	0	Pass
+53 µm	weight %	0	1	0	Pass
+45 µm	weight %	Info Only	-	2.09	Pass

#### LASER SIZE DIFFRACTION - ASTM B822

	Units	Min	Max	Result	Approved
Dv (10)	µm	Info Only	-	19.8	Pass
Dv (50)	µm	Info Only	-	30.9	Pass
Dv (90)	µm	Info Only	-	48.0	Pass
-5 µm	volume %	0	0	0	Pass
-16 µm	volume %	0	10	2	Pass

Carpenter Additive is a business unit of Carpenter Technology Corporation, LPW is a wholly owned subsidiary of Carpenter Technology Corporation.  
LPW Technology Limited is a company registered in England and Wales  
Company Registration: 06233481 VAT Registration Number: GB 920134667  
Registered Office: 54 Portland Place London W1B 1DY

Page 1 of 2

## Annex B: Parameters for single track

Sample	Laser power [W]	Scanning speed [mm/s]	Volumetric Energy Density [ $Jmm^{-3}$ ]
1	50	200	0.250
2	50	400	0.125
3	50	600	0.083
4	50	800	0.063
5	50	1000	0.050
6	50	1200	0.042
7	100	200	0.500
8	100	400	0.250
9	100	600	0.167
10	100	800	0.125
11	100	1000	0.100
12	100	1200	0.083
13	100	1400	0.071
14	100	1600	0.063
15	100	1800	0.056
16	100	2000	0.050
17	150	200	0.750
18	150	400	0.375
19	150	600	0.250
20	150	800	0.188
21	150	1000	0.150
22	150	1200	0.125
23	150	1400	0.107
24	150	1600	0.094
25	150	1800	0.083
26	150	2000	0.075
27	175	200	0.875
28	175	400	0.438
29	175	600	0.292
30	175	800	0.219
31	175	1000	0.175
32	175	1200	0.146
33	175	1400	0.125
34	175	1600	0.109
35	175	1800	0.097
36	175	2000	0.088
37	185	600	0.308
38	185	800	0.231
39	185	1000	0.185
40	185	1200	0.154
41	185	1400	0.132
42	185	1600	0.116
43	185	1800	0.103
44	200	200	1.000
45	200	400	0.500
46	200	600	0.333
47	200	800	0.250
48	200	1000	0.200
49	200	1200	0.167
50	200	1400	0.143
51	200	1600	0.125
52	200	1800	0.111
53	200	2000	0.100